MODELING THE RADIATIVE DRYING PROCESS FOR INDUSTRIAL PRINTING APPLICATIONS

by

Brennan H. Fentzlaff

A thesis submitted in partial fulfillment of

the requirements for the degree of:

Master of Science

(Mechanical Engineering)

at the

UNIVERSITY OF WISCONSIN-MADISON

2016

(Page intentionally left blank.)

Approved by:

_____ _____

Professor Gregory F. Nellis Date

_____ _____

Professor Sanford A. Klein Date

(Page intentionally left blank.)

Abstract

Offset printing is an industrial printing process that uses forced drying to protect the printed image from defects and increase production rates. One method of drying uses infrared (IR) lamps to help evaporate the moisture off the printed surface. The IR drying process was investigated in detail through the creation of several models and experimental tests. The initial drying model simulated a corrugated board substrate passing across an IR dryer, and kept track of the radiation, conduction, convection, and mass transfer of the board. The initial model found that radiation was the dominant force behind the drying process because of its ability to rapidly increase the substrate's temperature.

To improve the initial drying model, a dryer radiation model was constructed to gain a better understanding of the radiation exchange in an IR dryer. The dryer radiation model utilized the developed semi-transparent radiosity method (STRM) to perform the analysis. The model produced a 1-D heat flux distribution that calculated the radiation heat flux that the substrate would experience when passing over the dryer. An experimental test was designed to measure the actual 1-D heat flux generated by the dryer. The dryer radiation model was supplied with the same conditions that the experiment was operated, and their results were compared to show that the model's and experiment's 1-D heat flux distributions agreed within 7.6%. The model and experiments showed that the lamp type had the largest impact on the dryer's performance, but the glass type and power level also affected the radiation exchange.

With the knowledge that the dryer radiation model was realistic, the initial drying model was improved by implementing the model's 1-D heat flux distribution. The improved drying model showed that radiation remained the dominant force in drying, but the board's convection coefficient and radiant properties should be investigated in more detail in the future.

Acknowledgements

I want to thank my advisors, Greg Nellis and Sandy Klein, for their advice and guidance throughout this research. It was your teaching and undergraduate classes that inspired me to pursue my graduate work at UW-Madison. I would not have the understanding or tools necessary to tackle engineering problems without your education. I also want to extend my gratitude to the rest of the Solar Energy Lab for their help.

I am grateful to have had the chance to work with all the employees of XDS Holdings, Inc. during my research. I specifically want to thank Rodger Whipple for his guidance in introducing the drying process and its components to me, as well as spearheading the experimental measurements with me. Josh Isaacson and Lee Hartjes also significantly contributed to my growth as a practical engineer with their help in the physical setup the experimental equipment—thank you, gentlemen. I also appreciate all the equipment XDS provided to fulfill the experimental work of my research.

I firmly believe I had a great upbringing because of the people who surrounded me—family and friends, alike. No matter the occasion, you have always been there pushing me to be a better student, athlete, and person, while making life exciting and enjoyable. I specifically want to thank my parents for developing my work ethic and providing me with countless opportunities—from a great education, to golf lessons, and my countless other hobbies. Lastly, thank you to my long-time girlfriend, Kirstyn Wood, for selflessly supporting me–thanks for being by my side.

Table of Contents

List of Figures

List of Tables

Nomenclature

Main Variables

Symbol	Description
A	surface area
AR	absorbed and reflected radiation
b	width into page of chill surface
C	ceramic glass
c	specific heat of corrugated board concentration of water vapor in air
c_{sat}	concentration of water vapor in air when air is saturated
$CSEM$	Coupled sub-enclosure method
CV	control volume
$D_{a,w}$	diffusion coefficient of water in air
D_{bulb}	diameter of bulb
dx	differential distance in x-direction
E_b	blackbody emissive power
$E_{b,lamp}$	blackbody emissive power of the lamp at its specified color temperature
F	view factor
f_f	fraction of lamps' blackbody emissive power that is absorbed in the front liner
f_λ	fraction of blackbody's radiation that is emitted in wavelength band lambda
$FRMW$	fast-response medium wave
g	gravitational acceleration
G	irradiation
H	height
$\bar{h}$	convection coeffiecient
$\bar{h}_D$	mass transfer coefficient
H_{bulb}	distance between bulb center and the cassette reflector
H_{clear}	clearance height--distance between dryer glass and board surface
H_{htr}	distance from cassette reflector to glass surface
J	radiosity
k	thermal conductivity
L	length
L_h	heated length
L_{htr}	length of triple-cassette dryer area
L_{lit}	length of the filament in a lamp

M	number of rows in the experimental test grid
m''	mass of substance per unit area
$\dot{m}_{air}$	mass flow rate of supply air
$m''_{ink,wet}$	mass of ink per unit area
$m''_{w,ini}$	initial mass of water per unit area
MCM	Monte Carlo method
MW	medium wave lamp
N	number of nodes in discretized numerical analysis number of surfaces in radiation analysis number of columns in experimental test grid
N_{calc}	number of calculations required for STRM
N_{λ}	number of wavelength bands
N_{rays}	number of rays simulated in the MCM
p_{fl}	fluting pitch
Q	quartz glass
$\dot{q}$	heat transfer rate
$\dot{q}_{bulb,\lambda}$	radiation heat transfer rate leaving the bulb surface within the wavelength band specified
$\dot{q}_{supply}$	lamps' supplied electrical power
$\dot{q}''_{surf}$	radiant heat flux on the chill surface
Ra	Rayleigh number
RH_{amb}	relative humidity of ambient conditions
S	spacing between chill tube centers
S_{bulb}	spacing between bulb centers
SR	sampling rate of the DAQ
$STRM$	semi-transparent radiosity method
SW	short wave lamp
T	temperature transmitted radiation
t_{cond}	time required for conduction
$t_{cond,fluting}$	time required for conduction in the fluting
$t_{cond,liner}$	time required for conduction in the liner
T_{sides}	temperature of chill surface under side cassettes
t_{ss}	time to reach steady-state
t_{travel}	time for board travel
th	liner thickness thickness of chill surface

u	corrugated board velocity
W	width
W_{htr}	width of triple-cassette dryer area
x	direction of corrugated board travel
y	direction normal to corrugated board travel y-position of node in discretized array
z	vertical direction
α	thermal diffusivity absorptivity Type 1 error rate
β	volumetric expansion coefficient
Δ	difference in
Δi_{vap}	latent heat of vaporization of water
ΔT_{htr}	rise in air temperature from passing through the dryer
ε	emissivity
η	efficiency
λ	wavelength index of wavelength band
λ_c	cutoff wavelength
μ	average of normal distribution
ν	kinematic viscosity degrees of freedom
ρ	density reflectivity
σ	Stefan-Boltzmann constant
$\hat{\sigma}$	standard deviation of normal distribution
σ^2	variance of normal distribution
τ	transmissivity
φ_{solid}	fraction of ink that is not moisture

Subscripts

Symbol	**Description**
∞	far away from the surface
a	of air
amb	of ambient conditions
$board$	of the board
$bott$	from the bottom
c	of corrugated board

cass	of one cassette
cond	of conduction
conv	of convection
eff	effective
fl	of fluting
g	geometric
i	of node at index *i* of surface *i*
j	of surface *j*
k	of surface *k*
lambda	of wavelength band lambda
max	maximum
max	maximum
meas	of the measurement area
rad	of radiation
surr	of surroundings
top	from the top
tot	total
w	of water

Ch. 1 Introduction

1.1 Offset Printing Process

The offset printing process is used for mass production printing jobs, such as printing newspapers, magazines, and other high-volume items. Offset printing can either be applied to a web or sheet substrate. Web-fed offset printing involves supplying a constant stream of a material (such as a large roll of paper or polymer film) to be printed on. Sheet-fed offset printing provides the press with individual substrates on (such as cardboard for product containers or corrugated board for shipping boxes) to be printed on. Offset printing can print images in black and white or in color. Color images require separate stages of ink application—one stage for each layer of ink applied (typically a sequence of cyan, magenta, yellow, and key (CMYK) inks). Figure 1 illustrates a conceptual view of a sheet-fed offset printing process for a color image on corrugated board.

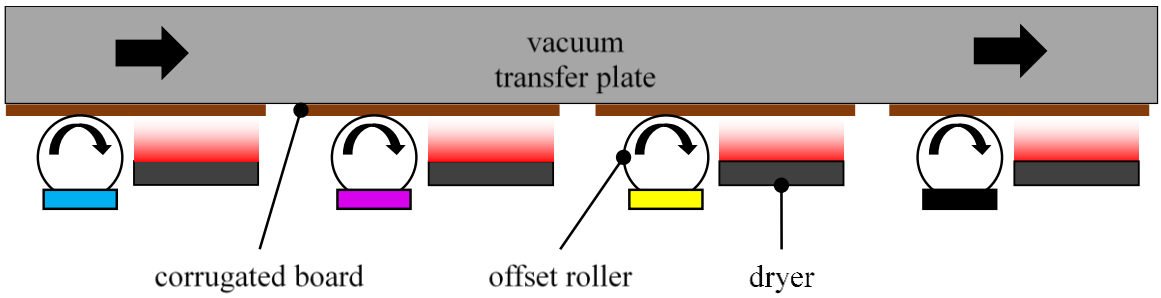

Figure 1: Offset printing process.

A vacuum transfer plate carries corrugated board into the press where an offset roller transfers a cyan image to the corrugated board. After application of the cyan ink, the corrugated board travels across a dryer to evaporate the moisture from the deposited ink. The press repeats this process with the other colored inks, ultimately producing a color image on the corrugated board.

Drying is an important process in offset printing because it protects the image from smearing and other image quality defects and allows the press to be operated at high production rates. Substrate feed rate, substrate material type, and ink type all determine the amount of drying required and what type of drying is necessary. Faster material speeds typically require more drying power. Printed surfaces that are hydrophobic (have little affinity towards water) need more drying energy because the water in the ink does not penetrate into the material, and is only present at the substrate surface. Certain ink types may contain more moisture and hence must be dried more thoroughly. As depicted in Figure 1, drying is especially important for color printing because the ink from one color application is dried before applying the next layer of ink.

There are various ways to dry solvent-based ink, including forced hot air and infrared (IR) radiative heating. Forced hot air dryers blow heated air onto the printed surface. The hot air warms the substrate and the air flow thins the boundary layer at the surface, both of which aid in evaporation of the moisture at the printed surface. IR heating dryers use infrared heat lamps to radiate thermal energy onto the substrate. This radiant energy increases the substrate temperature, which helps the evaporation process. To prevent the IR lamps from overheating, the IR dryers also force ambient air past the lamps. The forced air is then routed towards the substrate to thin the boundary layer at the printed surface to help the evaporation process. The IR dryers provide more drying power than forced hot air dryers because of the additional radiant energy.

The entire offset printing process, including drying, is controlled by the press operator. After inspecting samples of printed material, the operator will know if the substrate is sufficiently dry or if additional drying power is needed. The two main parameters the operator changes to control the amount of drying are the substrate feed rate and the electrical power

supplied to the IR lamps. Slower feed rates provide more drying to the ink because the substrate spends more time over the dryer. Higher supply power increases the amount of drying because more electrical energy is converted into emitted radiation from the IR lamps. A detailed view of the heat transfer behind the radiative drying process is described in Figure 2.

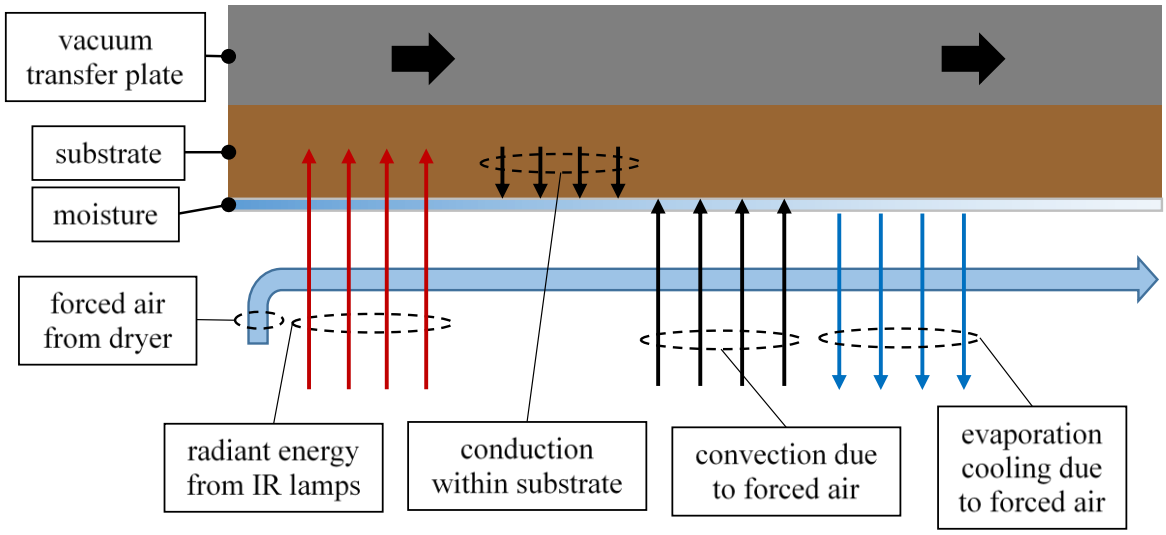

Figure 2: Heat transfer process of drying process with IR dryers.

The IR drying process involves four different modes of heat transfer: radiation, conduction, convection, and mass transfer. Radiation heat transfer is the transfer of thermal energy due to the exchange of electro-magnetic waves. In terms of the drying process, the IR lamps emit radiation, a fraction of which eventually is absorbed by the substrate. Conduction is the transfer of thermal energy within a solid. In the drying process, conduction occurs within the substrate. Convection is the transfer of thermal energy between a solid and a fluid. Because air is forced over the printed surface, convection contributes to the drying process at the printed surface. Mass transfer is the transfer of energy associated with evaporating liquid water at its surface. The physical action of drying ink is a mass transfer process because the ink's moisture evaporates into the forced air.

1.2 IR Dryer Design and Components

Figure 3 provides a picture of a typical IR dryer design. Figure 4 illustrates a side view of the dryer while operating on a printing press.

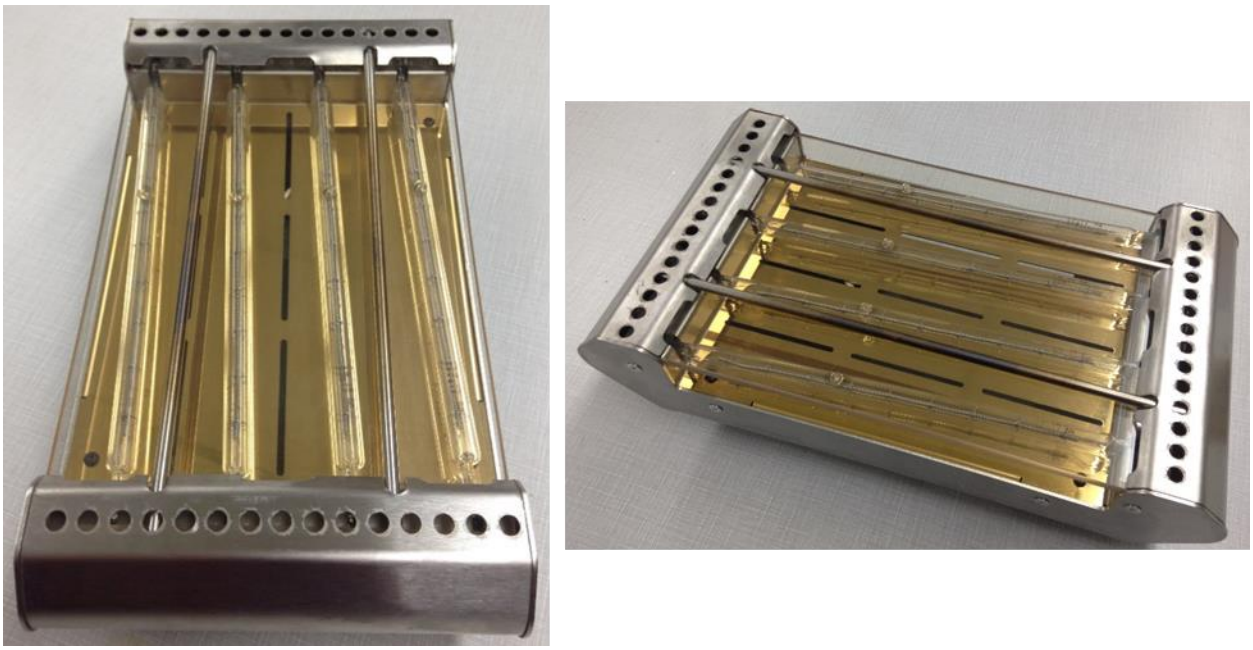

Figure 3: Single IR dryer cassette.

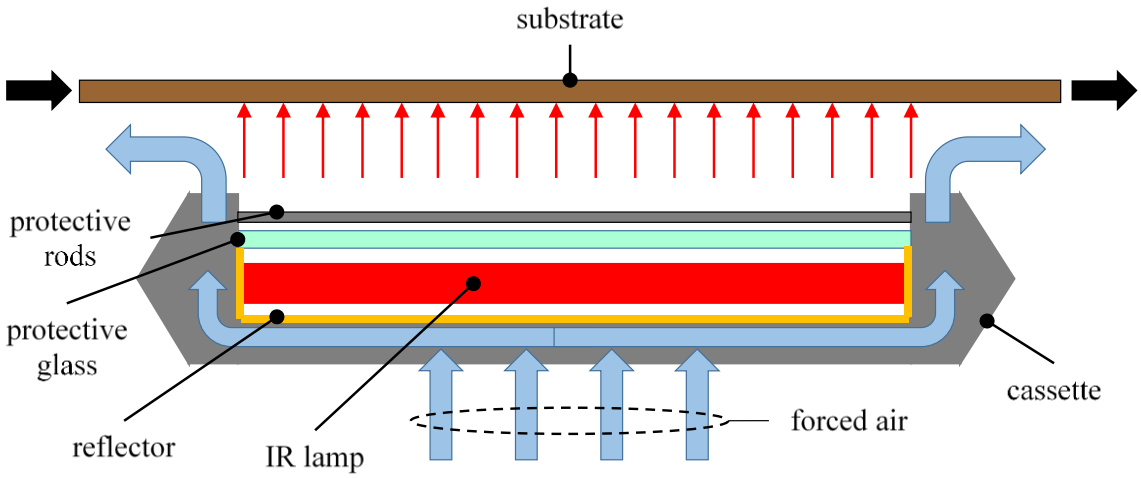

Figure 4: The mechanical design of an IR dryer.

As shown in Figure 3 and Figure 4, an IR dryer's outside housing is termed the cassette, which contains all the electrical connections and provides mounting for all other components. The cassette surfaces directly exposed to the radiation from the lamp have a reflective coating.

The forced air is pushed through the cassette to cool the IR lamps and eventually impinges upon the printed surface. Some dryer designs include protective components, such as the metal rods and the glass plate. The small protective rods are present to protect against the possibility that a substrate detaches from the vacuum transfer plate and jams against the dryer. A jammed substrate can provide enough force to break the glass plate and bulbs of the IR lamps—a costly accident.

The glass plate is meant to prevent dust from settling on the lamps and reflector surfaces, as dust on these hot surfaces can be a fire hazard. While including the glass plate in the design does prevent possible safety hazards and reduces cleaning maintenance, the glass plate can negatively impact the performance of the dryer. The glass plate absorbs a portion of the emitted radiation, preventing some of the absorbed energy from ever reaching the substrate. The amount of radiation absorbed in the glass largely depends on the type of glass being used, as different types of glass have different transmission properties.

The amount of radiation that is absorbed in the glass plate also depends on the spectrum of radiation emitted by the IR lamps. Each IR lamp consists of an electrically-resistive filament that is enclosed by a cylindrical, glass bulb. The basic concept of the IR lamp is that supplied electrical energy is dissipated in the filament, causing the filament temperature to increase to a steady-state value that is hot enough to emit a considerable amount of thermal radiation. Figure 5 below depicts a close-up comparison of three types of IR lamps: medium wave (MW), fast-response medium wave (FRMW), and short wave (SW).

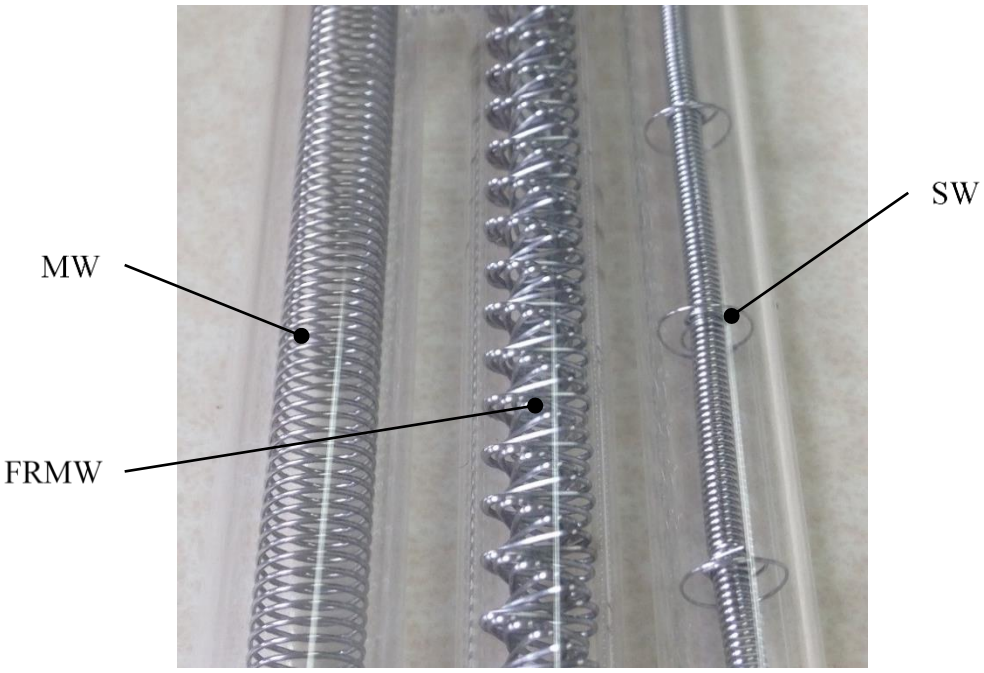

Figure 5: Comparison of three IR lamps and their filaments.

The amount of radiant energy leaving the lamps clearly depends on the amount of supplied electrical energy. The emitted radiation's spectrum depends on both the supplied electrical energy and the filament diameter. As more electrical energy is dissipated in the filament, the steady-state temperature increases and causes the spectrum of radiation to shift to shorter wavelengths. But for the same supplied electrical energy, a lamp with a tightly wound filament will reach a higher steady-state temperature than a lamp with a large filament diameter, which means filaments with a small diameter have radiation spectrums concentrated at shorter wavelengths, while filaments with large diameters have radiation spectrums spread out at longer wavelengths. Figure 5 demonstrates that the SW lamp has the smallest filament diameter, and thus will provide a radiation spectrum concentrated at shorter wavelengths. The MW lamp has the largest filament diameter and will produce a spectrum shifted towards longer wavelengths.

1.3 Proposed Analysis of Drying Process

This research describes a computer model that was developed to better understand the heat transfer mechanisms involved in the IR radiative drying process. The computer model estimates the amount of drying and all of the individual modes of heat transfer within the drying process, including radiation, conduction, convection, and mass transfer. The model calculates the total heat transferred to the substrate, along with the rate of moisture evaporation at the printed surface. The model also measures the efficiency of the dryer, which refers to the ratio of energy required to dry the ink compared to the total energy consumed by the dryer. The main purpose of the model was to compare the effectiveness of different IR dryer components (i.e., IR lamps, protective glass plates, etc.). Therefore, the model was based on fundamental physics to evaluate the performance of the dryer with these different components. The dryer design was assumed to be similar to the dryer in Figure 3 and Figure 4, so the model accounted for the details of the following parameters:

1. Lamp type
2. Glass type
3. Reflector coating
4. Clearance height
5. Supplied electrical power
6. Substrate material
7. Substrate feed rate

The model provides a deeper understanding of how the moisture in the ink is evaporated during the drying process, and along with the importance of the different modes of heat transfer. The

knowledge gained from the model will enable better dryer designs that decrease dryer energy use and dry the ink more quickly, which ultimately will lead to better profits for printing companies.

Ch. 2 Initial Model of Drying Process

An initial model was developed to provide insight into the drying process by using simplified geometry and general assumptions. This initial model was not meant to exactly simulate the drying process, but rather provide approximate information on how the different modes of heat transfer affected the drying process. The results of this initial model provided direction for the radiation model described in Ch. 4, ensuring that time and energy were not wasted on modeling phenomena that carried little relative importance in the drying process.

2.1 Initial Drying Model Geometry

The drying process simulated in the initial model is illustrated below in Figure 6.

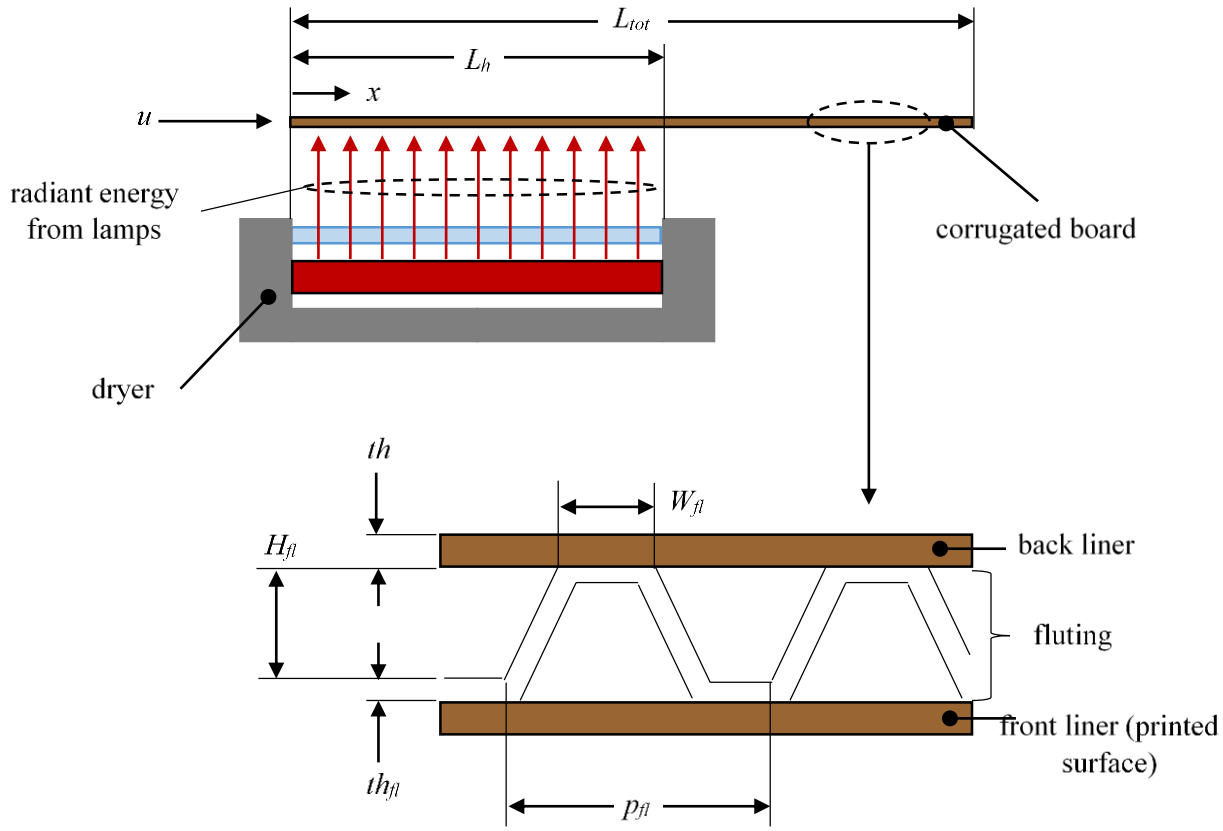

Figure 6: Simplified geometry for process time comparisons.

Figure 6 depicts the substrate as corrugated board (with printed side down) traveling over an IR dryer at speed, u. The printed surface is exposed to radiant energy from the IR dryer to heat the moisture in the ink and help it evaporate off the surface. Additionally, the board motion and the dryer's forced air reduces the boundary layer for convection and mass transfer. Table 1 below provides names, descriptions, and nominal values for the variables in Figure 6.

Table 1: Process time analysis parameters.

Parameter	Variable Symbol	Nominal Value/Range
Corrugated board velocity	u	20 – 300 ft/min
Heated length	L_h	155 mm
Total travel length	L_{tot}	610 mm
Thermal conductivity of corrugated board	k_c	0.05 W/m-K
Density of corrugated board	ρ_c	0.61 g/cm^3
Specific heat capacity of corrugated board	c_c	1400 J/kg-K
Thermal diffusivity of corrugated board	α_c	5.86e-8 m^2/s
Liner thickness	th	0.3 mm
Flute thickness	th_{fl}	0.2 mm
Flute pitch	p_{fl}	154 1/m
Flute-to-liner contact width	W_{fl}	6.49 mm
Flute height	H_{fl}	2.6 mm

2.2 Heat Transfer Process Time Comparisons

The first step in determining which heat transfer processes were important for drying was calculating the characteristic times required to achieve these different processes. The total time being analyzed in the model was determined by the speed of the corrugated board, u, and the total travel length, L_{tot}, as shown in Eq. (1).

$$t_{travel} = \frac{L_{tot}}{u} \tag{1}$$

Based upon the range of corrugated board velocities, t_{travel} ranged between 6.0 and 0.40 seconds. This travel time provided a base time to compare any other process times. If a process required significantly longer time than this travel time, that process was deemed unimportant to the drying process.

In general, the time required for conduction is given by Eq. (2).

$$t_{cond} = \frac{L^2}{4\alpha} \tag{2}$$

where L is the distance to conduct energy across and α is the thermal diffusivity of the material experiencing conduction. Figure 6 depicts that the corrugated board is composed of three sections: front liner, fluting, and back liner. The time required for energy to conduct through the front and back liners is given by Eq. (3).

$$t_{cond,liner} = \frac{th^2}{4\alpha_c} \tag{3}$$

Evaluation of Eq. (3) showed the time to conduct through the liners was $t_{cond,liner}$ = 0.68 seconds. This time was of the same magnitude as the total travel time found from Eq. (1), and thus conduction in the liner is important for the drying process.

The time required to conduct through the fluting was less obvious to calculate. The distance to conduct energy was along the diagonal of the fluting. This was computed using the fluting pitch, p_{fl}, and fluting height, H_{fl}. The time required for conduction through the fluting is shown in Eq. (4).

$$t_{cond,fluting} = \frac{\left[\left(\frac{p_{fl}}{2} - W_{fl}\right)^2 + H_{fl}{}^2\right]}{4\alpha_c} \tag{4}$$

Equation (4) lead to a conduction time of $t_{cond,fluting}$ = 35.5 seconds. This time was much higher than the total travel time previously calculated. Because the energy required 35.5 seconds to conduct through the fluting, but the travel time was at most 6.0 seconds, the energy would never able to fully conduct through the fluting.

The fluting section is also composed of air pockets, which might transfer the energy via natural convection. Natural convection is the transfer of energy from a solid to a fluid whose motion is induced by the heat transfer. Natural convection is often measured by the dimensionless Raleigh number:

$$Ra = \frac{g\beta_a H_{fl}^3 \Delta T}{\alpha_a \nu_a} \tag{5}$$

where g is the gravitational constant, H_{fl} is the vertical height of the fluting, and ΔT is the temperature difference between the front and back of the liner. β_a, α_a, ν_a are the volumetric expansion coefficient, thermal diffusivity, and kinematic viscosity of air, respectively. Assuming a temperature difference of 50 K (a conservative estimate based upon previous experimental measurements) leads to Ra = 37. In order for natural convection to be an appropriate model of heat transfer, Ra must be at least 2300. This means the air in the fluting pockets is essentially stagnant, and there will be little heat transfer through the air.

The process time comparisons suggested that heat transfer via conduction in the liners is important for the drying process, while the dynamics of the heat transfer in the fluting are unimportant to model. The fluting separates the front and back liners, and since the fluting has poor heat transfer performance, the front and back liners were considered thermally isolated. Additionally, the ink was assumed to be present only on the surface of the front liner, thus the ink only has thermal communication with the front liner—the fluting and the back liner were deemed to not affect the moisture on the printed surface. Based upon the process time

comparisons, only the front liner section of the corrugated board needed to be modeled, with an adiabatic boundary where the front liner contacted the fluting.

2.3 Initial Drying Model Setup

The comparison of heat transfer process times suggested that the corrugated board could essentially be modeled solely as the front liner without affecting the ink drying analysis. The initial drying model made several assumptions about the drying process to simplify the analysis. These assumptions are listed below:

1. The corrugated board was modeled as only the front liner because the thermal gradients in the fluting and back liners do not affect the drying process.
2. The front liner material was homogenous with constant thermal properties.
3. All of the applied ink was only present on the printed surface—the moisture was assumed to not penetrate into the front liner.
4. The convection coefficient of the printed surface was assumed to be constant throughout the entire process.
5. The radiant energy from the dryer was applied only while the corrugated board was directly above the dryer.
6. The radiant energy incident on the board was constant and assumed to be equal to the blackbody emissive power defined by the lamps' color temperature.
7. Only a fraction of the total incident radiation, f_f, was absorbed in the front liner.
8. Because the liner is thin (~0.3 mm) and f_f is typically small, the absorbed radiation was assumed to be absorbed equally throughout the thickness of the liner.

To model the conduction in the front liner, a column of N temperature nodes were discretized across the front liner thickness, as shown in Figure 7.

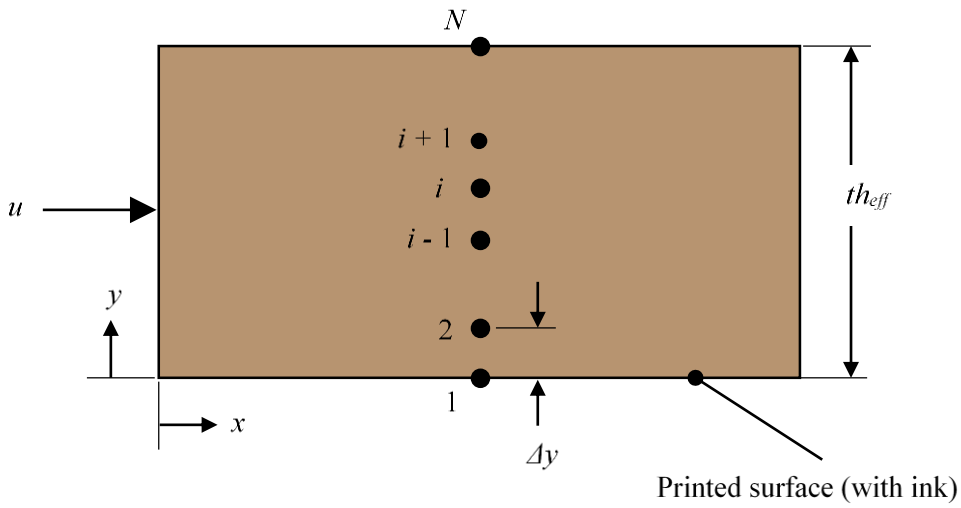

Figure 7: Discretization of the front liner.

The spatial distribution of the nodes consisted of *N* vertical locations distributed across the front liner thickness. The detailed view in Figure 6 showed that a portion of the front liner was in direct contact with the fluting. To account for the added thickness of the fluting, an effective thickness was defined, as in Eq. (6).

$$th_{eff} = th + \frac{th_{fl}}{2} \tag{6}$$

Because the nodes were equally spaced across the effective thickness, the nodes' y-positions and spacing between them were determined:

$$y_i = \frac{th_{eff}\,(i-1)}{(N-1)} \tag{7}$$

$$\Delta y = \frac{th_{eff}}{(N-1)} \tag{8}$$

The energy transfer in the front liner was modeled by a stationary, control-volume (CV) analysis on all nodes. The CV was differentially small in *x* (*dx* approaching zero) and stationary (i.e., the corrugated board flowed through the CV). Figure 8 illustrates an example of a CV around node *i*.

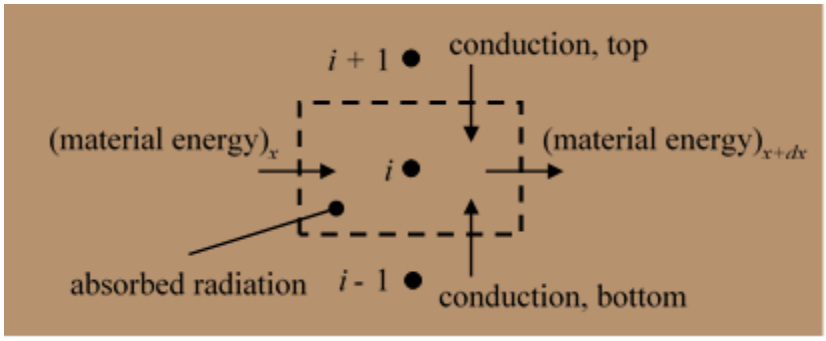

Figure 8: CV analysis of internal node i.

The heat transfer due to conduction from the upper and lower nodes are shown in Eqs. (9) and (10), respectively.

$$conduction, top = \frac{k_c dx W}{\Delta y}(T_{i+1} - T_i) \tag{9}$$

$$conduction, bottom = \frac{k_c dx W}{\Delta y}(T_{i-1} - T_i) \tag{10}$$

where W is the width into the page of the material and T_i is the temperature of node i. The energy of the corrugated board material as it enters the CV was given by:

$$(material\ energy)_x = \rho_c c_c u W \Delta y T_i \tag{11}$$

Because the energy of the material changed because of absorbed radiation or conduction, the energy of the corrugated board as it exited the CV was given by:

$$(material\ energy)_{x+dx} = \rho_c c_c u W \Delta y T_i + \frac{d}{dx}\left(\rho_c c_c u W \Delta y T_i\right) dx \tag{12}$$

Finally, the radiant energy from the lamps that was absorbed in the CV is shown in Eq. (13).

$$absorbed\ radiation = f_f E_{b,lamp} dx W \frac{\Delta y}{th_{eff}} \tag{13}$$

where $E_{b,lamp}$ is the blackbody emissive power of the lamp, evaluated at the lamp's manufacturer-specified color temperature, and f_f is the fraction of that radiation that gets absorbed in the front

liner. Because f_f is typically small, the uniform radiation absorption was an appropriate assumption. An energy balance on the CV is:

$$\begin{aligned} &conduction,top + conduction,bottom + absorbed\ radiaiton \\ &+ (material\ energy)_x = (material\ energy)_{x+dx} \end{aligned} \tag{14}$$

By substituting Eqs. (9) through (13) into Eq. (14), the energy balance simplified to:

$$\underbrace{\frac{k_c}{\Delta y}(T_{i+1} - T_i)}_{conduction,top} + \underbrace{\frac{k_c}{\Delta y}(T_{i-1} - T_i)}_{conduction,bottom} + \underbrace{f_f E_{b,lamp} \frac{\Delta y}{th_{eff}}}_{absorbed\ radiation} = \underbrace{\rho_c c_c u \Delta y \frac{dT_i}{dx}}_{stored\ energy} \tag{15}$$

Equation (15) was valid for all internal nodes, thus i = 2..(N-1). The same process was performed on node N—the only difference was that node N's CV was half the height of the internal nodes' CV. The energy balance for node N is shown in Eq. (16).

$$\underbrace{\frac{k_c}{\Delta y}(T_{N-1} - T_N)}_{conduction,bottom} + \underbrace{f_f E_{b,lamp} \frac{\Delta y}{2th_{eff}}}_{absorbed\ radiation} = \underbrace{\rho_c c_c u \frac{\Delta y}{2} \frac{dT_i}{dx}}_{stored\ energy} \tag{16}$$

The CV analysis for node 1 was slightly more complicated, as it included convection and mass transfer from the ink's moisture evaporating. Figure 9 illustrates the CV with all the energy terms shown.

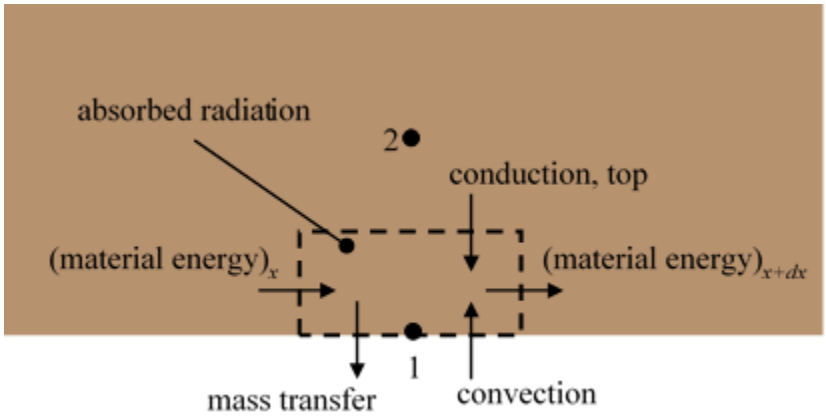

Figure 9: CV analysis of node 1 on the printed surface.

The convection term represented the heat transfer from the surrounding air to the corrugated board. Equation (17) shows how this convection term was modeled.

$$convection = \bar{h} dx W (T_\infty - T_1) \tag{17}$$

where $\bar{h}$ is the average convection coefficient and T_∞ is the temperature of the air in contact with the corrugated board. T_∞ was determined by Eq. (18).

$$T_\infty = T_{amb} + \Delta T_{htr} \tag{18}$$

where ΔT_{htr} is the rise in temperature of the air after being forced through the dryer. The mass transfer term represented the heat transfer due to the moisture evaporation process; the mass transfer term is shown in Eq. (19).

$$mass\ transfer = \dot{m}''_w dx W \Delta i_{vap} \tag{19}$$

where $\dot{m}''_w$ is the mass flow rate of moisture evaporation per unit area, and Δi_{vap} is the latent heat of vaporization of water. The energy balance for the CV of node 1 simplified to:

$$\underbrace{\frac{k_c}{\Delta y}(T_2 - T_1)}_{conduction,top} + \underbrace{\bar{h}(T_\infty - T_1)}_{convection} + \underbrace{f_f E_{b,lamp} \frac{\Delta y}{2th_{eff}}}_{absorbed\ radiation} = \underbrace{\dot{m}''_w \Delta i_{vap}}_{mass\ transfer} + \underbrace{\rho_c c_c u \frac{\Delta y}{2} \frac{dT_i}{dx}}_{stored\ energy} \tag{20}$$

The mass flow rate of moisture evaporation was modeled using the heat-mass transfer analogy. This meant that the mass flow rate of evaporation was given by:

$$\dot{m}''_w = \begin{cases} \bar{h}_D (c_{sat} - c_\infty) & if\ \ m''_w > 0 \\ 0 & if\ \ m''_w = 0 \end{cases} \tag{21}$$

The variable $\bar{h}_D$ is the mass transfer coefficient, and c_{sat} and c_∞ are the concentration of water vapor at the ink surface and in the surrounding air, respectively. These values were based upon the air temperature and the relative humidity, RH_{amb}. When the printed surface became completely dry, evaporation stopped, and thus mass transfer no longer affected the heat transfer

process. The mass transfer coefficient is similar to the convection coefficient under the heat-mass transfer analogy. The mass transfer coefficient is defined by Eq. (22).

$$\bar{h}_D = \bar{h}\frac{D_{a,w}}{k_a} \tag{22}$$

where $D_{a,w}$ is the diffusion coefficient of water in air, and k_a is the thermal conductivity of air—both evaluated at the film temperature (the average of the surface temperature and surrounding air temperature). To track the moisture, a mass balance on the ink's water content was performed, as shown in Eq. (23).

$$0 = \dot{m}''_w + u\frac{dm''_w}{dx} \tag{23}$$

The initial moisture that was present on the surface is given by:

$$m''_{w,ini} = m''_{ink,wet}(1-\phi_{solid}) \tag{24}$$

where $m''_{ink,wet}$ is the mass of ink per unit area and φ_{solid} is the fraction of ink that is not moisture. The previous equations were entered into Engineering Equation Solver (EES) and numerically integrated forward in time by integrating with respect to x. The initial drying model appears in the electronic supplement, as outlined in Appendix C:.

2.4 Initial Drying Model Results

Table 2 below lists the necessary inputs for the EES model.

Table 2: Necessary input parameters for initial model.

Description	Symbol	Nominal Value/Range
Corrugated board velocity	u	20 – 300 ft/min
Heated length	L_h	155 mm
Total travel length	L_{tot}	610 mm
Thermal conductivity of corrugated board	k_c	0.05 W/m-K
Density of corrugated board	ρ_c	0.61 g/cm^3

Specific heat capacity of corrugated board	c_c	1400 J/kg-K
Thermal diffusivity of corrugated board	α_c	5.86e-8 m^2/s
Liner thickness	th	0.3 mm
Flute thickness	th_{fl}	0.2 mm
Radiation from lamps	$E_{b,lamp}$	595.2 kW/m^2
Fraction of energy absorbed in front liner	f_f	0.143 (based upon previous experimental data)
Ambient temperature	T_{amb}	20 ℃
Ambient relative humidity	RH_{amb}	50%
Air temperature rise from heater	ΔT_{htr}	40 K
Wet mass of ink per area	$m''_{ink,wet}$	2.11 g/m^2
Fraction of ink that is not moisture	φ_{solid}	0.4
Convection coefficient	$\bar{h}$	varies

Figure 10 depicts the temperature of various position nodes as a function of x, with, u = 100 ft/min (~0.508 m/s) and $\bar{h}$ = 100 W/m^2-K. Figure 10 also illustrates the amount of moisture on the surface of the corrugated board, indicated by the dashed red line associated with the right side Y-axis.

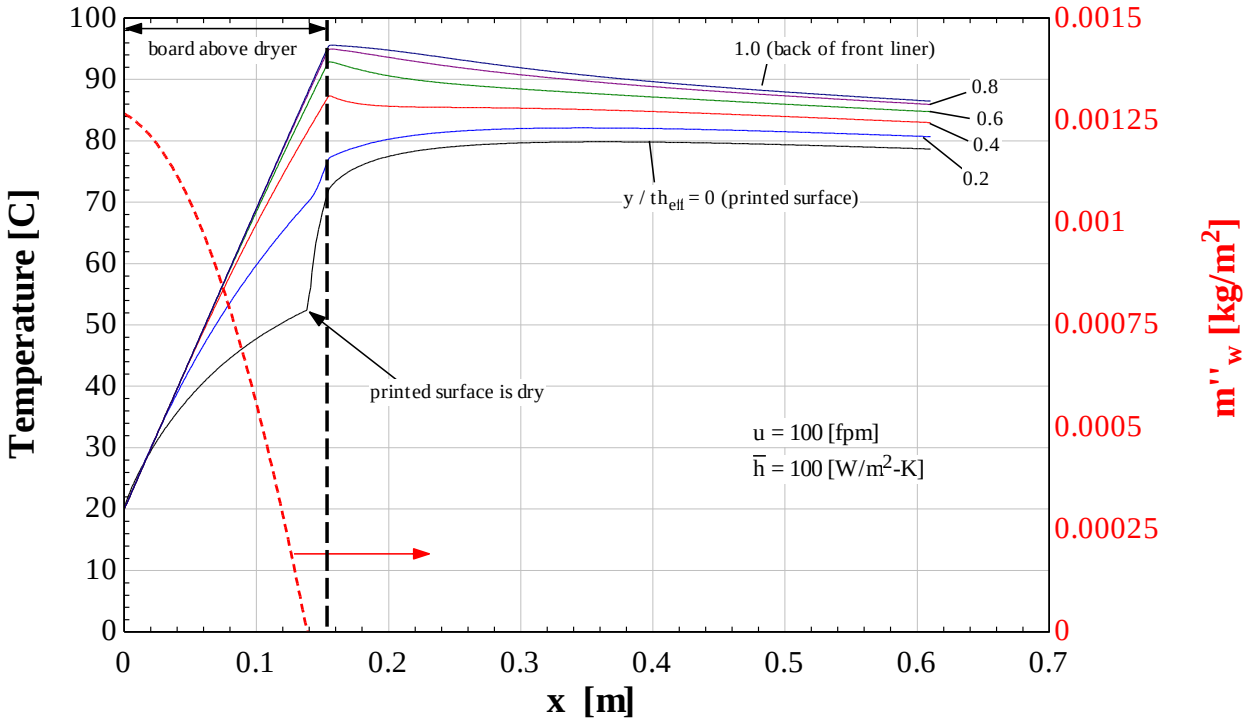

Figure 10: Temperature and moisture distribution of the corrugated board.

The plot agrees with intuition; almost all the node temperatures rose together due to the assumption that the absorbed radiation was equally-distributed across the liner thickness. This property indicated that the lamp radiation had a large impact on the heat transfer process. One interesting feature of the plot is the cooling effect of the moisture evaporation. As the corrugated board began to travel across the heater, the ink moisture content started at the specified level and dropped steeply until it dried at $x \approx 0.144$ m. The model only had moisture present on the board's printed surface and so the temperature of the node at the printed surface remained significantly colder than all other nodes while the moisture evaporated. As soon as the moisture dried, there was a large spike in the printed surface's temperature because the cooling effect of evaporation was lost.

To compare the modes of heat transfer, Figure 11 plots the contribution of each mode (radiation, mass transfer, convection, and conduction) to the heat transfer process within the CV at the printed surface.

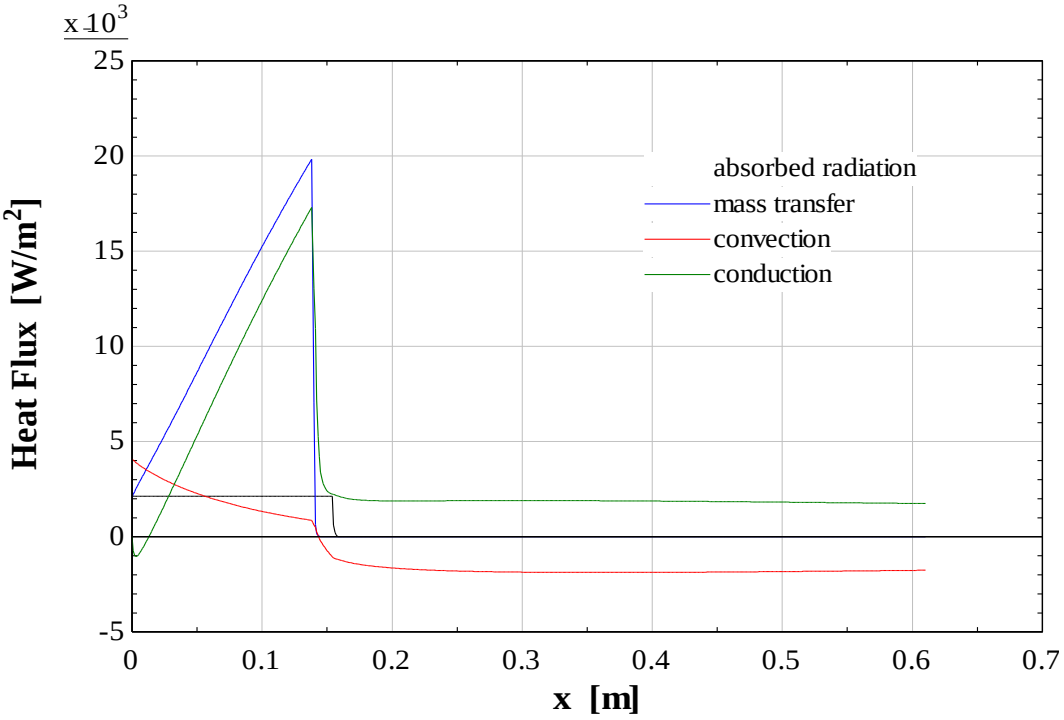

Figure 11: Comparison of heat transfer modes at the printed surface CV.

At first glance, Figure 11 suggests that the drying process was dominated by mass transfer and conduction, since they had relatively large heat flux values compared to absorbed radiation and convection. This conclusion is slightly misleading, though. The conduction term physically represents the energy transferred from the adjacent nodes in the front liner to the printed surface. Because the internal nodes of the front liner were only externally heated by the absorbed radiation, the energy received by the printed surface through conduction is actually energy that originated as absorbed radiation. To gain a more intuitive perspective on the modes of heat transfer, the *effective absorbed radiation* seen by the printed surface is actually the sum of the radiation absorbed by node 1 at the printed surface and the energy transferred to the surface via conduction. The plot of this comparison is shown in Figure 12.

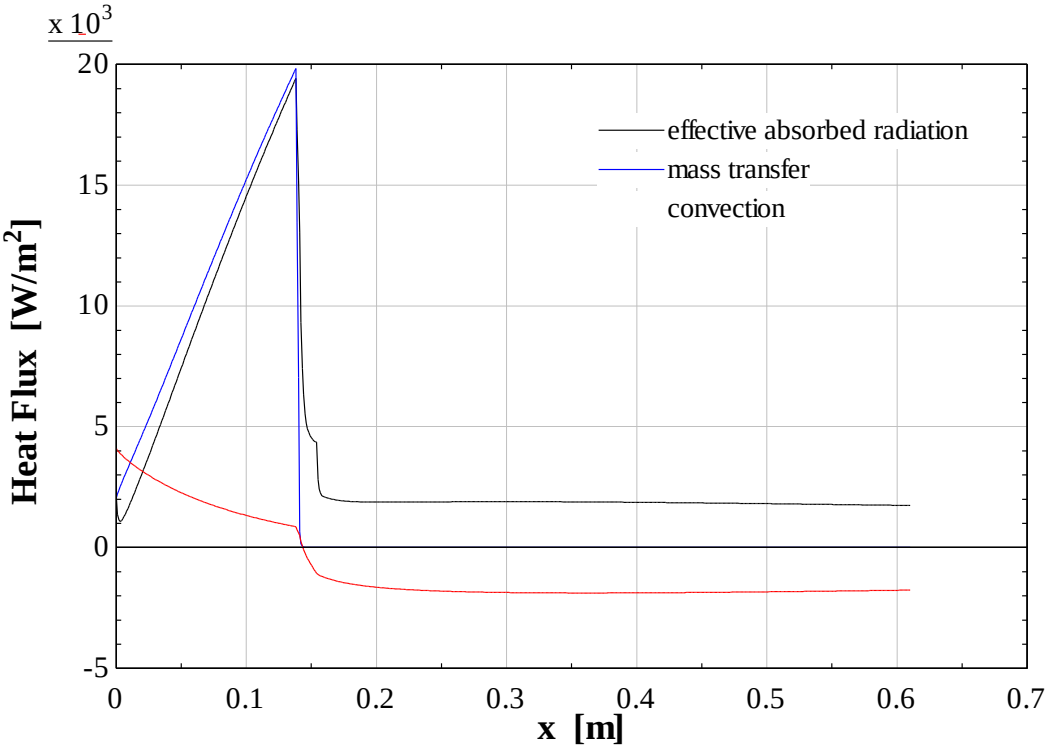

Figure 12: Comparison of effective heat transfer modes at the printed surface CV.

Figure 12 illustrates that the effective absorbed radiation almost matched the mass transfer heat flux, implying that nearly all of the drying process was forced by the radiation—not convection. These observations actually provide further insight to the comparison in Figure 11. While Figure 12 demonstrates that the drying process was mostly forced by radiation, Figure 11 shows that the mass transfer process was not significantly forced by radiation absorbed at the surface, but rather mostly dictated by the radiation absorbed by the nodes near the printed surface and then conducted into the surface. This indicates that the assumption regarding the spatially-uniform radiation absorption in the front liner likely has a significant impact on the drying process, and was investigated in section 7.3.

Figure 11 and Figure 12 suggest that all of the radiation absorbed in the front liner (not just radiation absorbed at the surface) was important to the drying process. To compare the total

amount of radiation, mass transfer, and convection in the drying process, Figure 13 plots the total modes of heat transfer.

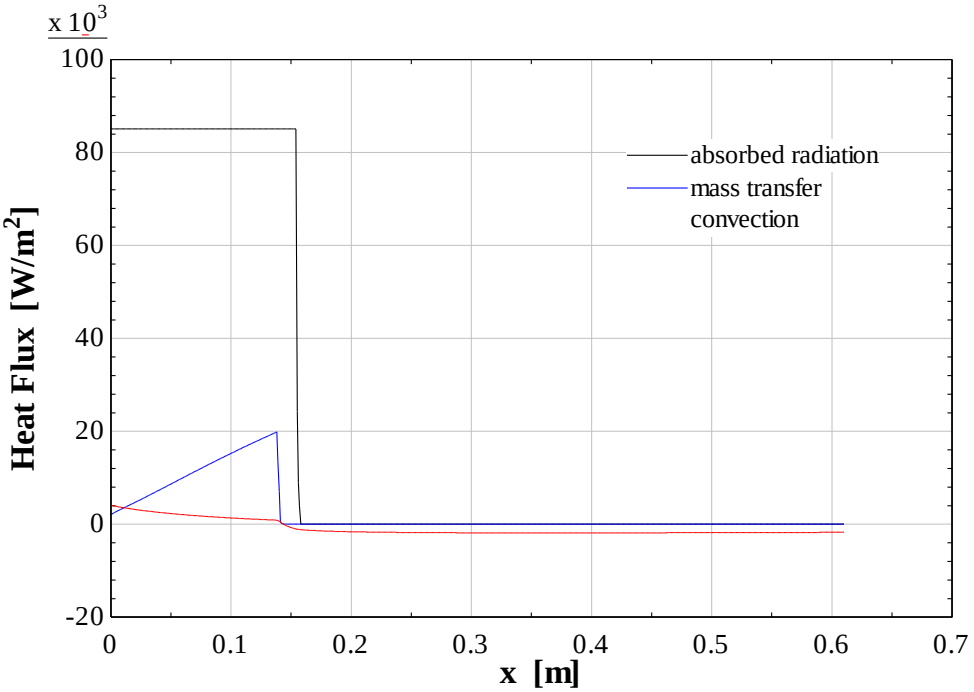

Figure 13: Comparison of the total heat transfer modes.

The total amount of radiation clearly dwarfed the heat transfer due to convection, and was the driving force for drying the ink's moisture. Assuming the input variables were representative of the actual process, Figure 10 through Figure 13 suggest that radiation had the greatest impact on the drying process. Assuming convection was negligible, Figure 13 also provides an illustration of an approximate drying efficiency. The area under the mass transfer curve was used to determine the total energy required to evaporate the moisture in the ink, as shown in Eq. (25).

$$energy\ required\ to\ evaporate\ moisture = \int \frac{mass\ transfer}{u} dx \tag{25}$$

The area under the absorbed radiation curve represents the total energy that was absorbed by the front liner and was calculated according to Eq. (26).

$$radiant\ energy\ absorbed\ in\ \ front\ liner = \int \frac{absorbed\ \ radiation}{u} dx \tag{26}$$

The ratio of these values describes how much of the absorbed radiation was actually utilized for drying the ink. This ratio was considered a type of dryer efficiency. The efficiency of the dryer for the above situation, where u = 100 ft/min and $\bar{h}$ = 100 W/m^2-K, is shown in Eq. (27).

$$\eta_{elec \rightarrow rad} = \frac{energy\ required\ to\ evaporate\ moisture}{radiant\ energy\ absorbed\ in\ \ front\ liner} = \frac{3043\ \frac{J}{m^2}}{26289\ \frac{J}{m^2}} \approx 11.5\% \tag{27}$$

The efficiency in Eq. (27) only describes the portion of the drying process within the corrugated board; the total efficiency of the drying process is even less because not all the dryer's supplied electrical energy is converted into absorbed radiation. To calculate the total drying efficiency, a relation is needed to conclude how much of the dryer's supplied electrical power was converted into absorbed radiation in the corrugated board. This initial model assumed that the radiant energy from the lamps was equal to the blackbody emissive power evaluated at the lamp's specified color temperature. In reality, the radiant energy incident on the corrugated board depends upon many factors, including supplied electrical power, lamp type, glass plate type, reflector coating, clearance height, and other factors. Furthermore, the initial model assumed that the absorbed radiation within the front liner was some fraction, f_f, of the lamps' blackbody emissive power. Physically, the portion of the incident radiation that was absorbed in the corrugated board depends on the board's radiant properties, the incident radiation's wavelength spectrum, and other factors. All of the above factors were not properly taken into account within this initial model.

There was also a large uncertainty for the convection coefficient, which affected both the convection and mass transfer terms of the model. Additionally, the range of board speeds could

significantly affect the total amount of radiation absorbed. These uncertainties further reinforce that the purpose of this initial model was simply to identify the important parameters that should be investigated in more detail.

2.5 Initial Drying Model Conclusions

The initial model was meant to distinguish the important modes of heat transfer in the drying process from the modes that had little effect on the drying process. The comparison of heat transfer process times determined that only the front liner affected the evaporation of the ink's moisture—meaning that the fluting and back liner were unimportant to the drying process and thus did not need to be considered. The initial model showed that the radiation from the lamps provided the largest contribution to the drying process, with mass transfer being the second most important mode of heat transfer.

While there were several avenues to consider for better estimating the drying process, the most important aspect from the initial model to investigate was the radiation exchange. Because radiation had the greatest impact on the drying process, the radiant energy from the lamps was considered in more detail in Ch. 4. A radiation model was created in Ch. 4 to simulate the exchange of thermal radiation of all surfaces involved in the drying process. The radiation model relates how much of the supplied electrical energy is converted into thermal radiation that gets absorbed by the corrugated board.

Ch. 3 Modeling Thermal Radiation by Semi-Transparent Radiosity Method

The initial drying model presented in Ch. 2 showed that radiation was the most important mode of heat transfer within the drying process. Because radiation had the largest impact on the drying process, a detailed radiation model was created (described in Ch. 4) to investigate the thermal radiation exchange between all the surfaces involved in the drying process. There were several techniques available for modeling surfaces experiencing thermal radiation exchange—two of the most well-known included the *net radiation method* (NRM, also known as the *radiosity method*) and the *Monte Carlo method* (MCM). The *semi-transparent radiosity method* (STRM) was developed during this research to accurately track thermal radiation exchange between surfaces that include semi-transparent surfaces. Before describing the geometry and setup of the radiation model in Ch. 4, a derivation of the STRM and comparison with the NRM and MCM is presented.

3.1 Current Techniques for Modeling Thermal Radiation Exchange

The NRM has been well documented ([1], [2]) as a convenient way to model thermal radiation exchange within an enclosure of surfaces. The NRM uses a linear set of equations, shown in Eqs. (28) and (29), to determine the amount radiation leaving a surface and the amount of radiation absorbed by the surface.

$$\dot{q}_{rad,i} = \frac{\varepsilon_i A_i \left(E_{b,i} - J_i \right)}{1-\varepsilon_i}, \quad for\ i = 1 \ldots N \tag{28}$$

$$\dot{q}_{rad,i} = A_i \sum_{j=1}^{N} F_{g,i,j} \left(J_i - J_j \right), \quad for\ i = 1 \ldots N \tag{29}$$

where $\dot{q}_{rad}$ is the surface heat transfer rate due to thermal radiation, E_b is the surface's blackbody emissive power, ε is the surface's emissivity, and A is the surface area. The variable J is termed the *radiosity* of a surface, and is defined as the total radiation leaving the surface (both emitted and reflected radiation). The variable $F_{g,i,j}$ is the geometric view factor from surface i to surface j, and represents the fraction of diffuse radiation leaving surface i that directly hits surface j. Equations (28) and (29) provide $2N$ equations, yet typically there are $3N$ unknown variables (E_b, J, and $\dot{q}_{rad}$). To fully constrain the system of equations, the user specifies N boundary conditions—typically a combination of surface temperatures and heat transfer rates.

Equations (28) and (29) mathematically compare the radiation emitted from a surface and the radiation absorbed at a surface, and the difference between those values is the surface's net heat transfer rate due to thermal radiation exchange. The NRM is accurate under the following surface assumptions:

1. Isothermal: the entire surface is at one temperature
2. Diffuse: the surface emits/reflects radiation equally in all directions
3. Opaque: radiation incident on a surface is either absorbed or reflected (not transmitted)

The NRM is a deterministic method, meaning the algorithm will result in the same solution every time for the same inputs. Additionally, the NRM can be extended to solve semi-gray problems by dividing the analysis into separate wavelength bands, and summing the spectral results to solve for the total heat transfer rates. The major disadvantage of the NRM is it's inflexibility to assumptions; if the surface network badly violates one of the assumptions, the NRM may provide an inaccurate solution of surface temperatures and heat transfer rates.

For the NRM to simulate semi-transparent surfaces (such as the protective glass plate in the dryer), the surface network must be partitioned into sub-enclosures and the NRM needs to be applied separately within each sub-enclosure. The sub-enclosures are coupled by an energy balance on the partitioning semi-transparent surface. This hybrid method (referred to here as the *coupled sub-enclosure method*—CSEM) is described in more detail in [3]. Unfortunately the CSEM does not account for the directionality of the radiation when it is transmitted through the semi-transparent surface and likewise does not provide a precise solution of heat transfer rates and temperatures.

The MCM models radiation exchange within enclosures by simulating random rays of radiation from an emitting surface, and then tracking the ray within the enclosure until the ray gets absorbed by another surface. Each ray is assigned an amount of energy depending on the emitting surface's temperature and radiant properties. The amount of energy absorbed by a surface is the sum of the energy associated with all rays that are absorbed at that surface. The amount of radiant energy emitted by a surface is the sum of energy associated with all rays leaving that surface. The difference between a surface's absorbed energy and its emitted energy is the surface's net heat transfer rate due to radiation. It is a very powerful technique that does not require any major assumptions. The MCM can model spectral-, specular-, or temperature-dependent radiant properties, spatially-varying temperatures, and semi-transparent surfaces. The foremost disadvantage of the MCM is its computational requirements. The MCM is a stochastic process (based upon randomness), which requires large quantities of simulated rays to obtain results that converge towards the correct solution. Furthermore, as the surface network and its radiant properties get more complex (i.e., more surfaces, spectral or specular properties, etc.) the

MCM requires even more computational effort. The large computational effort along with its poor computational scalability causes the MCM to be undesirable for some analyses.

3.2 Semi-Transparent Radiosity Method Description

The STRM is a modified version of the NRM that uses *effective view factors*, but is otherwise analogous to the NRM. Effective view factors are defined as the fraction of radiation that leaves a surface and is directly *absorbed on or reflected from* another surface, without reflection from other surfaces. Using effective view factors is a simple modification to the NRM equations that allows the method to track the directionality of radiation in enclosures that contain semi-transparent surfaces. The STRM offers clear advantages over the computationally intensive MCM which is the only other alternative to accurately model these situations.

The STRM is an extension of the NRM, and so the assumptions required by the STRM are very similar. Like the NRM, the STRM assumes that the surfaces are diffuse-emitting and diffuse-reflecting. This just means that the radiant properties of the surface are constant for all angles of radiation emission or reflection. The STRM also assumes that each surface in the network is isothermal (at a single temperature). What makes the STRM different is that it allows for surfaces to be semi-transparent and have a non-zero transmissivity. These semi-transparent surfaces are assumed to not affect the path of the transmitted radiation (i.e., semi-transparent surface cannot be a lens).

3.3 Effective View Factors

The only major difference between the NRM and the STRM is that the NRM uses geometric view factors, while the STRM uses effective view factors. Geometric view factors are based entirely upon the geometric shape of the two surfaces exchanging radiation and their position relative to one another. Effective view factors are not only dependent upon the surfaces'

shapes and relative position, but they also are based upon the transmissivity of the exchanging surfaces and any surfaces directly obstructing that radiation exchange. Effective view factors are valid for any set of surfaces, including geometries with opaque and semi-transparent surfaces. Effective view factors are an extension of geometric view factors in that they allow radiation that is transmitted through a semi-transparent surface to eventually hit a second surface. The purpose of effective view factors is to track where the radiation leaving a surface can be absorbed or reflected by another surface. These effective view factors allow a modified version of the NRM (the STRM) to be applied to geometries that include semi-transparent surfaces.

To aid in the explanation of effective view factors, an example enclosure, shown in Figure 14, will be discussed.

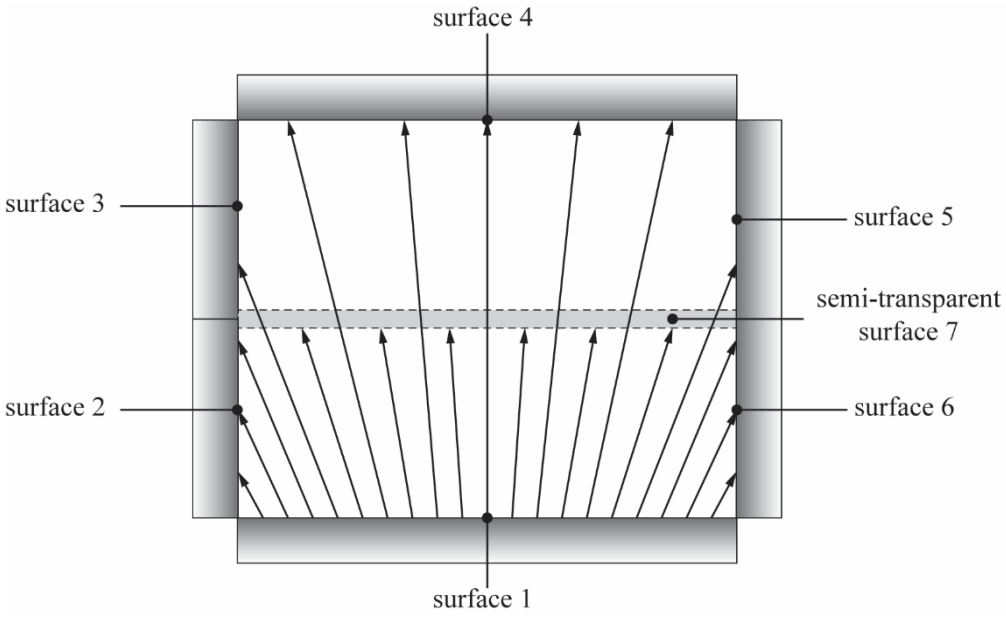

Figure 14: Example surface set for effective view factor discussion.

There are four types of surface-to-surface radiation interactions that must be considered for the enclosure shown in Figure 14:

1. opaque surface to opaque surface that lie on the same side of the semi-transparent surface

2. opaque surface to opaque surface that lie on the opposite side of the semi-transparent surface
3. opaque surface to semi-transparent surface
4. semi-transparent surface to opaque surface

An illustration of an opaque surface to opaque surface interaction on the same side of a semi-transparent surface is shown in Figure 15.

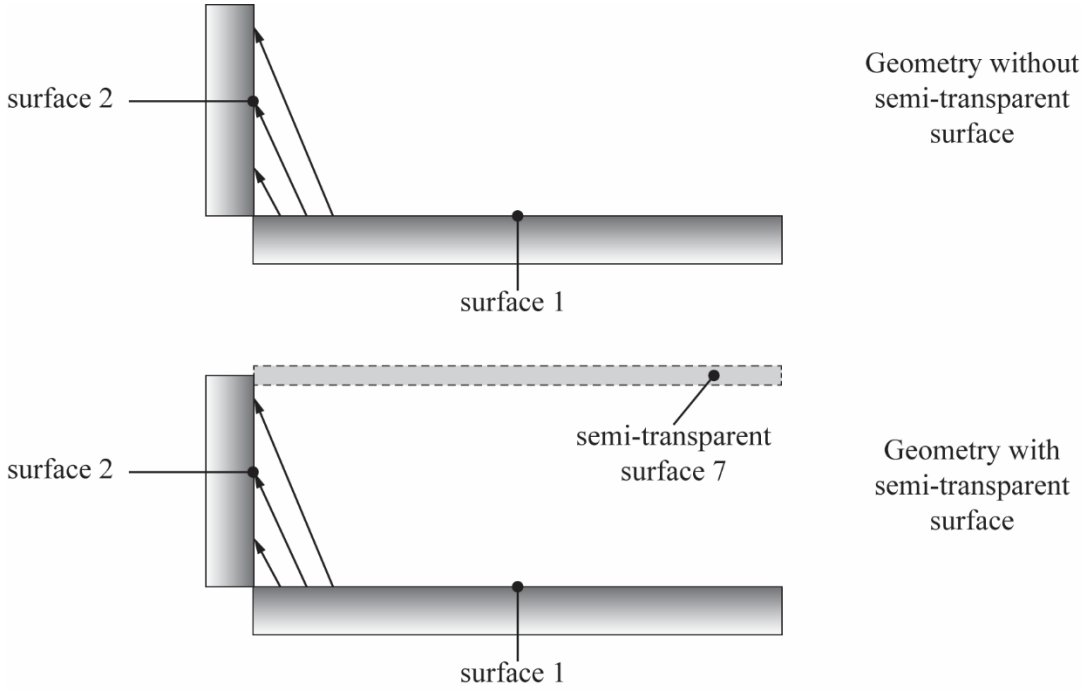

Figure 15: Radiation exchange between opaque surfaces on same side of the semi-transparent surface.

Assuming that the semi-transparent surface 7 is flat, the addition of surface 7 in Figure 15 does not affect the fraction of radiation that leaves surface 1 and directly hits surface 2 because radiation that leaves surface 1 and directly goes to surface 2 will never pass through surface 7. Thus, the effective view factor (denoted with the subscript *eff*) and the geometric view factor (denoted with the subscript *g*) must be the same for this type of interaction:

$$F_{eff,1,2} = F_{g,1,2} \tag{30}$$

This relationship can be more generally written as:

$F_{eff,i,j} = F_{g,i,j}$, where surfaces *i* and *j* are opaque surfaces on the same side of the semi-transparent surface (31)

Radiation exchange between opaque surfaces that lie on opposite sides of the semi-transparent surface is shown in Figure 16.

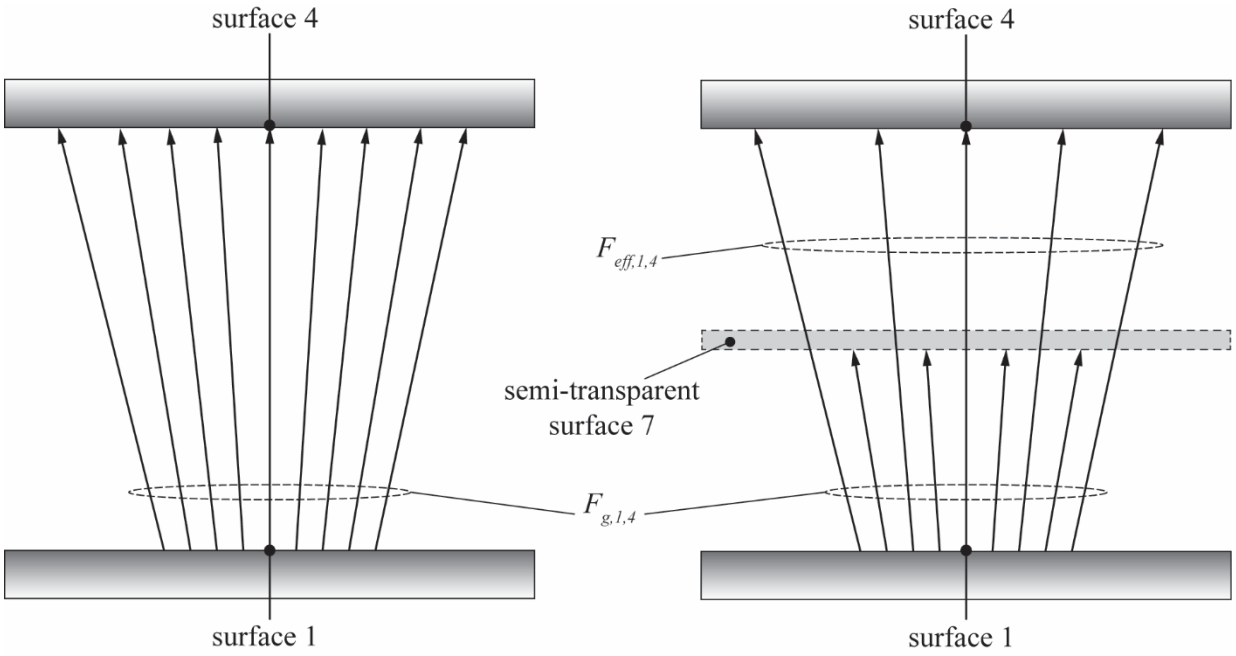

Figure 16: Radiation exchange between opaque surfaces on opposite sides of the semi-transparent surface.

Figure 16 demonstrates that the fraction of radiation that leaves surface 1 and directly reaches surface 4 without reflection from other surfaces is affected by the addition of the semi-transparent surface 7. If the semi-transparent surface were not present, the portion of radiation leaving surface 1 that reaches surface 4 simply would be the geometric view factor, $F_{g,1,4}$. When semi-transparent surface 7 is introduced, some of the radiation that would have travelled to surface 4 is intercepted and either absorbed or reflected by surface 7. Assuming that surface 7 does not affect the direction of radiation (i.e., surface 7 is not a lens), the radiation that is not absorbed or reflected is transmitted through surface 7, and some of it hits surface 4. The fraction of incident radiation that is transmitted through surface 7 is defined by the transmissivity of

surface 7, τ_7. The fraction of radiation leaving surface 1 that reaches surface 4 where it will either be absorbed or reflected is given by:

$$F_{eff,1,4} = F_{g,1,4}\tau_7 \tag{32}$$

where τ_7 is the transmissivity of surface 7, accounting for both reflection at the surface interfaces (in accordance with Snell's and Fresnel's law) and absorption within the glass (in accordance with Bouger's Law) [4]. This concept can be generalized to all situations where the interaction is between two opaque surfaces on opposite sides of the semi-transparent surface, as shown in Eq. (33).

$F_{eff,i,j} = F_{g,i,j}\tau_k$, where i and j are opaque surfaces on opposite sides of the semi-transparent surface k (33)

The third type of radiation exchange is from an opaque surface to the semi-transparent surface. Because the semi-transparent surface does not fully transmit incident radiation, a portion of the radiation that hits it must either be absorbed or reflected as shown in Figure 17.

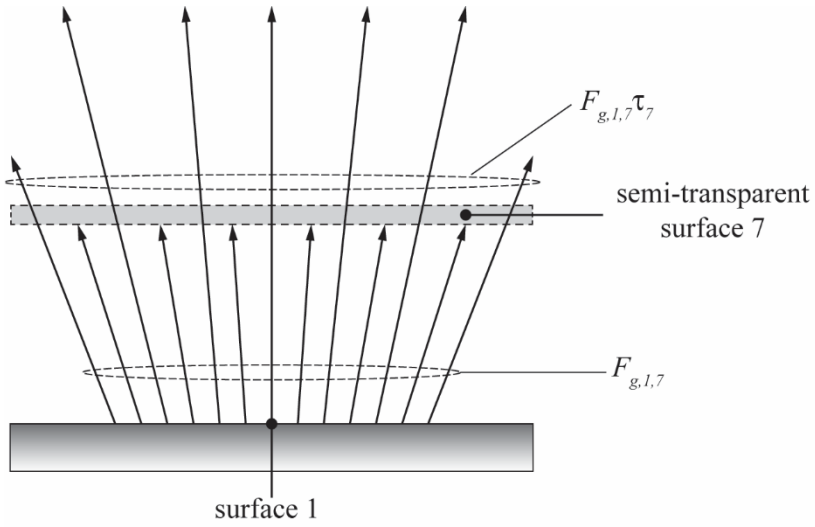

Figure 17: Radiation exchange from opaque surfaces to the semi-transparent surface.

The portion of radiation that leaves surface 1, directly hits surface 7, and is absorbed or reflected by surface 7 is given by Eq. (34):

$$F_{eff,1,7} = F_{g,1,7}\left(1-\tau_7\right) \tag{34}$$

This relationship can be generalized according to:

$F_{eff,i,j} = F_{g,i,j}\left(1-\tau_j\right)$, where i is an opaque surface and j is the semi-transparent surface (35)

The fourth and final type of radiation exchange is from the semi-transparent surface to an opaque surface. Based upon the geometry in Figure 14, the effective view factor from surface 7 to any other surface is calculated through Eq. (36).

$F_{eff,7,j} = F_{g,7,j}$, where j is an opaque surface (36)

Any radiation that leaves the semi-transparent surface 7 will impinge on an opaque surface because there is no other semi-transparent surface and the semi-transparent surface is flat. The effective view factor is simply the geometric view factor. This relationship can be generalized according to:

$F_{eff,i,j} = F_{g,i,j}$, where i is the semi-transparent surface and j is an opaque surface (37)

One important difference between effective and geometric view factors is that effective view factors do not obey the rule of reciprocity. Reciprocity is the relationship between geometric view factors given by:

$$A_i F_{g,i,j} = A_j F_{g,j,i} \tag{38}$$

The reason that the rule of reciprocity does not apply to effective view factors is because their values depend on the transmissivity of the semi-transparent surface. Consider the geometry in Figure 14 and radiation exchange between surfaces 1 and 7. The rule of reciprocity applied to effective view factors would state:

$$A_1 F_{eff,1,7} = A_7 F_{eff,7,1} \tag{39}$$

Substituting in the equations for the effective view factors results in Eq. (40).

$$A_1 F_{g,1,7}\left(1-\tau_7\right) = A_7 F_{g,7,1} \tag{40}$$

Unless τ_7 is 0 (which means the semi-transparent surface is actually opaque), then Eq. (40) contradicts the rule of reciprocity that exists between geometric view factors, given by Eq. (38).

Effective view factors provide a convenient way to identify where radiation that leaves a surface either is absorbed or reflected, even if a semi-transparent surface is present in the surface network. The effective view factors build upon geometric factors by accounting for the transmissivity of semi-transparent surfaces.

3.4 Semi-Transparent Radiosity Method Equations

To investigate radiation exchange in surface networks that include semi-transparent surfaces, the NRM must be modified in several ways. The first modification requires the use of effective view factors instead of geometric view factors. As explained in the previous section, effective view factors describe the fraction of radiation that leaves a surface, hits another surface without reflection, and then is either absorbed or reflected. Figure 18 illustrates a semi-transparent surface experiencing thermal radiation exchange.

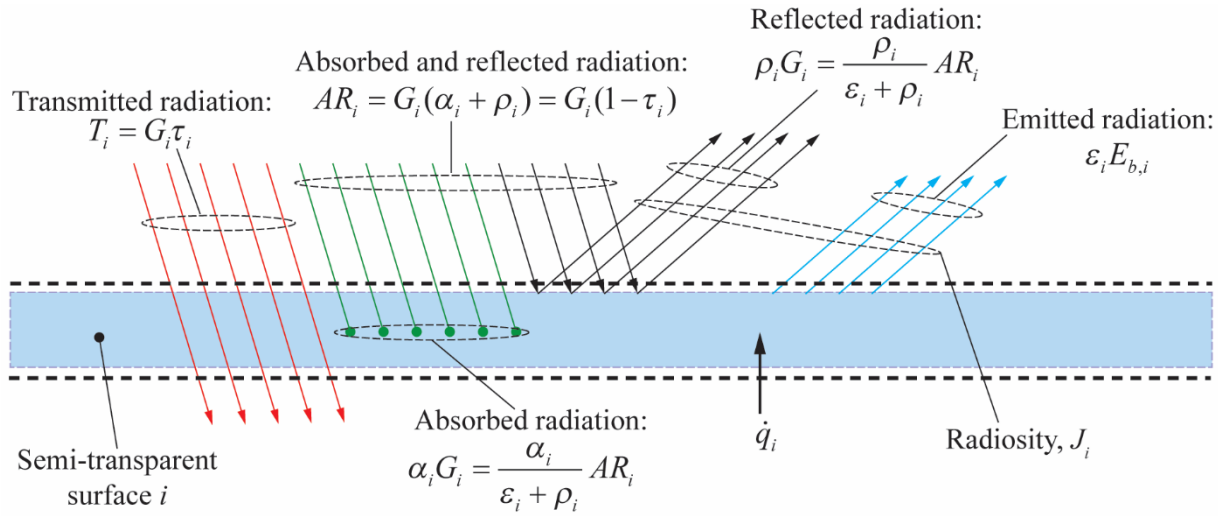

Figure 18: Close-up of the radiation exchange at a semi-transparent surface.

Figure 18 shows incident radiation (or irradiation, G_i), a portion of which is transmitted through the surface:

$$T_i = G_i \tau_i \tag{41}$$

The irradiation that is not transmitted (AR_i) is either absorbed or reflected and given by:

$$AR_i = G_i \left(1 - \tau_i\right) = G_i \left(\alpha_i + \rho_i\right) \tag{42}$$

The portion of incident radiation that is reflected by the surface is:

$$reflected\ radiation = \rho_i G_i \tag{43}$$

The reflected radiation can be related to AR_i by substituting Eq. (42) into Eq. (43). Kirchhoff's Law applies to semi-transparent surfaces, and thus the absorptivity is equal to the emissivity at a specified wavelength [1]. Therefore Eq. (43) can be rewritten as:

$$reflected\ radiation = \frac{\rho_i}{\varepsilon_i + \rho_i} AR_i \tag{44}$$

where ρ_i is the reflectivity and ε_i is the emissivity at a specified wavelength. The emitted radiation is a function of the emissivity and the blackbody emissive power at the wavelength of interest (which is only a function of the surface temperature):

$$emitted\ radiation = \varepsilon_i E_{b,i} \tag{45}$$

According to [5], the emissivity of semi-transparent surfaces is not just a surface property, but in fact a volumetric property. Therefore, the emissivity of a semi-transparent surface will be dependent on the thickness of the surface. A method to determine the emissivity of glass as a function of temperature is provided in [5].

The total radiation leaving surface *i* at any wavelength (i.e., the radiosity of surface *i*) is the sum of the reflected radiation and emitted radiation:

$$J_i = \rho_i G_i + \varepsilon_i E_{b,i} \tag{46}$$

Substituting Eq. (44) into Eq. (46) provides:

$$J_i = \frac{\rho_i}{\varepsilon_i + \rho_i} AR_i + \varepsilon_i E_{b,i} \tag{47}$$

Equation (47) can be rearranged to solve for the absorbed or reflected radiation:

$$AR_i = \frac{J_i\left(\varepsilon_i + \rho_i\right) - \varepsilon_i\left(\varepsilon_i + \rho_i\right)E_{b,i}}{\rho_i} \tag{48}$$

An energy balance on surface *i* yields:

$$\dot{q}_i = A_i J_i - A_i AR_i \tag{49}$$

Substituting Eq. (48) into Eq. (49) leads to:

$$\dot{q}_i = A_i\left(J_i - \frac{J_i\left(\varepsilon_i + \rho_i\right) - \varepsilon_i\left(\varepsilon_i + \rho_i\right)E_{b,i}}{\rho_i}\right) = A_i\left(\frac{-\varepsilon_i J_i + \varepsilon_i\left(\varepsilon_i + \rho_i\right)E_{b,i}}{\rho_i}\right) \tag{50}$$

Equation (50) can finally be rearranged to provide:

$$\dot{q}_i = \frac{A_i \varepsilon_i}{\rho_i}\left(\left(\varepsilon_i + \rho_i\right)E_{b,i} - J_i\right) \tag{51}$$

Equation (51) relates the total energy leaving surface *i* as radiation (J_i) to surface properties (ε_i and ρ_i), the surface area (A_i), the surface temperature (related to $E_{b,i}$), and the rate at which the surface is being heated externally ($\dot{q}$). The total radiation leaving surface *i* that is absorbed or reflected by surface *j* is given by:

$$\dot{q}_{rad,i,j} = A_i F_{eff,i,j} J_i \tag{52}$$

Similarly, the radiation leaving surface *j* that can be absorbed or reflected by surface *i* is:

$$\dot{q}_{rad,j,i} = A_j F_{eff,j,i} J_j \tag{53}$$

Thus, the net radiation transfer from surface *i* to surface *j* is given by:

$$\dot{q}_{i,j} = \dot{q}_{rad,i,j} - \dot{q}_{rad,j,i} = A_i F_{eff,i,j} J_i - A_j F_{eff,j,i} J_j \tag{54}$$

Equation (54) can then be summed over all surfaces to determine the rate of radiation heat transfer from surface *i* to all other surfaces:

$$\dot{q}_i = \sum_{j=1}^{N} \left(A_i F_{eff,i,j} J_i - A_j F_{eff,j,i} J_j \right) \tag{55}$$

Equations (51) and (55) can be applied to an enclosure of *N* surfaces, producing:

$$\dot{q}_i = \frac{A_i \varepsilon_i}{\rho_i} \left(\left(\varepsilon_i + \rho_i \right) E_{b,i} - J_i \right), \quad for\ i = 1..N \tag{56}$$

$$\dot{q}_i = \sum_{j=1}^{N} A_i F_{eff,i,j} J_i - A_j F_{eff,j,i} J_j, \quad for\ i = 1..N \tag{57}$$

Equations (56) and (57) are the principle equations for the STRM. Like the NRM, the STRM uses a linear set of 2*N* equations with 3*N* unknown variables (the net heat transfer rates, blackbody emissive powers, and radiosities). By providing *N* of the unknown variables, Eqs. (56) and (57) can be solved for the remaining unknown values. These equations can be input into an equation solving software to solve for the unknown temperatures and heat transfer rates.

3.5 Example Geometry

To ensure that the STRM performs as expected, consider the example shown in Figure 19.

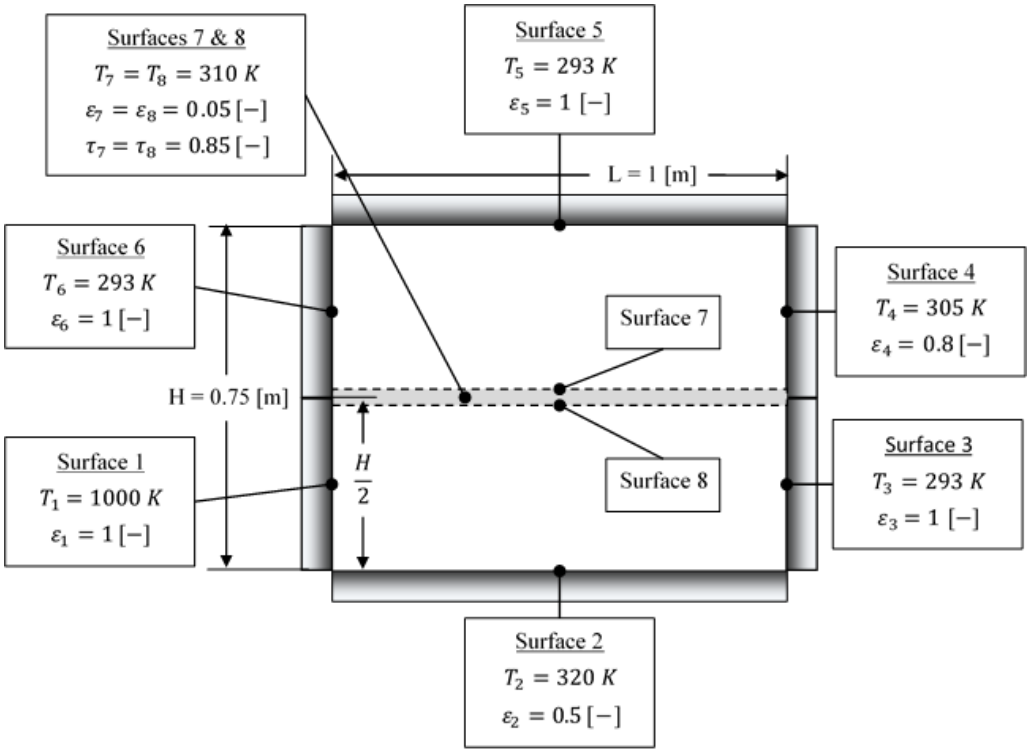

Figure 19: Example problem geometry.

The six outside surfaces are opaque and either black or gray. The internal "surface" actually is composed of two surfaces (surfaces 7 and 8—one on each side). Surfaces 7 and 8 are semi-transparent surfaces that have non-zero transsmisvities. Because surfaces 7 and 8 are separate surfaces, they can have different properties, temperatures, heat transfer rates, etc.—however, this example problem assumes that their radiant properties and temperatures will always be the same. If the transmissivity of surfaces 7 and 8 are set to be 0 (i.e., they are opaque), the STRM applied to the geometry shown in Figure 19 should yield the same results as obtained with the NRM. Table 3 shows a comparison of the results when $\tau_7 = \tau_8 = 0$.

Table 3: Comparison between STRM and NRM: semi-transparent surface acts opaque.

	Net Heat Transfer Rates [kW]	
Surface	STRM	NRM
1	17.454	17.454
2	-9.221	-9.221

3	-7.480	-7.480
4	0.020	0.020
5	-0.019	-0.019
6	-0.006	-0.006
7	0.005	0.005
8	-0.752	-0.752

If the transmissivity of surfaces 7 and 8 are set to 1 (i.e., perfectly transparent), radiation heat transfer occurs as if surfaces 7 and 8 are not present. Table 4 shows a comparison of the results from the STRM with the results from the NRM when $\tau_7 = \tau_8 = 1$.

Table 4: Comparison between STRM and NRM: semi-transparent surface acts transparent.

	Net Heat Transfer Rates [kW]	
Surface	STRM	NRM
1	20.302	20.302
2	-4.328	-4.328
3	-4.519	-4.519
4	-2.893	-2.893
5	-7.991	-7.991
6	-0.571	-0.571
7	0.000	N/A
8	0.000	N/A

The previous two tables verify that the STRM matches the NRM, in the limit that the transmissivity of the semi-transparent surface is either 0 or 1. Now consider the geometry and radiant properties shown in Figure 19. Table 5 presents a comparison of the results from the semi-transparent radiosity method and the CSEM presented in [3].

Table 5: Comparison between the STRM and the CSEM.

	Net Heat Transfer Rates [kW]	
Surface	STRM	CSEM
1	20.086	20.457
2	-4.721	-4.177
3	-4.765	-4.471

4	-2.485	-0.120
5	-6.986	-0.823
6	-0.524	-0.188
7	-0.008	1.506
8	-0.596	-1.547

Because the transmissivities of surfaces 7 and 8 were set to 0 and 1 in Table 3 and Table 4, respectively, the net heat transfer rates in Table 3 and Table 4 serve as outer bounds for the net heat transfer rates of surfaces 1-6. When $\tau_7 = \tau_8 = 0.85$ in Table 5, the net heat transfer rates of surfaces 1-6 should be between the values computed in Table 3 and Table 4. Notice that the STRM obeys these boundaries, while the CSEM produces net heat transfer rates outside of the bounds for surfaces 1-3. Also note the large difference between the methods when calculating net heat transfer rates for surfaces 4-8. These discrepancies arise because the CSEM loses the radiation's directionality when it performs the energy balance on the semi-transparent surface, while the STRM method maintains the radiation's directionality as it transmits through a semi-transparent surface.

The MCM also was performed on the example geometry shown in Figure 19, using the same assumptions required for the STRM and CSEM (i.e., all surfaces are isothermal, diffuse-emitting, and diffuse-reflecting). To ensure that the MCM converged towards a solution, the MCM was run a total of 250 times—25 replicate runs at 10 different values of total simulated rays (N_{rays}). Since the MCM is a stochastic process, for a given value of N_{rays}, the 25 replicate runs produced results that slightly varied from run to run, creating a distribution of calculated surface heat transfer rates with a mean and variance. The replicate runs can be compared to the distribution mean to find the residuals. Figure 20 shows the quantile-normal plot of surface 4's net heat transfer rate residuals when the MCM was run with $N_{rays} = 32{,}000$.

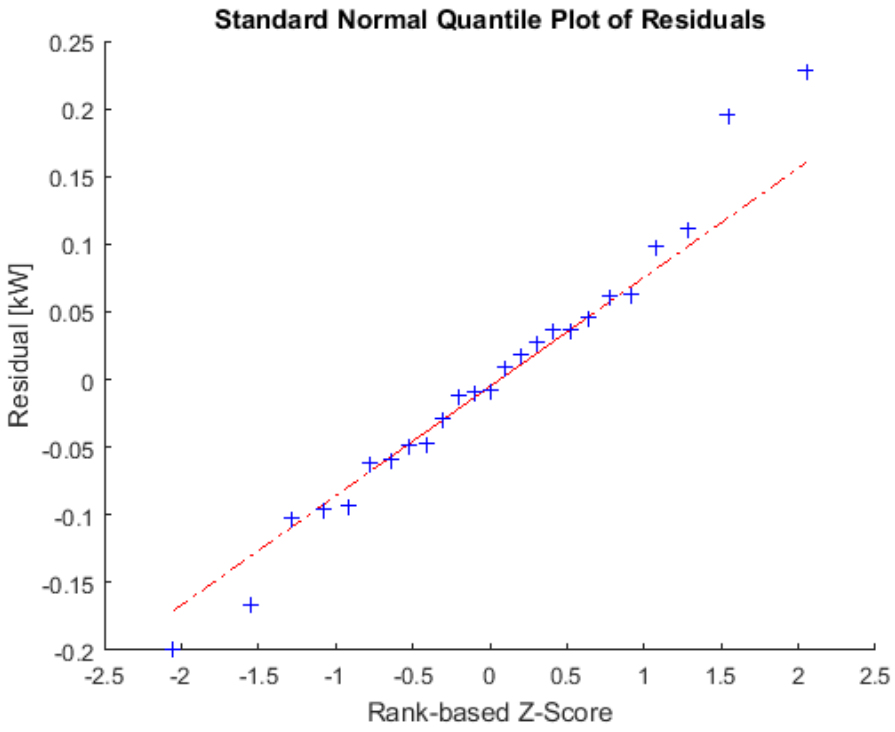

Figure 20: Residual normal-quantile plot of replicate MCM runs.

Because the normal-quantile plot in Figure 20 shows the residuals plot nearly a straight line, the calculated net heat transfer rates can be assumed to be normally distributed, with mean, μ, and variance, σ^2— $\dot{q}_i \sim N(\mu,\sigma^2)$. Since the MCM produces a normal distribution for each surface's net heat transfer rate, confidence intervals can be built to determine how accuracy of the MCM's calculated heat transfer rate. The distribution shown in Figure 20 has 25 replicates, which is a relatively small amount meaning the Student-t distribution should be used in constructing the confidence intervals. For example, the 95% confidence interval for surface 4's net heat transfer rate is determined according to Eq. (58).

$$\dot{q}_{4,CI\ Limits} = \mu \pm t_{\nu=24,\alpha=0.025}\hat{\sigma} \tag{58}$$

where ν is the degrees of freedom (equal to number of replicates minus 1), α is the Type 1 error rate (equal to 1-0.95/2), and $\hat{\sigma}$ is the standard deviation of the distribution.

Figure 21 illustrates the net heat transfer rate leaving surface 4.

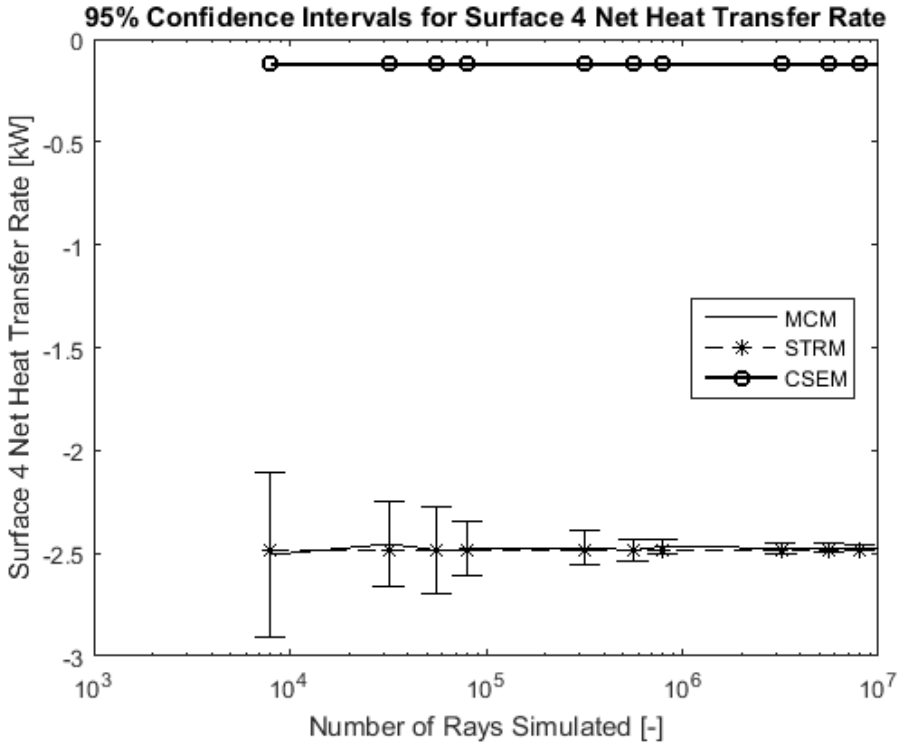

Figure 21: Comparison of the MCM, STRM, and CSEM for semi-transparent example problem.

As the number of rays simulated increased, the MCM converged towards -2.474 kW, with a 95% confidence interval of (-2.478,-2.469) kW. The STRM calculated surface 4's net heat transfer rate to be -2.485 kW. On the other hand, the net heat transfer rate calculated by the CSEM was -0.120 kW. The STRM clearly estimates the net heat transfer rates better than the CSEM because it maintains the directionality of the transmitted radiation.

While the MCM is the most flexible method for modeling thermal radiation, the STRM still offers several distinct advantages over the MCM. The STRM resulted in the same solution as the MCM, but the STRM required far fewer computations than the MCM. Figure 22 illustrates the MCM's confidence interval as a function of the number of calculations. In contrast, because the STRM is essentially a linear system of 2N equations, the Gaussian elimination method suggests that the number of calculations required is given by Eq. (59).

$$N_{calc} = \frac{(2N)^3}{3} \tag{59}$$

The sample problem above could be solved by the STRM in ~1,336 calculations—many orders of magnitude fewer than the MCM.

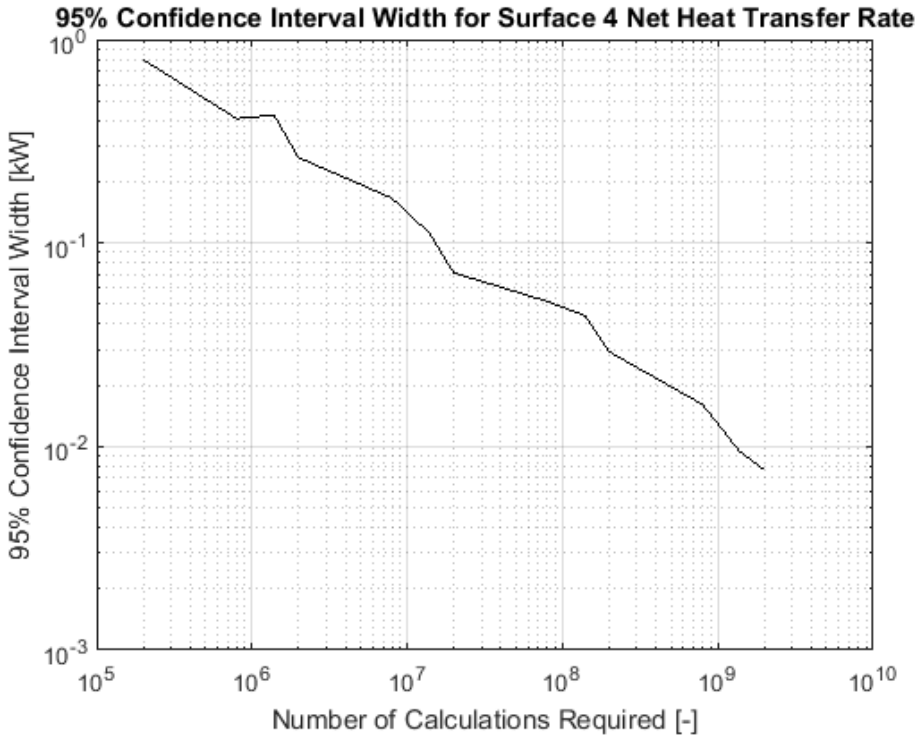

Figure 22: MCM confidence interval as a function of required calculations.

The example problem considered was composed of a simple, 2-D geometry with just 8 surfaces—4 of which were black. As the geometry becomes more complex (more surfaces, 3-D geometry, etc.) the number of computations will significantly increase. Additionally, because the MCM tracks a simulated ray until it is absorbed, as the enclosure surfaces become more reflective the ray of radiation must be tracked for a longer period of time, which requires even more computations. Conversely, the STRM's computational requirements remain relatively unchanged even as the geometry becomes more complicated or the surface properties change; the STRM has very good scalability.

In addition to being more computationally efficient than the MCM, the STRM has the advantage of being able to use surface net heat transfer rates as inputs to the model, and solve for surface temperatures as outputs. In the MCM, the surface temperatures must be specified as an input to solve for the surface heat transfer rates. If the surface heat transfer rates are the known variables, then iteration will be required if using the MCM, which significantly adds to the computationally intensive nature of the MCM. Because the STRM is just a linear system of equations, the surface temperatures, net heat flux rates, or a combination of the two can be specified as inputs to the problem.

3.6 STRM for Semi-Gray Analysis

Thermal radiation can occur at different wavelengths, producing a spectrum of radiation. As described in section 1.2, the spectrum of radiation leaving a surface often depends on the temperature of the surface and its radiant properties. Higher temperature surfaces emit more radiation at short wavelengths while lower temperature surfaces concentrate more radiation at longer wavelengths. Many glasses transmit radiation differently depending on the wavelength radiation. The STRM equations (displayed in Eqs. (56) and (57)) are valid for the total radiation of surfaces 1 through N. In order to model the spectrally-varying behavior of radiation with the STRM, the analysis must be partitioned into smaller wavelength bands where radiant properties can be assumed constant within a given wavelength band. When a surface's properties are broken into wavelength bands where the properties are assumed constant, the surface is considered "semi-gray." For instance, a semi-transparent surface may have the transmission spectrum shown in Figure 23.

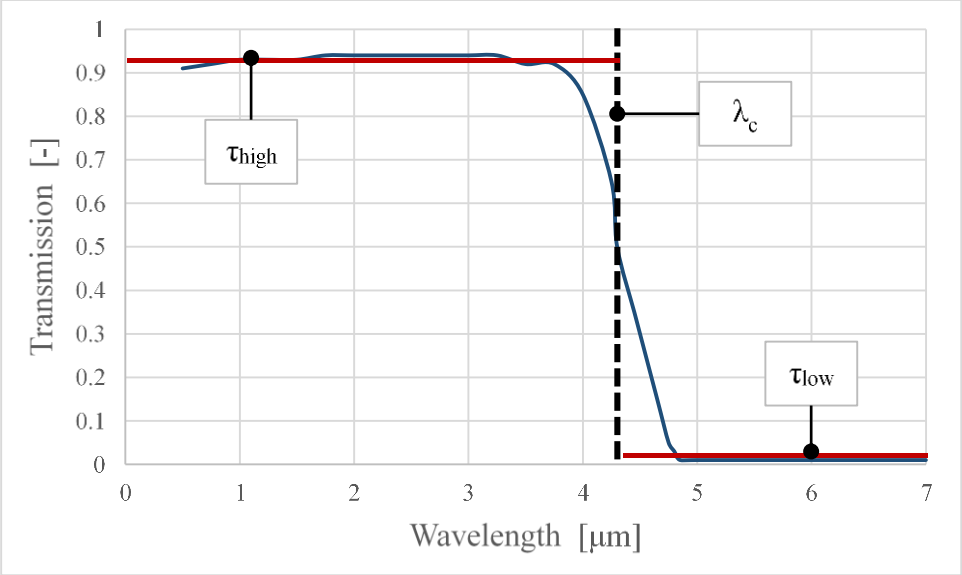

Figure 23: Example transmission spectrum of a semi-gray, semi-transparent surface.

Because the transmission spectrum exhibits relatively constant behavior at wavelengths below and above the cutoff wavelength (λ_c), the analysis can be broken into two wavelength bands. At wavelengths less than λ_c, the transmissivity is equal to τ_{high}, while at wavelengths longer than λ_c, the transmissivity is equal to τ_{low}.

The STRM for semi-gray surfaces uses Eqs. (60) and (61) to determine the net heat transfer rates within each wavelength band of the analysis.

$$\dot{q}_{i,\lambda} = \frac{A_i \varepsilon_{i,\lambda}}{\rho_{i,\lambda}} \left(\left(\varepsilon_{i,\lambda} + \rho_{i,\lambda} \right) E_{b,i,\lambda} - J_{i,\lambda} \right), \quad for\ i = 1..N, \quad for\ \lambda = 1..N_\lambda \tag{60}$$

$$\dot{q}_{i,\lambda} = \sum_{j=1}^{N} A_i F_{eff,i,j,\lambda} J_{i,\lambda} - A_j F_{eff,j,i,\lambda} J_{j,\lambda}, \quad for\ i = 1..N, \quad for\ \lambda = 1..N_\lambda \tag{61}$$

where the subscript λ specifies the wavelength band, and N_λ is the number of wavelength bands. $E_{b,i,\lambda}$ is given by Eq. (62).

$$E_{b,i,\lambda} = f_\lambda \sigma T_i^4 \tag{62}$$

where f_λ is the fraction of the radiation emitted by a blackbody within the wavelength band specified by λ. Because semi-transparent surfaces may have different transmissivities for each wavelength band, a separate set of effective view factors is required for each wavelength band.

In Eqs. (60) and (61), $\dot{q}_{i,\lambda}$ represents the net heat transfer rate leaving surface i that occurs within the λ-wavelength band. To get the total net radiation heat transfer rate leaving surface i, $\dot{q}_{i,\lambda}$ must be summed over all the wavelength bands.

$$\dot{q}_i = \sum_{\lambda=1}^{N_\lambda} \dot{q}_{i,\lambda} \tag{63}$$

This summation is required because the heat transfer rate boundary conditions are typically specified in terms of the total net heat transfer rate of a surface, and thus the set of equations can be solved. The semi-gray analysis is a very convenient extension of the STRM because many semi-transparent materials exhibit transmission spectrums that are a strong function of wavelength.

To demonstrate the semi-transparent radiosity method's application for semi-gray surfaces, consider the geometry in Figure 19. Assume that the semi-transparent surfaces 7 and 8 have radiant properties as shown in Figure 24.

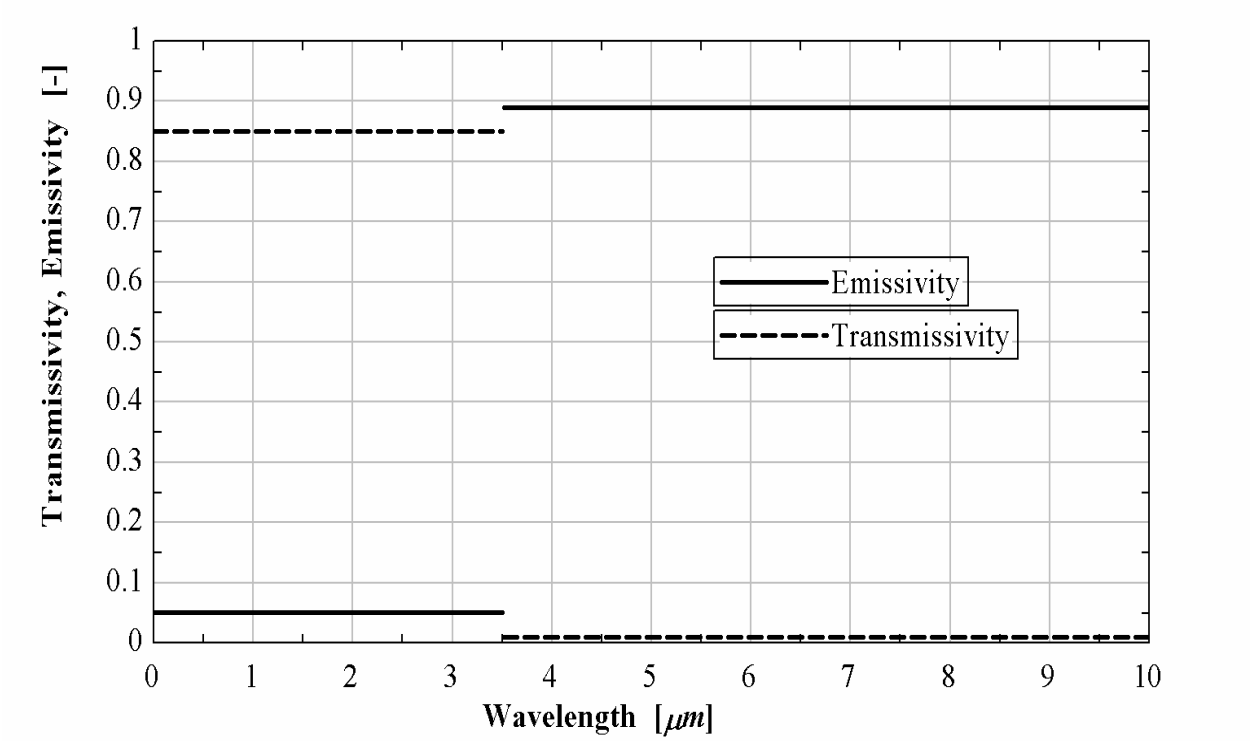

Figure 24: Radiant properties of a semi-transparent surface, semi-gray surface.

Surfaces 7 and 8 are mostly transparent to radiation less than the cutoff wavelength (λ_c), while the surface is nearly opaque for wavelengths longer than λ_c. To handle this semi-gray, semi-transparent surface, the semi-transparent radiosity method must be applied separately within each of the two wavelength bands. Table 6 lists the heat transfer rates in the two wavelength bands for each surface from Figure 19. It also lists the surface temperatures and the net heat transfer rate leaving each surface.

Table 6: Results for semi-gray, STRM example problem.

Surface	Heat Transfer Rates for $\lambda < \lambda_c$ [kW]	Heat Transfer Rates for $\lambda > \lambda_c$ [kW]	Net Heat Transfer Rates [kW]	Temperatures [K]
1	7.755	12.367	20.120	1000
2	-1.852	-2.853	-4.706	320
3	-1.832	-2.943	-4.775	293
4	-0.964	-0.008	-0.972	305
5	-2.674	-0.126	-2.800	293

6	-0.197	-0.023	-0.220	293
7	-0.005	0.083	0.078	310
8	-0.2308	-6.496	-6.727	310

Table 6 demonstrates that the net heat transfer rate is actually the sum of the heat transfer rates in the two wavelength bands. When comparing the net heat transfer rate of surface 4 from Table 6 with the net heat transfer rate of surface 4 from Table 5 (results from semi-transparent example), surface 4 absorbs 1.513 kW less radiation for the semi-gray example. This is because the semi-transparent surface 8 is nearly opaque at wavelengths longer than 3.5 microns, and thus surface 8 prevents much of surface 1's radiation from reaching surface 2 in the long wavelength band. This idea also explains why surface 8 absorbs 6.131 kW more radiation in the semi-gray example.

The MCM and the CSEM can also be extended to analyze semi-gray geometries. Figure 25 below compares the net heat transfer rate of surface 4 for the three different analysis methods.

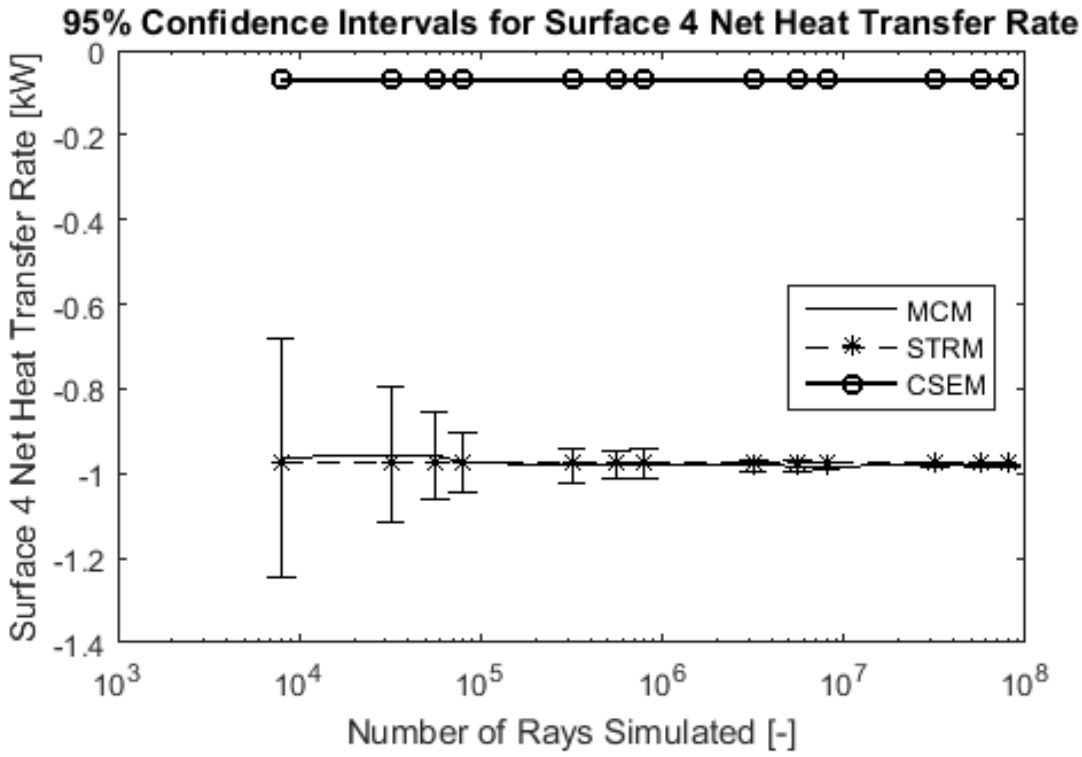

Figure 25: Comparison of the MCM, STRM, and CSEM for semi-gray, semi-transparent example problem.

Figure 25 shows that the MCM solution converges towards the solution found by the STRM as the number of simulated rays increases. The STRM is clearly a more accurate model of thermal radiation than the CSEM.

Ch. 4 Radiation Model of IR Dryer using STRM

The initial drying model discussed in the Ch. 2 determined that the radiant energy from the lamps had the largest impact on the drying process. This initial model made two assumptions regarding the amount of radiation that was absorbed by the corrugated board:

1. The radiation incident on the board (irradiation) is constant (while the board is directly above the dryer) and equal to the blackbody emissive power of the lamp's manufacturer-specified color temperature.
2. The fraction of irradiation absorbed by the front liner is assumed to be f_f.

Since radiation was the dominant mode of heat transfer in the drying process, these two assumptions bear significance on the results of the initial model. To more realistically model the board's absorbed radiation, a radiation model was created to track the dryer's radiation exchange based upon the dryer's specified parameters (i.e., supplied electrical power, lamp type, glass type, clearance height, etc.).

The dryer design presented in Figure 4 includes the protective glass plate, which separates the IR lamps from the substrate. While the CSEM (described in section 3.1 and [3]) could have been used to model the drying process, it would have produced an inaccurate result because it would not have tracked the radiation's direction as it transmitted through the glass plate. The MCM (described in section 3.1) certainly could have model the drying process, as well, but the heavy computational requirements of the technique rendered the technique undesirable. The semi-gray extension of the STRM (derived in Ch. 3) was the best technique for the modeling the thermal radiation exchange for the dryer in Figure 4.

4.1 Geometry

The dryer radiation model tracks how thermal radiation is exchanged between all surfaces involved in the drying process. Figure 3 in 0 shows two pictures of the IR dryer that the radiation model replicated. The IR dryer in Figure 3 shows the outside stainless steel cassette, equipped with four cylindrical IR lamps. The cassette surfaces directly exposed to the IR lamps are tinted and polished for a reflective finish; the large, back surface with the reflective coating is termed the reflector. The narrow slots in the reflector allow the dryer's forced air to actively cool the lamps' bulbs, which keeps the lamps from overheating and breaking. Figure 3 also depicts the glass plate, the protective metal rods, and the air jet holes.

To model the radiation exchange using the STRM, the IR dryer was broken down into the geometry shown in Figure 26.

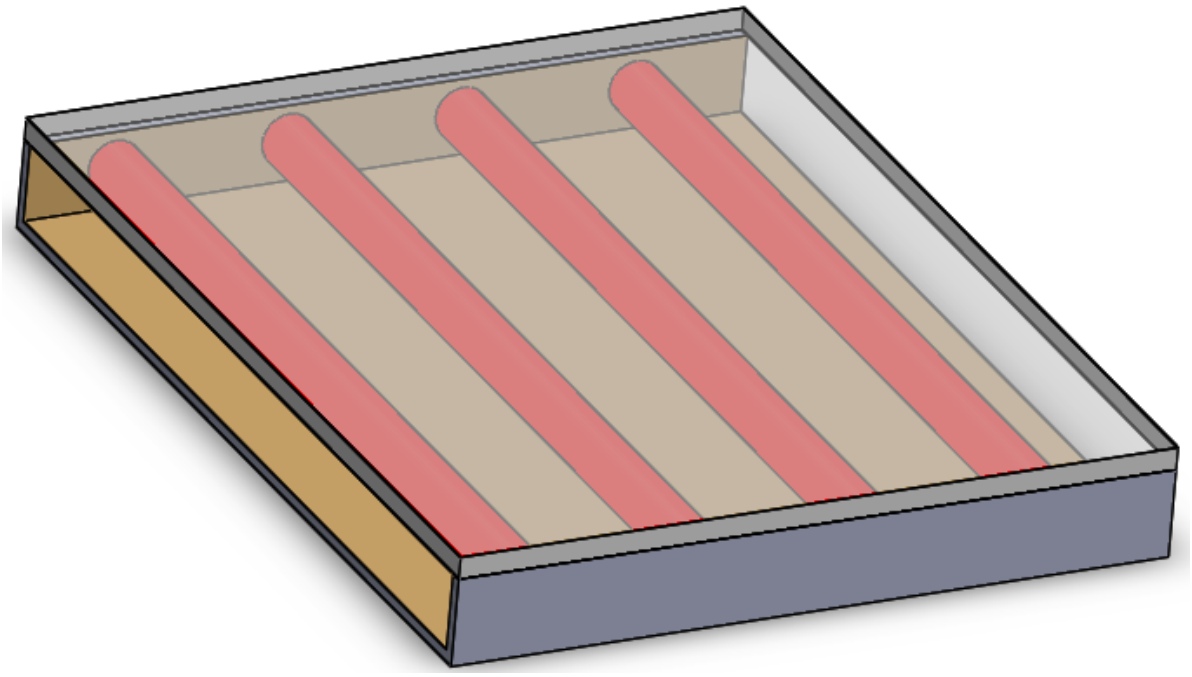

Figure 26: Simplified geometry of a single IR dryer.

The model geometry consists of the reflective surfaces, the IR lamp bulbs, and the glass plate. The dryer geometry shown in Figure 26 is slightly different than the geometry shown in

Figure 3. The lamps in Figure 3 are mounted at a slight angle in the dryer, while the bulbs in Figure 26 are aligned with the cassette length. The angle the lamps are mounted at is small enough that there will be no discernable difference in the overall radiation exchange. The geometry in Figure 26 also does not include the metal rods. The rods were omitted from the analysis because their surface area was small compared to the other surfaces, and so the rods contributed very little to the radiation exchange. The geometry in Figure 26 does not model the narrow slots in the reflector. Like the metal rods, the narrow slots were small in comparison to the other surfaces and hardly affected the radiation exchange. Even though the slots were not physically modeled in the geometry, the convection process they were designed for was still be applied within the model.

The simplified geometry shown in Figure 26 only shows the surfaces for one cassette. In reality, the drying stations on an offset printing press typically have approximately 18 cassettes installed side-by-side to cover the full width of the press. To ensure that the model was more representative of the actual drying process, the surfaces of three cassettes were modeled. The final layout of the dryer surfaces is shown in Figure 27.

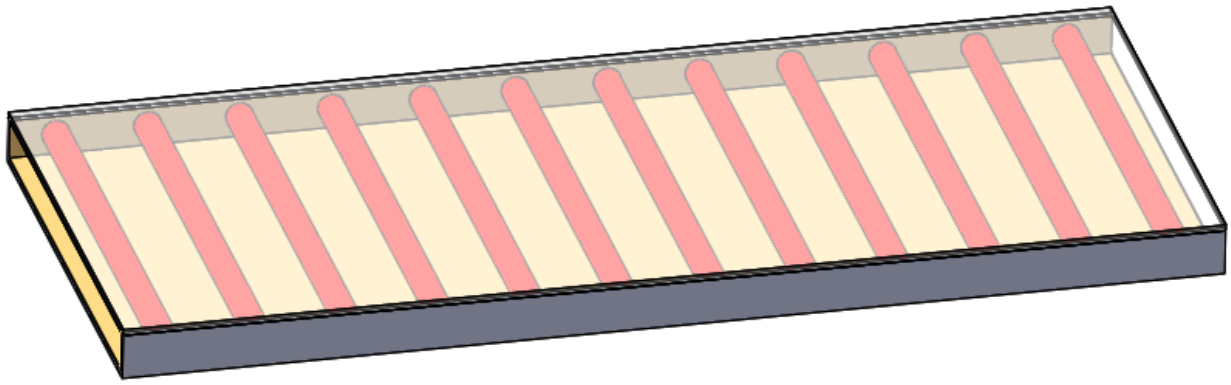

Figure 27: Dryer surfaces for dryer radiation model.

There are 19 surfaces from the dryer that are modeled, including:

1. 12 IR lamp bulbs

2. 2 vertical reflective surfaces
3. 2 vertical sides open to the surroundings
4. 1 back reflector surface
5. 2 surfaces associated with the glass plate (1 surface for each side of the glass plate)

A top view of the model geometry is shown in Figure 28.

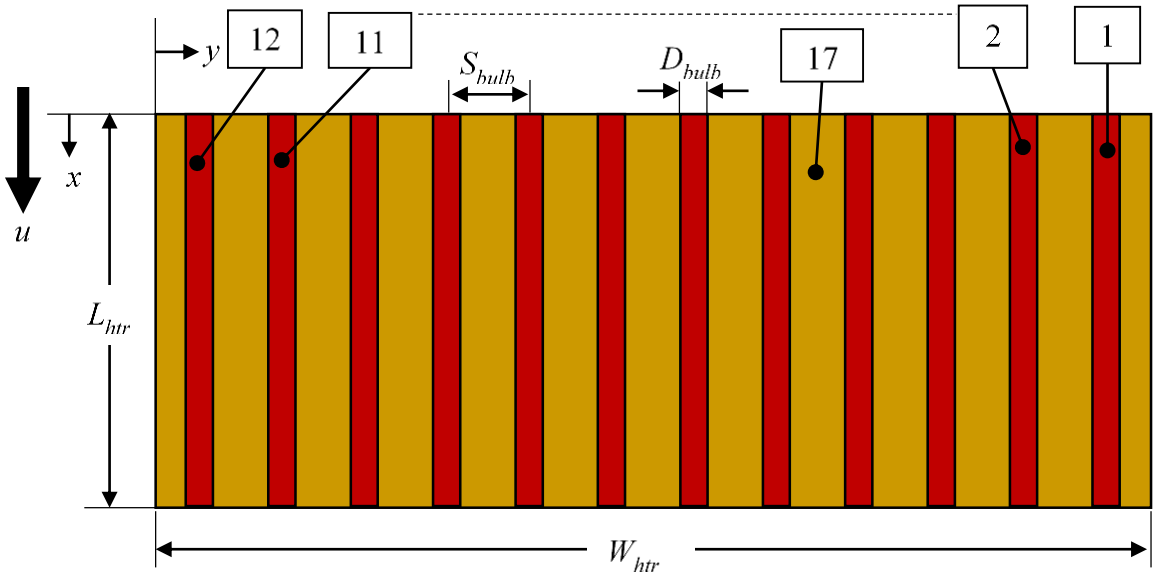

Figure 28: Top view of dryer radiation model geometry..

The geometry in Figure 28 shows the identifying surface number of the bulbs (1-12), and the surface number of the back reflector (17). It also shows the length and width of the dryer (L_{htr} and W_{htr}, respectively), as well as the bulb diameter and axial spacing between the bulbs (D_{bulb} and S_{bulb}, respectively). To provide some reference of how the dryer is oriented, the substrate velocity, u, is indicated by the bold arrow to the left, showing that the substrate would be traveling parallel to the lamps' axes.

A detailed, profile, section view of the model geometry is shown in Figure 29.

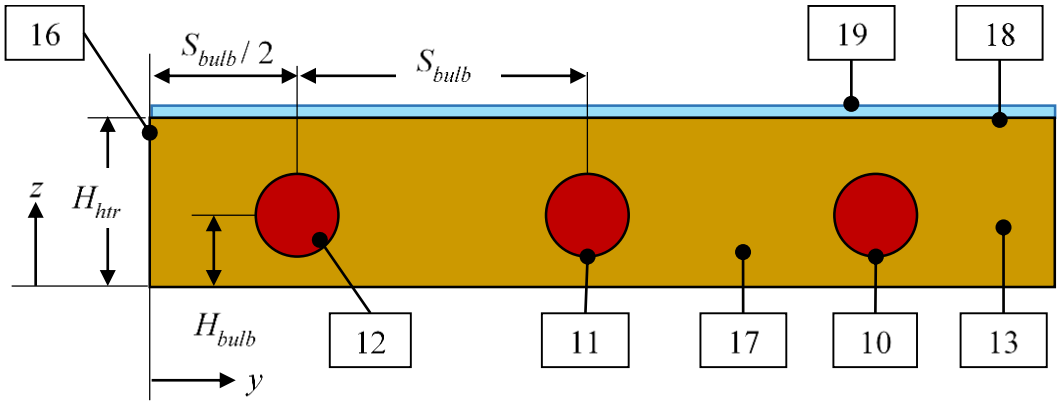

Figure 29: Profile view of dryer radiation model geometry.

The detailed profile view of the model geometry shows the dryer height (H_{htr}) and bulb height (H_{bulb}). The illustration also shows the dryer surfaces' associated numbers: the three lamps are numbered 10-12, the reflector is number 17, the vertical side reflector (at $x = 0$) is 13, and the vertical open side surface (at $y = 0$) is 16. While the other open vertical side on the opposing side (at $y = W_{htr}$) is not shown, that surface is numbered 15. Finally, the glass plate has two surfaces—18 is the dryer side of the glass plate and 19 is the substrate side of the glass plate.

The side view of the model geometry is shown in Figure 30.

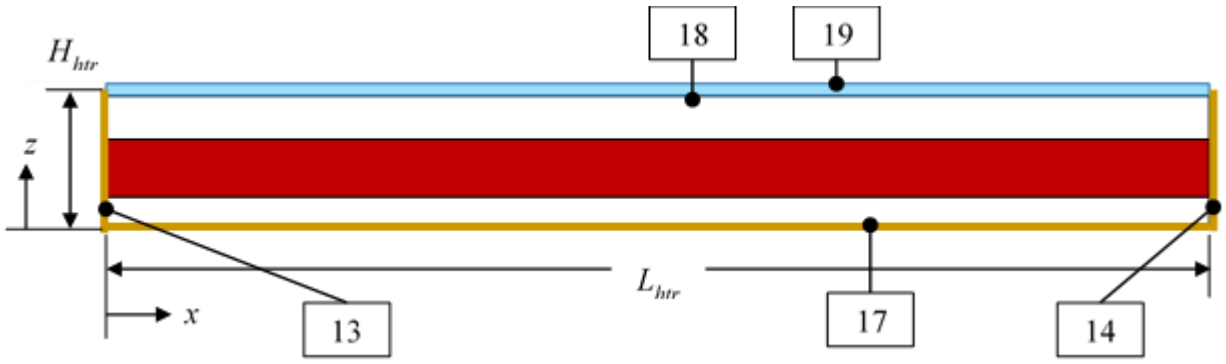

Figure 30: Side view of dryer radiation model geometry.

The geometry described thus far only included the dryer surfaces, but the model also simulated the substrate surface—assumed to be corrugated board. Figure 31 shows an auxiliary view of the corrugated board surface situated over the dryer geometry. The modeled corrugated board surface only included the portion of the board that was directly over the dryer cassettes.

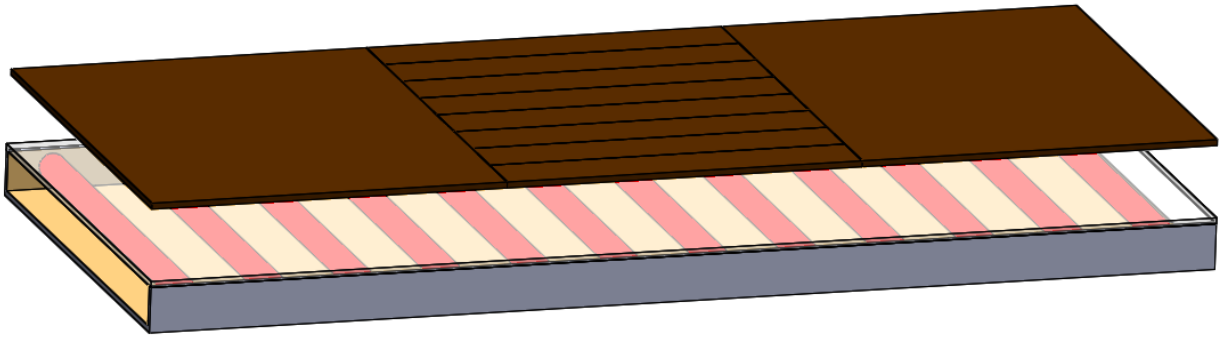

Figure 31: Dryer radiation model geometry with corrugated board.

Figure 31 shows the board split into 10 different surfaces—two large surfaces on the right and left side and eight strip-surfaces in the center. The radiation model used the STRM to analyze the radiation exchange; as described in Ch. 3, one of the required assumptions of the STRM is that all of the modeled surfaces are considered to be isothermal (at one temperature) and the net heat transfer rate for a surface applies to the entire surface. To model the board with a spatially-varying heat transfer rate, the board surface was split into smaller, separate surfaces so that the constant heat transfer rate STRM assumptions still applied. The board was broken into these 10 different surfaces because the corrugated board will experience different radiation exchange depending on the location being analyzed.

Just by visual inspection, the center eight surfaces of the board were predicted to receive more radiation than the two large outside surfaces because the outside surfaces were more exposed to the open surroundings than the center eight surfaces. The calculated heat transfer rates of these outside surfaces did not provide a good estimate of the actual radiation exchange within a dryer on a printing press (where there are typically 18 cassettes mounted next to each other). This was the reason why the surfaces of three cassettes were modeled. Only the center section of the board was useful in estimating the radiation exchange of the drying process.

The center of the board was divided into the eight strip surfaces in order to estimate how the radiation was distributed spatially. The radiation from the IR dryer was foreseen to be

distributed unequally, with the outer strips receiving less radiation and the center strips receiving more radiation. The initial drying model described in Ch. 2 assumed that the radiation incident on the board was constant while the board was directly over the dryer, and equal to the blackbody emissive power of the lamps' color temperature. By breaking the center surface into eight strips, the dryer radiation model was able to provide the spatially-varying radiation absorbed by the board as it passes over the dryer.

Figure 32 and Figure 33 depict the top and side view of the board surfaces and their relation to the dryer geometry.

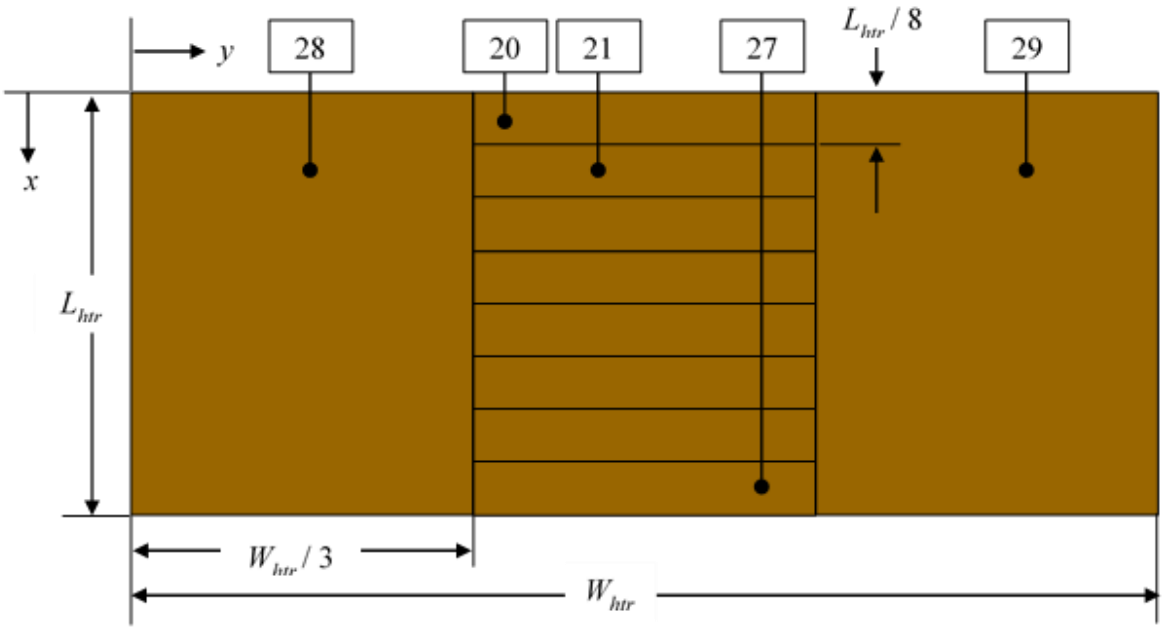

Figure 32: Top view of the dryer radiation model board surfaces.

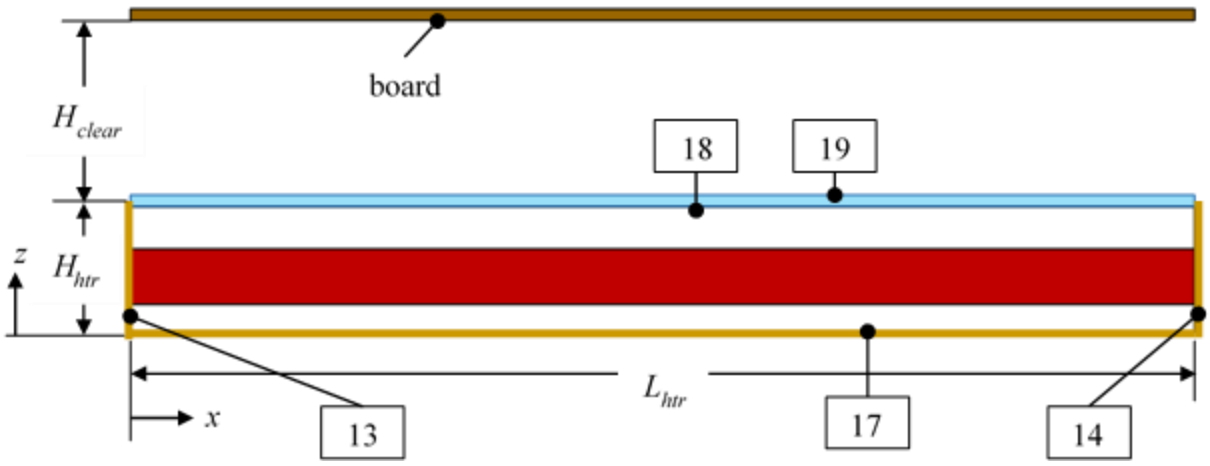

Figure 33: Side view of dryer radiation model surfaces with board.

Figure 32 shows that the board was first split into three equal sized sections, and then the center of those three sections was broken into 8 equally-sized strips. The clearance height, H_{clear}, is shown in Figure 33 as the normal distance between the glass plate and the board.

Figure 28 through Figure 33 graphically explain the variables used in the dryer geometry. The numerical values used and description of these variables are presented in Table 7.

Table 7: Dryer radiation model geometry parameters.

Description	Symbol	Nominal Value
Dryer length	L_{htr}	7.44 in
Dryer width (includes all 3 cassettes)	W_{htr}	17.82 in
Dryer height	H_{htr}	0.875 in
Bulb diameter	D_{bulb}	11 mm
Bulb height (reflector to bulb axis)	H_{bulb}	0.36 in
Bulb spacing (bulb axis to axis)	S_{bulb}	1.49 in
Clearance height	H_{clear}	1.27 in

The final “surface” for the enclosure geometry was the surroundings. Figure 33 shows that the radiation from the IR lamps that transmitted through the glass either hit the board surface, or shot off into the surrounding environment. The surrounding environment was modeled with the STRM by combining the enclosing surfaces into one “surface” that was black

(ε = 1, ρ = 0, τ = 0), had an infinite area (A_{surr} = 9e99 m^2), and was at the ambient temperature, T_{amb}.

The first step for implementing the STRM was calculating the areas of each surface. The surface area of each bulb was defined by:

$$A_i = \pi D_{bulb} L_{lit}, \quad for\ i = 1,12 \tag{64}$$

L_{lit} is the lighted length of the bulb, which is determined by the lamp's filament length; L_{lit} depends on the lamp type. A single bulb is shown in Figure 34, illustrating the L_{lit} dimension.

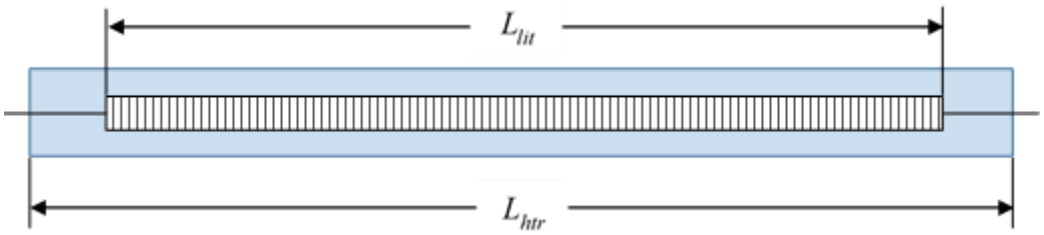

Figure 34: Filament length vs lamp length.

The remaining surface areas were calculated according to Eqs. (65) through (70).

$$A_{13} = A_{14} = W_{htr} H_{htr} - 12\left(\frac{\pi}{4} D_{bulb}^{\ 2}\right) \tag{65}$$

$$A_{15} = A_{16} = L_{htr} H_{htr} \tag{66}$$

$$A_{17} = A_{18} = A_{19} = L_{htr} W_{htr} \tag{67}$$

$$A_i = \frac{L_{htr}}{8}\frac{W_{htr}}{3}, \quad for\ i = 20,27 \tag{68}$$

$$A_{28} = A_{29} = L_{htr}\frac{W_{htr}}{3} \tag{69}$$

$$A_{30} = 9e99\ m^2 \tag{70}$$

4.2 Semi-Gray Analysis

The dryer radiation model used the STRM to track the radiation exchange within the enclosure geometry described in section 4.1. The dryer's thermal radiation exchange originates at the IR lamps. As described in section 1.2, the amount and spectral distribution of the radiation from the lamps is determined by the supplied electrical power and the filament diameter size. The three lamps considered included the medium wave (MW), fast-response medium wave (FRMW), and short wave (SW). A comparison of the lamps' filaments was shown in Figure 5 of section 1.2. Even if the same amount of electrical energy was dissipated in the three lamps, the spectral distribution of the radiation leaving the lamps differed due to the differences in the lamps' filament geometries. When supplied with the same amount of electrical energy, Figure 35 plots the three lamps' blackbody distributions (the lamps are assumed to be operating at their respective color temperatures, as indicated in Figure 35).

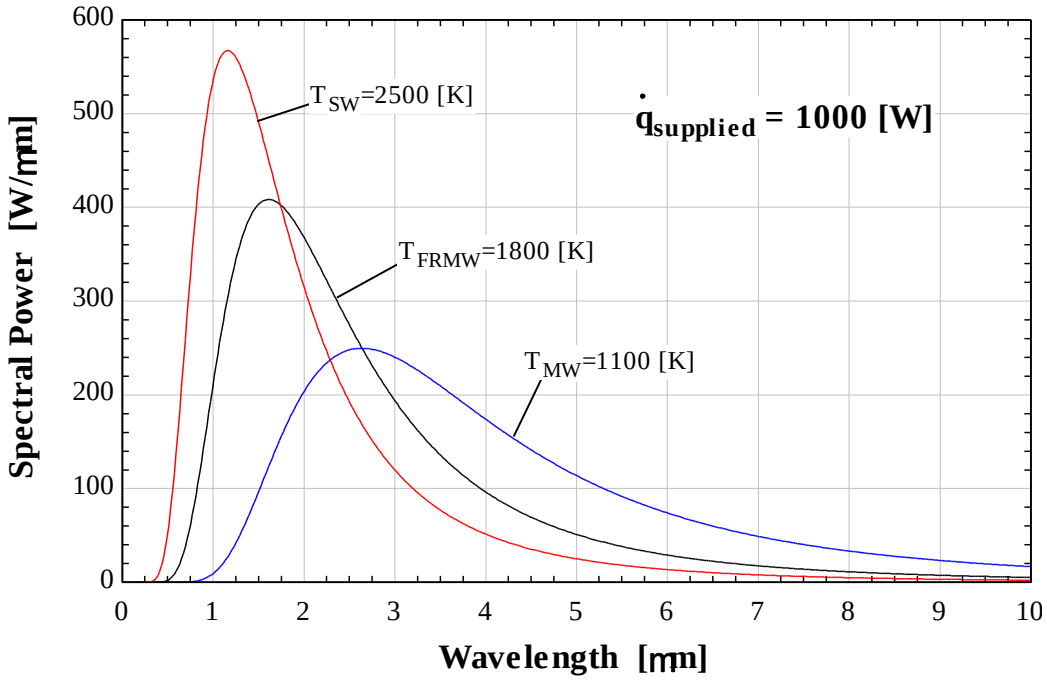

Figure 35: Blackbody curves of the lamps at their specified color temperature.

For a lamp's radiation to reach the substrate, the radiation emitted from the filament must be transmitted through both the lamp bulb and the glass plate. Glasses typically have radiant properties that are a strong function of wavelength, as shown in Figure 36. Figure 36 depicts the transmission spectrums of quartz 214 glass [6], quartz 124 glass [6], and ceramic glass [7]. All three types of IR lamps used quartz 214 glass for their bulbs. The two glass plates considered in the dryer radiation model are the quartz 124 glass and the ceramic glass.

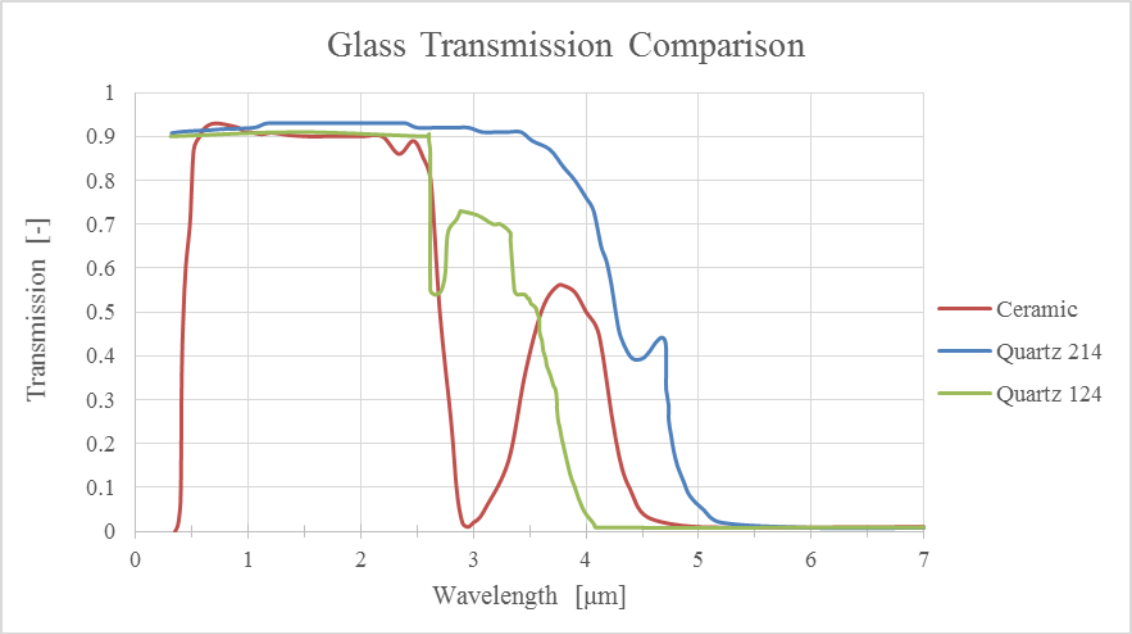

Figure 36: Transmission spectrums of ceramic and quartz glass.

Figure 36 shows that the glasses are nearly transparent to radiation at short wavelengths, but virtually opaque to radiation at longer wavelengths. Figure 35 and Figure 36 clearly show that the lamp type and the glass type affect the spectral distribution of the radiation travelling from the lamps to the corrugated board. But the lamp and glass type likely do not independently affect the spectrum of the board's applied radiation—the interaction of the lamp and glass type probably determine the board's incident radiation. Figure 37 overlays the spectral distributions shown in Figure 35 with the quartz 124 transmission curve.

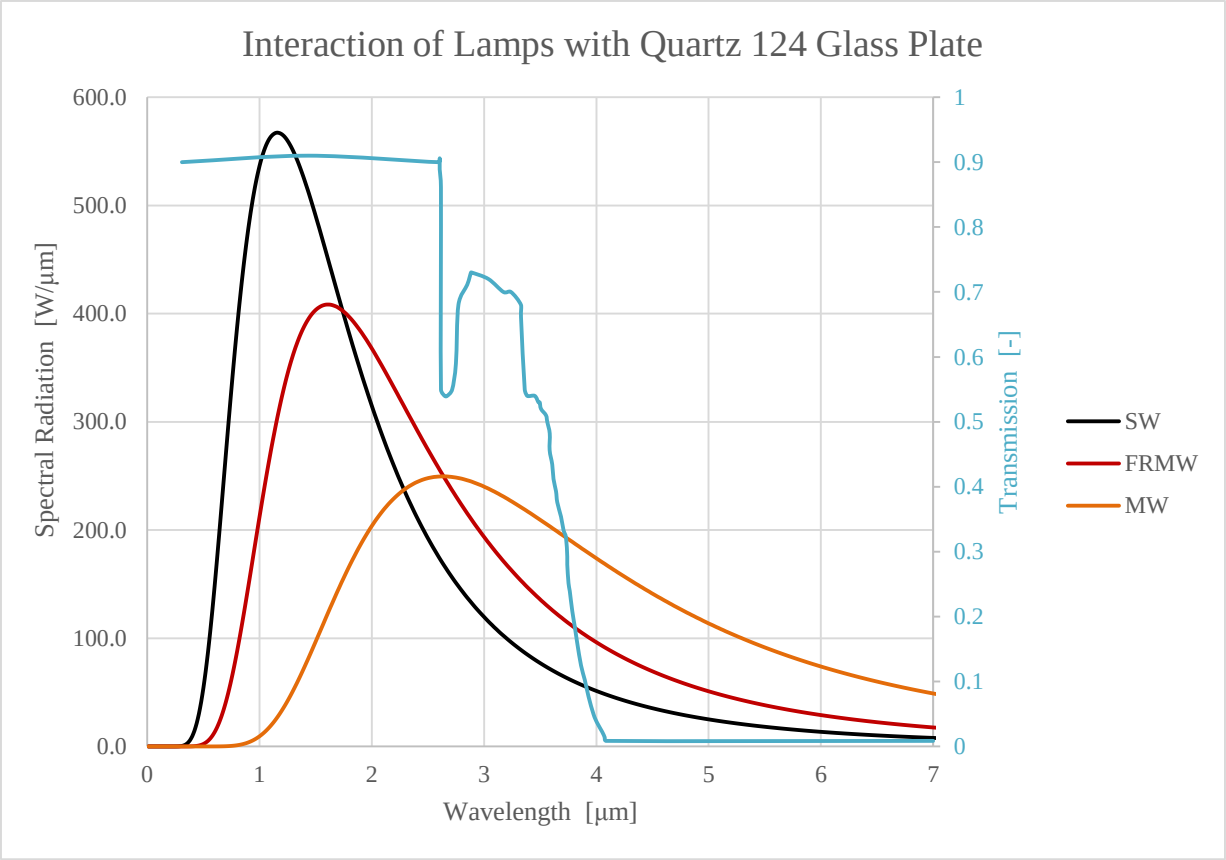

Figure 37: Lamps' blackbody curves with the transmission spectrum of quartz 124 glass.

Figure 37 shows that bulbs with a higher color temperature emit more radiation at shorter wavelengths where the glass plate is the most transparent. Low color temperature bulbs spread out the spectral distribution to longer wavelengths, causing a larger percentage of its emitted radiation to be absorbed/reflected by the glass. For instance, the quartz 124 transmission curve in Figure 37 illustrates that radiation at wavelengths longer than ~4 µm will not be transmitted through the glass. Table 8 provides quantitative evidence regarding the relative amount of radiation emitted at different wavelengths depending on the lamp type.

Table 8: Percentage of radiation emitted at wavelengths less than 4 µm.

Lamp Type	**Percent of Emitted Radiation**		
	$\lambda < 2.5$ µm	**2.5 µm $< \lambda <$ 4.0 µm**	**$\lambda >$ 4.0 µm**
MW	21.7%	33.2%	45.1%

FRMW	56.4%	25.5%	18.1%
SW	75.8%	15.6%	8.6%

The SW lamp emits 75.8% of its radiation at wavelengths less than 2.5 μm (where quartz 124's transmissivity is approximately 0.9)—much higher than 56.4% and 21.7% from the FRMW and MW lamps, respectively. The SW lamp only emits 8.6% of its radiation emitted at wavelengths greater than 4 μm, where the quartz 124 acts opaque. The FRMW and MW emit 18.1% and 45.1%, respectively, in this opaque wavelength-region. Because the glass plate is transparent where high color temperature lamps emit most of their radiation, but opaque where low color temperature lamps emit more of their radiation, the presence of the glass will have a greater negative impact on the lower color temperature lamps.

Clearly, the combination of lamp and glass type affects the distribution of the radiation spectrum, and likewise, the amount of radiation that reaches the corrugated board. For this reason, the radiation model utilized the semi-gray extension of the STRM. The surfaces that required these semi-gray properties include the lamp bulbs and the glass plate. EES (the equation solver used for the radiation model) limits the number of variables in a program, and because there are a large number of required variables for the STRM, the number of wavelength bands in the radiation model was limited to eight. The wavelength bands were determined based upon radiant properties of the glasses, such that spans of wavelengths where the properties remained relatively constant were assigned to be a wavelength band. Table 9 lists the wavelength bands and the radiant properties of the semi-gray surfaces.

Table 9: Radiant properties of the semi-gray, semi-transparent surfaces in model.

Wavelength Band			**Quartz 214**			**Quartz 124**			**Ceramic**		
Band	Lower Bound	Upper Bound	ε	ρ	τ	ε	ρ	τ	ε	ρ	τ
1	0.00	2.50	0.03	0.05	0.92	0.06	0.05	0.89	0.05	0.05	0.90

2	2.50	2.75	0.03	0.05	0.92	0.40	0.05	0.55	0.30	0.05	0.65
3	2.75	3.25	0.03	0.05	0.92	0.26	0.05	0.69	0.87	0.05	0.08
4	3.25	3.50	0.03	0.05	0.92	0.38	0.05	0.57	0.66	0.05	0.29
5	3.50	4.00	0.10	0.05	0.85	0.74	0.05	0.21	0.43	0.05	0.52
6	4.00	4.25	0.25	0.05	0.70	0.99	0.05	0.00	0.60	0.05	0.35
7	4.25	5.00	0.53	0.05	0.42	0.99	0.05	0.00	0.90	0.05	0.05
8	5.00	1000	0.99	0.01	0.00	0.99	0.05	0.00	0.94	0.05	0.01

Figure 38 through Figure 40 plot the transmission spectrums of the three semi-gray, semi-transparent surfaces, and overlay each of the eight wavelength bands' transmissivity.

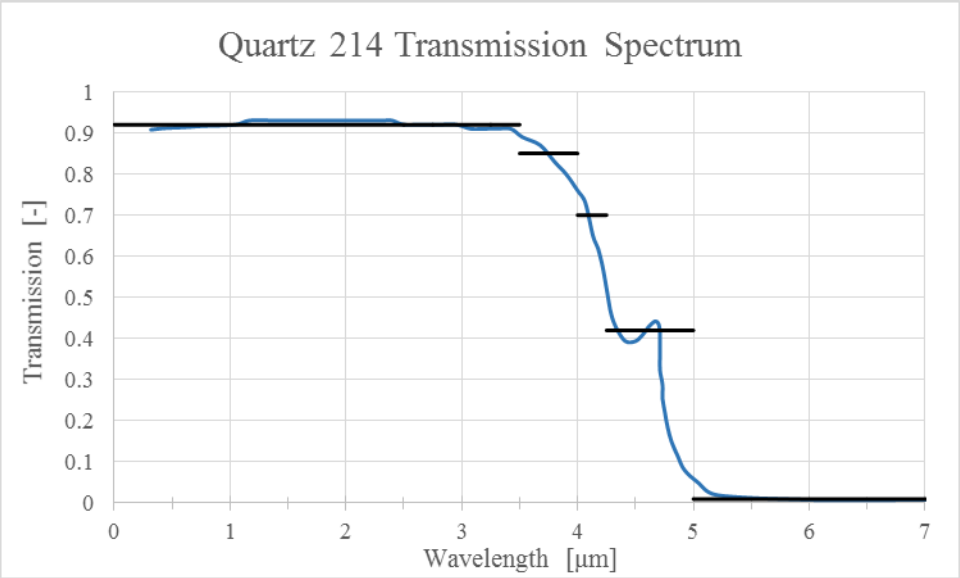

Figure 38: Transmission spectrum of quartz 214 glass.

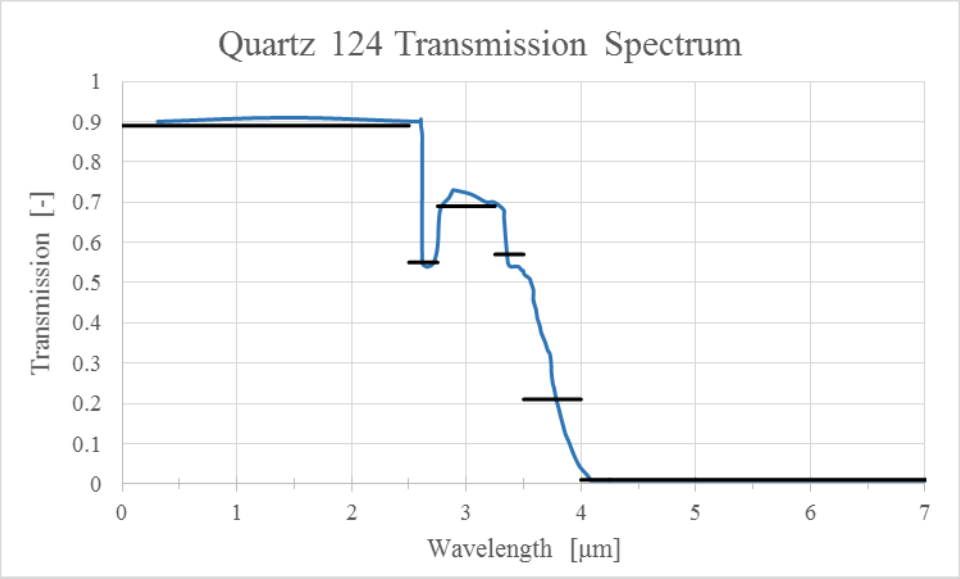

Figure 39: Transmission spectrum of quartz 124 glass.

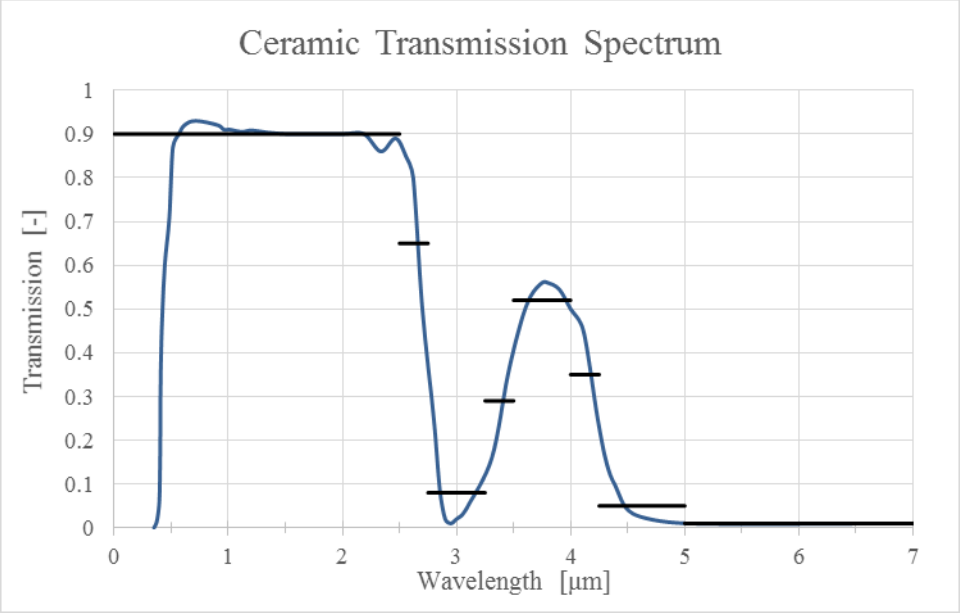

Figure 40: Transmission spectrum of ceramic glass.

While Figure 38 through Figure 40 and Table 9 provide the radiant properties of the semi-gray surfaces, the other surfaces in the model are considered to have constant properties at all wavelengths. Table 10 lists all of the surfaces in the model, with their respective radiant properties.

Table 10: Radiant properties for all surfaces in the model.

Surface	Description	ε	ρ	τ
1-12	Bulbs	See Table 9, quartz 214	See Table 9, quartz 214	See Table 9, quartz 214
13-14	Vertical side reflector (at $x = 0$, $x = L_{htr}$)	0.05	0.95	0.00
15-16	Vertical side openings (at $y = 0$, $y = W_{htr}$)	1.00	0.00	0.00
17	Reflector	0.05	0.95	0.00
18-19	Glass Plate	See Table 9, quartz 124 or ceramic	See Table 9, quartz 124 or ceramic	See Table 9, quartz 124 or ceramic
20-29	Board	0.95	0.05	0.00
30	Surroundings	1.00	0.00	0.00

4.3 Monte Carlo Geometric View Factors

Section 3.3 explained how the STRM utilizes effective view factors to perform the radiation analysis. The first step in calculating the effective view factors is determining all pairs of possible geometric view factors. Because analytical equations for the specific dryer geometry were not available, the geometric view factors were determined numerically with the Monte Carlo technique. Similar to the MCM described in section 3.1, the Monte Carlo technique for calculating geometric view factors simulates emitting large quantities of random rays of radiation from a surface one at a time, tracking where that ray travels, and finding which surface the ray first intersects. The MCM for complete radiation analysis differs from the Monte Carlo technique for geometric view factors because the full MCM actually assigns an amount of energy to each ray, and continues tracking that ray until it is absorbed by another surface (even if the ray is first transmitted through or reflected off an intermediate surface). The Monte Carlo technique for calculating geometric view factors only follows the ray of radiation until it first intersects another surface. By knowing the total number of rays emitted from surface *i*, and the total

number of rays that directly hit surface *j*, the geometric view factor can be calculated according to Eq. (71).

$$F_{g,i,j} = \frac{\#\ rays\ emitted\ \ from\ surface\ i\ that\ hit\ surface\ \ j}{\#\ rays\ emitted\ \ from\ surface\ i} \tag{71}$$

The Monte Carlo technique is stochastic in nature, and thus large quantities of rays need to be simulated to ensure that the calculated answer is known within some error margin. One question that could arise is that if the Monte Carlo technique is required to determine the geometric view factors, why not just perform the entire analysis with the MCM? Every time the MCM is run for a full radiation analysis, large numbers of rays must be simulated which requires substantial computing power and time. On the other hand, the STRM with Monte Carlo geometric view factors requires that the Monte Carlo technique only be run once to determine the set of geometric view factors; the determined set of geometric view factors can be saved and re-accessed in future runs of the STRM. Therefore the STRM using Monte Carlo geometric view factors still holds major time and computational advantages over the MCM.

The Monte Carlo geometric view factors were coded in MATLAB, with each geometric view factor consisting of two main functions—the *F* function and the *hit* function. The *F* function took in important geometry parameters about the surfaces and then determined random ray emission locations on the specified emitting surface. During execution, the *F* function called the *hit* function, sending it the current ray emission location and other geometric parameters. The *hit* function randomly selected a ray direction (according to Lambert's Cosine Law, explained in [8], for diffuse emitters) and emitted the radiation in that random direction from the emission point. The ray was incrementally lengthened and continuously checked to see if the ray intersected a surface in the model geometry. When the ray hit a surface, the *hit* function recorded the impinged surface number and returned that hit surface number to the *F* function.

The *F* function incremented a hit counter that logged a tally of the number of rays that leave the emitted surface and directly hit each of the other modeled surfaces. After the specified number of rays had been emitted from the surface, the number of rays that hit each surface was divided by the total number of emitted rays which provided a calculation of the geometric view factors. The explained procedure is displayed in graphical form, in Figure 41.

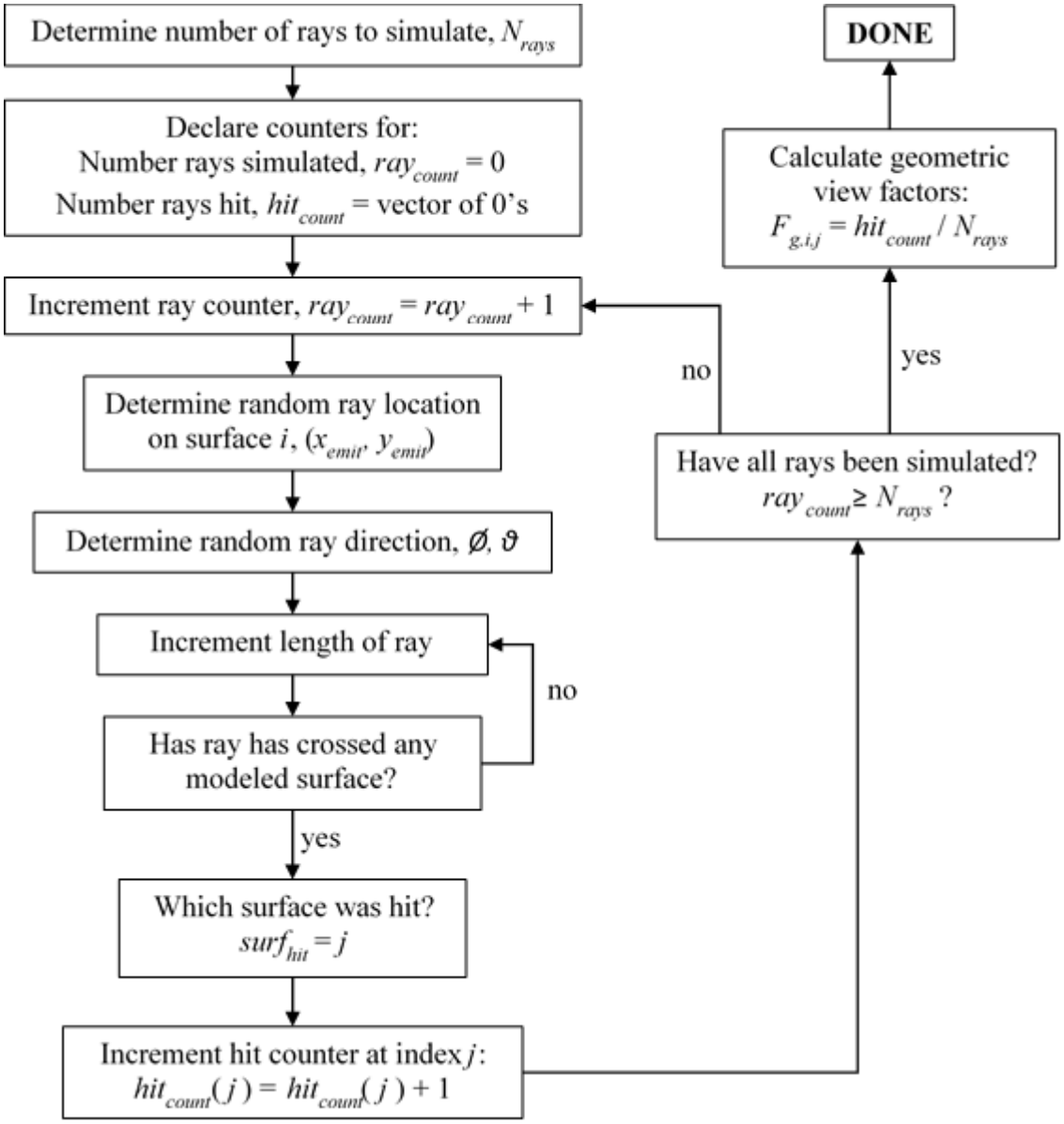

Figure 41: Workflow of Monte Carlo technique for geometric view factors.

The dryer radiation model did not require that all geometric view factors be calculated with the Monte Carlo technique, as some of the geometric view factors were determined from view factor libraries and the rules that govern geometric view factors (reciprocity and enclosure). The model surfaces chosen to be emitting surfaces for the Monte Carlo technique were 13 (vertical side reflector at $x = 0$), 16 (vertical side opening at $y = 0$), 17 (reflector), and 20-29 (all board surfaces). To learn more about the implementation of the Monte Carlo geometric view factors, please see the MATLAB codes provided in the electronic supplement, as outlined in Appendix C:.

4.4 Boundary Conditions

Section 3.4 explained that a combination of surface temperatures and/or net heat transfer rates must be supplied as inputs to the model for the STRM to solve for the remaining surface temperatures and heat transfer rates. The radiation model used the boundary conditions outlined in Table 11 to determine the radiation exchange.

Table 11: Radiation model boundary conditions for STRM.

Surface	Surface Description	Boundary Condition	Boundary Condition Description
1-12	IR lamp bulbs	$\dot{q}_{rad,i,\lambda} = \dot{q}_{bulb,\lambda}$, $for\ i = 1..12 \quad for\ \lambda = 1..8$	Specified spectral heat transfer rate (determined from lamp radiation model)
13-14	Vertical reflector sides	$T_i = T_{reflector} - \Delta T_{reflector}$, $for\ i = 13,14$	Vertical reflector sides are slightly colder than the reflector
15-16	Vertical side openings	$T_i = T_{surr}, \quad for\ i = 15,16$	Specified surroundings temperature
17	Vertical reflector	$T_{17} = T_{reflector}$	Specified temperature
18-19	Glass plate	$T_{18} = T_{19}$	Each side of the glass surface is at the same temperature

18-19	Glass plate	$-\dot{q}_{tot,18} = \dot{q}_{tot,19}$	There is no energy storage in the glass plate—any energy coming into the glass must leave the other side
20-29	Board surfaces	$T_i = T_{board,i}, \quad for\ i = 20, 29$	Specified temperature for each individual board surface
30	Surroundings	$T_{30} = T_{surr}$	Specified surroundings temperature

The radiation exchange in the drying process begins at the IR lamps. The dryer radiation model geometry only included the external surface of each IR lamp's bulb; the geometry did not include the filament or the internal bulb surface. As explained in section 4.2, the total and spectral radiation leaving the bulb surface is determined by the filament geometry, the supplied electrical power, and the bulb transmission spectrum. In order to specify the lamps' spectral radiation heat transfer rate boundary condition that was representative of these characteristics, a second radiation model was created to simulate the radiation exchange in the lamp.

The lamp radiation model is a 1-D radiation model that used the semi-gray, STRM to determine the spectrum of radiation that leaves the bulb surface towards the surroundings. Figure 42 provides an illustration of the geometry for the lamp radiation model.

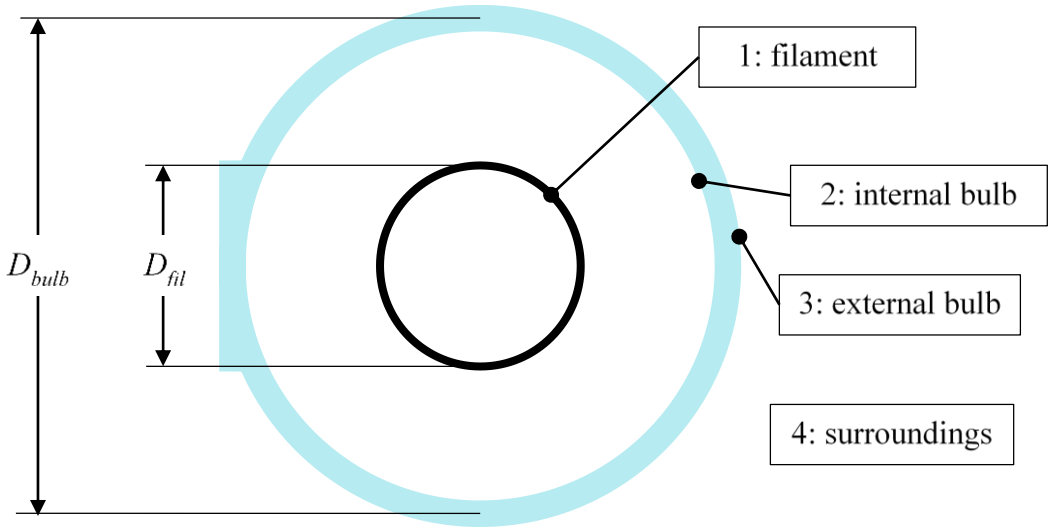

Figure 42: Geometry for lamp radiation model.

The model was assumed to be 1-D because the cylindrical bulbs have a length-to-diameter ratio of ≈17, which is large enough that the edge effects of the bulbs will contribute little to the overall radiation exchange. Furthermore, there were no circumferential variations in the bulb properties, so the radiation exchange was only a function of the radial dimension. The filament in Figure 42 was modeled as a continuous cylindrical surface with diameter, D_{fil}. The comparison of IR lamps and filaments in Figure 5 shows that the lamp filaments are actually composed of wire, tightly wound into a helical cylinder or some other complex shape. Approximating the filament as a continuous cylinder was a sufficient because all three filaments are compactly wound.

The areas of each surface wes calculated according to Eqs. (72) through (74).

$$A_1 = \pi D_{fil} L_{lit} \tag{72}$$

$$A_2 = A_3 = \pi D_{bulb} L_{lit} \tag{73}$$

$$A_4 = 9e99\ m^2 \tag{74}$$

The geometric view factors of the external side of the filament were determined solely by inspection, as shown in Eqs. (75) and (76).

$$F_{g,1,1} = F_{g,1,3} = 0\,[-] \tag{75}$$

$$F_{g,1,2} = F_{g,1,4} = 1\,[-] \tag{76}$$

Knowing the geometric view factor from the filament to the internal bulb surface, the rule of reciprocity stated that the geometric view factor from the internal bulb surface to the filament was known equalled the ratio of the surface diameters:

$$F_{g,2,1} = \frac{A_1}{A_2} \cancel{F_{g,1,2}}^{=1} \rightarrow F_{g,2,1} = \frac{\cancel{\pi} D_{fil} \cancel{L_{lit}}}{\cancel{\pi} D_{bulb} \cancel{L_{lit}}} = \frac{D_{fil}}{D_{bulb}} \tag{77}$$

The geometric view factor from the inside of the bulb to itself was determined via the enclosure rule.

$$F_{g,2,2} = 1 - F_{g,2,1} = 1 - \frac{D_{fil}}{D_{bulb}} \tag{78}$$

Since the inside bulb surface never directly "sees" the external bulb, the geometric view factor to the external bulb surface was given by:

$$F_{g,2,3} = 0\,[-] \tag{79}$$

In order for the radiation from the internal bulb surface to reach the surroundings, the radiation must hit the internal bulb surface and transmit through the bulb. Thus the geometric view factor from the internal bulb surface to the surroundings was the same as the view factor from the internal bulb surface to itself.

$$F_{g,2,4} = F_{g,2,2} = 1 - \frac{D_{fil}}{D_{bulb}} \tag{80}$$

The geometric view factors from surface 3 to the other surfaces were determined by inspection, and obey Eqs. (81) and (82).

$$F_{g,3,j} = 0\,[-], \quad for\ j = 1..3 \tag{81}$$

$$F_{g,3,4} = 1\,[-] \tag{82}$$

Because the surroundings were an all-encompassing "surface", the geometric view factors from the surroundings to the other surfaces were calculated through the rule of reciprocity and the enclosure rule.

$$F_{g,4,j} = \frac{A_j}{A_4} F_{g,j,4}, \quad for\ j = 1..3 \tag{83}$$

$$F_{g,4,4} = 1 - F_{g4,1} \tag{84}$$

The filament and the surroundings were assumed to be blackbodies, which means they absorb and emit all possible radiation ($\varepsilon = 1$, $\rho = 0$, $\tau = 0$). The bulb (surfaces 2 and 3) was assumed to have the quartz 214 properties, described in Table 9. These semi-transparent, semi-gray properties required separate sets of effective view factors within each wavelength band. The effective view factors from the filament to all surfaces were calculated according to Eqs. (85) through (87).

$$F_{eff,1,1,\lambda} = F_{g,1,1,\lambda}, \quad for\ \lambda = 1..8 \tag{85}$$

$$F_{eff,1,j,\lambda} = F_{g,1,j,\lambda}\left(1 - \tau_{j,\lambda}\right), \quad for\ j = 2,3, \quad for\ \lambda = 1..8 \tag{86}$$

$$F_{eff,1,4,\lambda} = F_{g,1,4,\lambda}\tau_{2,\lambda} \tag{87}$$

The effective view factors for the other surfaces were calculated similarly, according to the process described in section 3.3.

To determine the maximum amount of radiative power that could be emitted by a surface in each wavelength, the spectral blackbody emissive power was determined by Eq. (88).

$$E_{b,i,\lambda} = f_{i,\lambda}\sigma T_i^4, \quad for\ i = 1..4, \quad for\ \lambda = 1..8 \tag{88}$$

where $f_{i,\lambda}$ is the fraction of the blackbody's total power that is emitted in the wavelength band λ, σ is the Stefan-Boltzmann constant, and T_i is the surface temperature of surface i. The semi-gray, STRM equations are applied as described in section 3.6, and shown in Eqs. (89) and (90).

$$\dot{q}_{rad,i,\lambda} = \frac{A_i \varepsilon_{i,\lambda}}{\rho_{i,\lambda}}\left(\left(\varepsilon_{i,\lambda} + \rho_{i,\lambda}\right)E_{b,i,\lambda} - J_{i,\lambda}\right), \quad for\ i = 1..4, \quad for\ \lambda = 1..8 \tag{89}$$

$$\dot{q}_{rad,i,\lambda} = \sum_{j=1}^{8} A_i F_{eff,i,j,\lambda} J_{i,\lambda} - A_j F_{eff,j,i,\lambda} J_{j,\lambda}, \quad for\ i = 1..4, \quad for\ \lambda = 1..8 \tag{90}$$

Because this was a semi-gray analysis, the total net radiation leaving each surface was given by the sum of the radiation heat transfer rates in all wavelength bands:

$$\dot{q}_{rad,tot,i} = \sum_{\lambda=1}^{8} \dot{q}_{rad,i,\lambda} \tag{91}$$

On the printing press, the bulbs are cooled by forced air (at ambient temperature, T_{amb}) from a fan. This convection was modeled by applying a convection coefficient to each surface. Only the external bulb surface experiences convection, so surface 3 was the only surface with a non-zero convection coefficient.

$$\bar{h}_i = \begin{cases} 0\ \dfrac{W}{m^2 K}, & for\ i = 1, 2, 4 \\ 30\ \dfrac{W}{m^2 K}, & for\ i = 3 \end{cases} \tag{92}$$

where $\bar{h}_i$ is the convection coefficient of surface i. The convective heat transfer rate was given by Eq. (93).

$$\dot{q}_{conv,i} = \bar{h}_i A_i \left(T_i - T_{amb}\right) \tag{93}$$

The total heat transfer rate of energy leaving a surface was then determined by an energy balance on each of the surfaces, shown in Eq. (94).

$$\dot{q}_{tot,i} = \dot{q}_{rad,tot,i} + \dot{q}_{conv,i}, \quad for\ i = 1..4 \tag{94}$$

Like the dryer radiation model, this lamp radiation model required a set of boundary conditions. In the drying process, the lamps are supplied with electrical power, thus the boundary condition at the filament equates the supplied electrical power with the total heat transfer rate of the filament:

$$\dot{q}_{tot,i} = \dot{q}_{supply} \tag{95}$$

The lamp radiation model assumed that the internal and external surfaces of the bulb were at the same temperature, and there was no energy stored in the bulb.

$$T_2 = T_3 \tag{96}$$

$$\dot{q}_{tot,3} = -\dot{q}_{tot,4} \tag{97}$$

The final boundary condition set the temperature of the surroundings to the ambient temperature:

$$T_4 = T_{amb} \tag{98}$$

This lamp radiation model allowed the user to specify the filament diameter, the supplied electrical power, and the bulb transmission spectrums as inputs, and then determined the spectral distribution of the radiation leaving the bulb (which included radiation from the filament that was transmitted through the bulb, and radiation directly emitted from the bulb surface). Because the surroundings were considered to be black, all of the radiation leaving the lamps was absorbed by the surroundings eventually.

$$\dot{q}_{rad,4,\lambda} = \dot{q}_{bulb,\lambda}, \quad for\ \lambda = 1..8 \tag{99}$$

where $\dot{q}_{bulb,\lambda}$ is the amount of radiation (both transmitted and emitted) leaving the bulb in wavelength band, λ. The spectral radiation leaving the lamp bulb, $\dot{q}_{bulb,\lambda}$, was then supplied as an input to the dryer radiation model, and used as the boundary condition for the lamp bulbs (surfaces 1-12).

In addition to the spectral radiation leaving the bulbs, the lamp radiation model estimated the filament temperature and the bulb temperature. The estimated filament temperature was checked against manufacturer specifications; an estimated filament temperature that was close to the manufacturer-specified color temperature provided confidence that the lamp radiation model's calculated spectral radiation (which was sent to the dryer radiation model as an input) was realistic of the actual drying process. For instance, when the SW lamp was supplied with its rated 1200 W of electrical power, the lamp radiation model calculated an approximate filament temperature of ≈2300 K—close to the SW lamp's design color temperature of 2500 K. Likewise, when simulating FRMW lamp at its rated conditions, the estimated filament temperature was ≈1600 K—similar to the FRMW's advertised color temperature of 1800 K.

The lamp radiation model only produced an approximation of the radiation leaving the bulbs in the actual drying process. Realistically, the lamps exchange radiation with a number of real surfaces (i.e., other bulbs, reflector, glass plate, printed surface, etc.)—all of which have various radiant properties and are at temperatures greater than the ambient temperature. The lamps that are installed in the dryer will reach a hotter temperature for a given supply power because the bulbs are exposed to direct and reflected radiation from other nearby bulbs. This increased lamp temperature will affect the spectrum of radiation being emitted from the bulb. The lamp radiation model does not account for the lamp's increase in temperature, which is why the lamp radiation model only provided a close approximation of the radiation leaving the bulbs.

While the lamp radiation model did not fully account for the radiation exchange experienced by the lamps installed in the dryer, it still provided a practical approximation of the spectral radiation leaving the bulbs. This approximation accounted for the spectral differences in filament size, supplied electrical power, and glass bulb material. The spectral radiation absorbed into the surroundings was then sent to the dryer radiation model to be the boundary condition at the bulb surfaces. The lamp radiation model described above is provided in the online supplement, as directed in Appendix C:.

4.5 STRM and Convection Equations

The first step regarding the STRM was determining the effective view factors between all pairs of surfaces. The general rules for calculating effective view factors was explained in section 3.3, and these rules were applied to the model geometry. A set of effective view factors was required for each wavelength band because the glass plate had semi-gray radiant properties.

One important assumption for calculating the effective view factors was that the bulb surfaces in the dryer radiation model were assumed to be black ($\varepsilon = 1$, $\rho = 0$, $\tau = 0$) and should be treated as opaque surfaces for calculating effective view factors. It is important to note that assuming the bulbs were black surfaces does not affect the radiation exchange because of the bulb's boundary condition, shown in Eq. (100).

$$\dot{q}_{rad,i,\lambda} = \dot{q}_{bulb,\lambda}, \quad for\ i = 1..12, \quad for\ \lambda = 1..8 \tag{100}$$

where $\dot{q}_{bulb,\lambda}$ was determined by the separate lamp radiation model, described in section 4.4. This meant that the spectral radiation leaving the bulb surface was fixed. Changing the bulb emissivity, reflectivity, and transmissivity will not change the radiation leaving the bulbs, and hence it will not affect the radiation exchange to the other surfaces.

In terms of effective view factors, the model geometry was separated into three main groups: dryer-side surfaces, glass plate surfaces, and board-side surfaces. The dryer-side surfaces included the bulbs (1-12), the vertical sides (13-16), and the reflector (17). The glass plate surfaces included both sides of the glass plate (18 and 19). The board-side surfaces included the board surfaces (20-29) and the surroundings surface (30). The effective view factors from the dryer-side surfaces to other dryer-side surfaces were calculated according to Eq. (101).

$$F_{eff,i,j,\lambda} = F_{g,i,j}, \quad for\ i\ and\ j \le 17, \quad for\ \lambda = 1..8 \tag{101}$$

The effective view factors from the dryer-side surfaces to the glass plate were produced from Eq. (102):

$$F_{eff,i,j,\lambda} = F_{g,i,j}\left(1-\tau_j\right), \quad for\ i \le 17, \quad for\ j = 18,19, \quad for\ \lambda = 1..8 \tag{102}$$

Finally, the effective view factors from the dryer-side surfaces to the board-side surfaces were calculated from Eq. (103).

$$F_{eff,i,j,\lambda} = F_{g,i,j}\tau_{18}, \quad for\ i \le 17, \quad for\ j \ge 20, \quad for\ \lambda = 1..8 \tag{103}$$

Similarly, the effective view factors from the board-side of the enclosure were calculated according to Eq. (104) for opaque surfaces to other opaque surfaces on the board-side of the enclosure, Eq. (105) for opaque surfaces to the glass plate, and Eq. (106) for the opaque surfaces on the board-side to other opaque surfaces on the dryer-side of the enclosure.

$$F_{eff,i,j,\lambda} = F_{g,i,j}, \quad for\ i\ and\ j \ge 20, \quad for\ \lambda = 1..8 \tag{104}$$

$$F_{eff,i,j,\lambda} = F_{g,i,j}\left(1-\tau_j\right), \quad for\ i \ge 20, \quad for\ j = 18,19, \quad for\ \lambda = 1..8 \tag{105}$$

$$F_{eff,i,j,\lambda} = F_{g,i,j}\tau_{19}, \quad for\ i \ge 20, \quad for\ j \le 17, \quad for\ \lambda = 1..8 \tag{106}$$

The last effective view factors left to be determined included the effective view factors from the glass plate to the dryer-side and board-side surfaces. The effective view factors from the glass plate to all other surfaces in the enclosure were given by Eq. (107).

$$F_{eff,i,j,\lambda} = F_{g,i,j}, \quad for\ i = 18,19, \quad for\ \lambda = 1..8 \tag{107}$$

With all sets of effective view factors calculated, the semi-gray, STRM equations were input into the model, as shown in Eqs. (108) and (109).

$$\dot{q}_{rad,i,\lambda} = \frac{A_i \varepsilon_{i,\lambda}}{\rho_{i,\lambda}} \left(\left(\varepsilon_{i,\lambda} + \rho_{i,\lambda} \right) E_{b,i,\lambda} - J_{i,\lambda} \right), \quad for\ i = 1..30, \quad for\ \lambda = 1..8 \tag{108}$$

$$\dot{q}_{rad,i,\lambda} = \sum_{j=1}^{30} A_i F_{eff,i,j,\lambda} J_{i,\lambda} - A_j F_{eff,j,i,\lambda} J_{j,\lambda}, \quad for\ i = 1..30, \quad for\ \lambda = 1..8 \tag{109}$$

Equation (108) provided a relation between the net transfer rate, the radiant properties of the surface, and the radiation exchange at the surface, within the specified wavelength band, λ. Equation (109) described the radiosity exchange between each of the surfaces within the specified wavelength band, λ. The total radiation heat transfer rate of each surface, summing the spectral radiation heat transfer rates over all wavelength bands, was given in Eq. (110).

$$\dot{q}_{rad,i} = \sum_{\lambda=1}^{8} \dot{q}_{rad,i,\lambda}, \quad for\ i = 1..30 \tag{110}$$

The spectral blackbody emissive powers, $E_{b,i,\lambda}$ from Eq. (108), were related to the surface temperatures, as shown in Eq. (111).

$$E_{b,i,\lambda} = f_\lambda \sigma T_i^4, \quad for\ i = 13..30 \tag{111}$$

Note that Eq. (111) was not applied to the bulbs. The boundary conditions at the bulb surfaces consisted of specifying the radiation heat transfer rate within each wavelength band, $\dot{q}_{bulb,\lambda}$. This spectral radiation heat transfer included transmitted radiation (from the filament) and emitted radiation (from the bulb surface itself). The specified radiation typically was composed

of 90% transmitted radiation and 10% emitted radiation. In the STRM, Eq. (109) used the bulbs' specified spectral radiation to solve for the surface radiosities, $J_{i,\lambda}$ and $J_{j,\lambda}$. Equation (108) used the bulbs' specified spectral radiation, surface radiant properties, and net radiosity term to determine the blackbody emissive power, $E_{b,i,\lambda}$. However, the blackbody emissive power calculated in Eq. (108) was not representative of the bulb surface temperature, but rather a combination of the bulb and filament temperature since $\dot{q}_{bulb,\lambda}$ was composed of transmitted and emitted radiation. The surface temperature of the bulb could not be coupled to the blackbody emissive power determined by Eq. (108). Instead, the bulb temperature was determined by applying the same convection parameters to the bulb external surface as was used in the lamp radiation model. This de-coupling of the bulb surface temperature from the blackbody emissive power was the reason why the bulbs could be assumed black without disrupting the radiation exchange. The radiant properties did not affect the spectral radiation leaving the bulbs since the spectral radiation was specified by the user.

Convection was included in the analysis by specifying convection coefficients and fluid air temperature at each surface. The convection heat transfer rate at each surface was given by Eqs. (112) and (113).

$$\dot{q}_{conv,i} = \bar{h}_i A_i \left(T_i - T_{amb} \right), \quad for\ i = 1..18 \tag{112}$$

$$\dot{q}_{conv,i} = \bar{h}_i A_i \left(T_i - T_{air,out} \right), \quad for\ i = 19..30 \tag{113}$$

Note that Eq. (112) used an air temperature of T_{amb}, while Eq. (113) used an air temperature of $T_{air,out}$. This difference in applied air temperature was because the forced air was continuously being heated by the dryer's surfaces. By the time the air had been ejected out the dryer jet holes, the air had increased in temperature. $T_{air,out}$ was measured experimentally by mounting several thermocouples along the jet holes and averaging their readings. Thus all the dryer-side surfaces

were exposed to the ambient temperature air, while the board-side surfaces experienced convection to the heated air.

The final step of the model was to perform an energy balance to determine the total heat transfer rate at a surface, accounting for both radiation and convection. This energy balance is shown in Eq. (114).

$$\dot{q}_{tot,i} = \dot{q}_{rad,i} + \dot{q}_{conv,i}, \quad for\ i = 1..30 \tag{114}$$

where $\dot{q}_{tot,i}$ is the total heat transfer rate leaving surface i.

4.6 Dryer Radiation Model Overview

The equations in the section are what made up the dryer radiation model that used the STRM. From the geometry, the areas of the surfaces were calculated. The glass plate and the glass bulb were semi-transparent surfaces with wavelength-dependent transmissivity properties, so a semi-gray analysis was deemed necessary for the model. With the areas calculated, the geometric view factors were determined using the Monte Carlo technique, a view factor library, and the rules governing geometric view factors (reciprocity and enclosure rules). The boundary conditions at the surfaces were presented in Table 11, showing that the radiation leaving the bulb surfaces was modeled by a separate lamp radiation model. The lamp radiation model determined the net spectral radiation leaving the bulbs, both transmitted radiation (from the filament) and emitted radiation (from the bulb surface, itself). The first step in the STRM was to determine the effective view factors between all surfaces. The effective view factors were calculated according to the process outlined in section 3.3. The semi-gray STRM equations (Eqs. (60) through (63)) were applied to the geometry. These equations determined the radiation exchange between the surfaces, but the total heat transfer rate the surfaces was determined by including convection at all surfaces and performing an energy balance on each surface. The EES file of the dryer

radiation model can be found in the online supplement, as outline in Appendix C:. The results of the model are outlined in Ch. 6.

Ch. 5 Experimental Measurements

The research presented would not be complete without experimental information for the surface temperatures and heat flux values during operation of the radiative dryers. While the dryer radiation model from Ch. 4 can simulate the radiation exchange, the model made numerous assumptions and simplifications that could have caused the model results to deviate from the real process. An experiment was designed to measure various process parameters (surface temperatures, surface heat flux rates, etc.) while driving the IR dryers. The experimental measurements provided a comparison to the model that will help with validation or correction.

5.1 Experimental Concept

The main goal of the experimental measurements was to determine the total heat flux (radiation and convection) received by the corrugated board from the IR dryer during its normal operation. To perform the experiment, a test apparatus was designed to replicate the radiation exchange that occurs on the actual printing press. Important features required for the test apparatus included the dryer cassettes, a test surface that simulates the printed surface, a heat flux sensor (that can accurately account for intense radiation), ductwork for the forced cooling air, among other sensors to track various process parameters. Figure 43 illustrates an overview of the test apparatus's main components for the experiment.

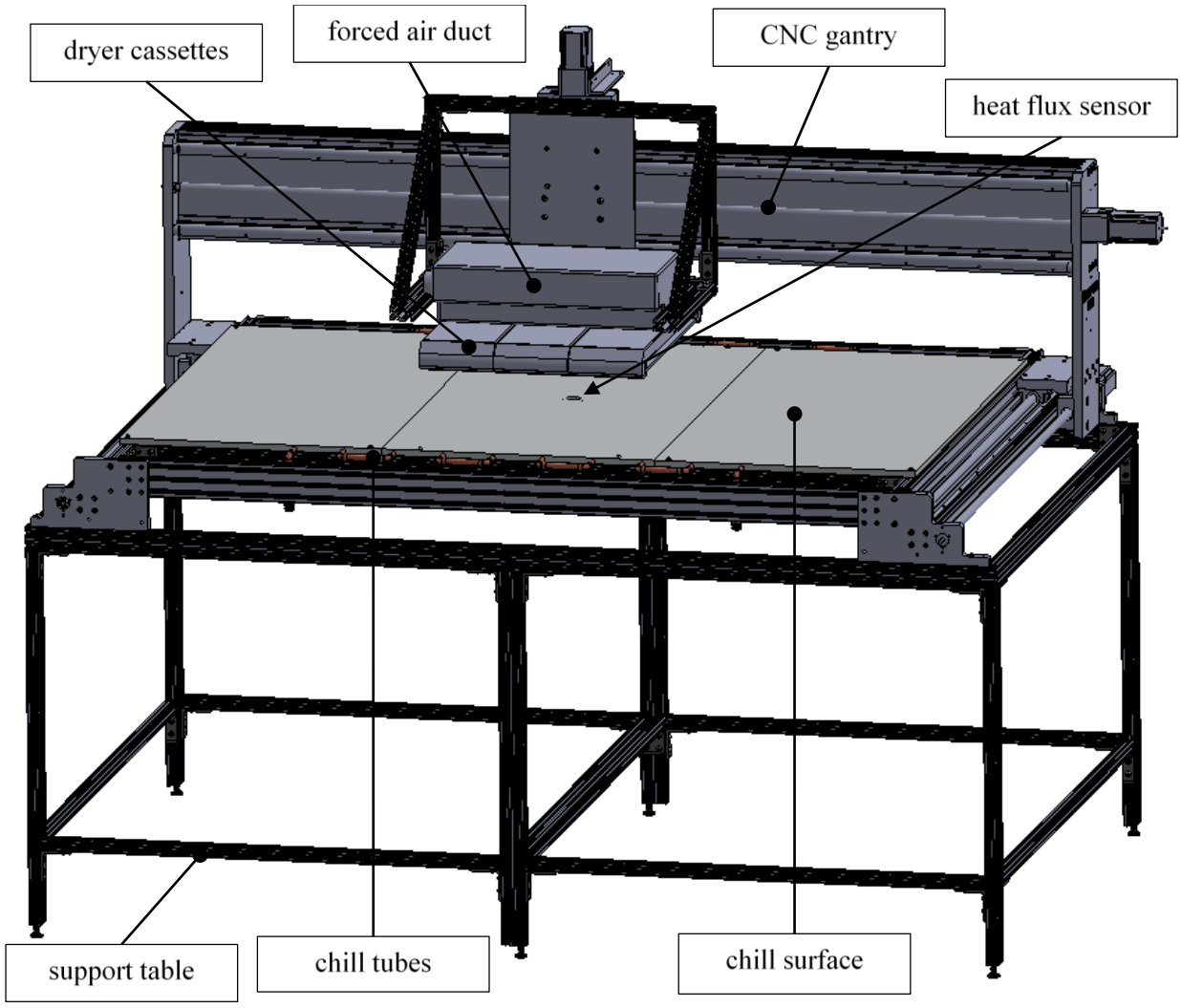

Figure 43: Test apparatus.

The test apparatus had three dryer cassettes in order to mimic the condition experienced by the approximately 18 cassettes that are mounted on an actual printing press. Unfortunately, creating a test apparatus with 18 cassettes was impractical for space and power consumption reasons. Conversely, performing experiments with just one cassette was not sufficient because the measurements would not be representative of the true radiation exchange on the press where most cassettes are surrounded on both sides by other cassettes. For this reason, three cassettes were included in the apparatus.

The test apparatus also included a flat, aluminum surface that had a single heat flux sensor mounted in the surface's center. The entire surface was powder-coated a matte black (ε = 0.95) to be as absorptive as possible to incident radiation. The surface was included in the test apparatus to create a similar environment as on the printing press. For instance, in reality, the dryer's forced air is pushed through the cassettes and onto the printed surface, where convection happens. The aluminum surface was present on the apparatus to create the same convection coefficient that the corrugated board would experience on a printing press. Similarly, just as the corrugated board would reflect some of the dryer's radiation, the aluminum surface also provided a surface for some irradiation reflection (not much, since it was matte black). The test's surface shown in Figure 43 was separated into three separate surfaces for ease of manufacturing and handling.

The sensor in the surface (shown in Figure 43 as the small circle in the surface's center) was a thermo gage heat flux sensor specifically designed for high radiation environments. The sensor was only one inch in diameter, so it only measured the heat flux at the specific location where the sensor was mounted on the surface. As explained in section 4.5, the dryers produced a spatially-varying heat flux: the parts of the test surface near the cassette edges experience less radiation than the part of the surface that is directly under the center of the dryer cassettes. For this reason, the three cassettes were mounted on a movable CNC-gantry that could be traversed across all three Cartesian directions (x, y, and z). By mounting the cassettes on a 3-axis CNC structure, the apparatus was able set the dryers to various clearance heights (i.e., the distance between the dryer cassettes and the aluminum surface) in the z-direction, and then move the dryers in the xy-plane to incrementally record a 2-D "map" of the heat flux on the aluminum surface.

When operating on the printing press, freshly printed substrates get continuously cycled through and exposed to the dryers; every substrate enters at the same cold temperature. The experiment, on the other hand, had the dryers heating the same aluminum surface for an extended period of time. Therefore, the aluminum surface had to be actively cooled to keep it from overheating and to keep the surface temperature low enough that the radiation exchange was representative of the actual drying process on the printing press. The aluminum surface was cooled by copper chill tubes that were press-fit into the grooves in the back of the aluminum surface. An air-cooled chiller cooled the water to a set temperature and cycled the water through the chill tubes. Since the chill tubes were simply press-fit into the aluminum surface, any small air gap at the interface of the tubes and the surface could create a large contact resistance, which would significantly inhibit the cooling ability of the chill tubes. A thermally-conductive paste was applied at the interface of the chill tubes and the grooves to minimize the contact resistance. The underside of the CNC table is shown in Figure 44 with the serpentine copper chill tube.

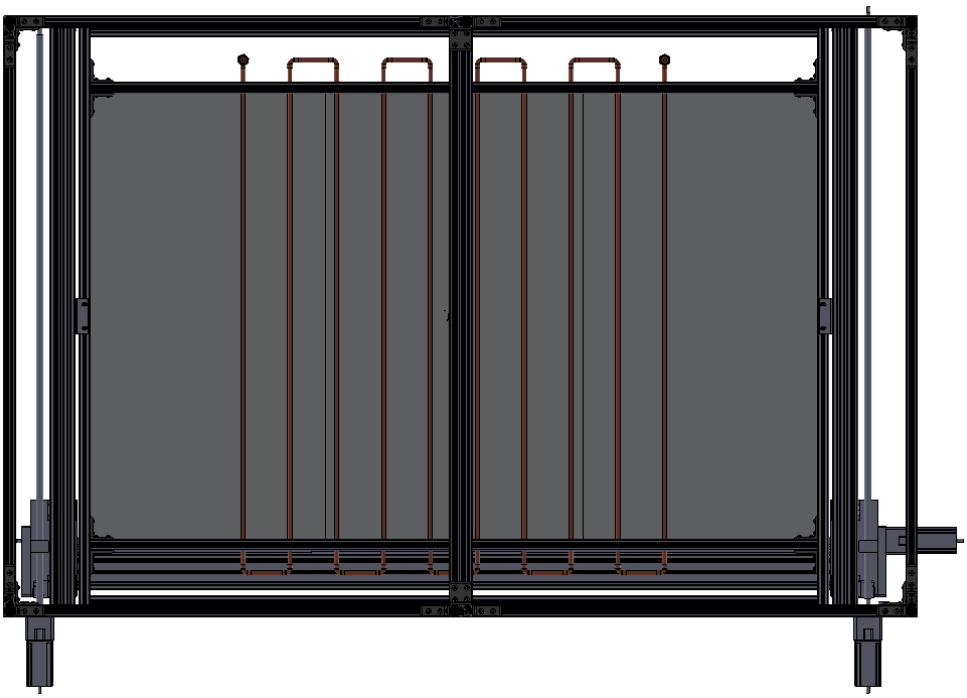

Figure 44: Underside of test apparatus.

A photo of the CNC table with the chill surface mounted is shown in Figure 45. Note that the picture was taken before the chill surface was powder-coated a matte black, and only cassette was installed at the time.

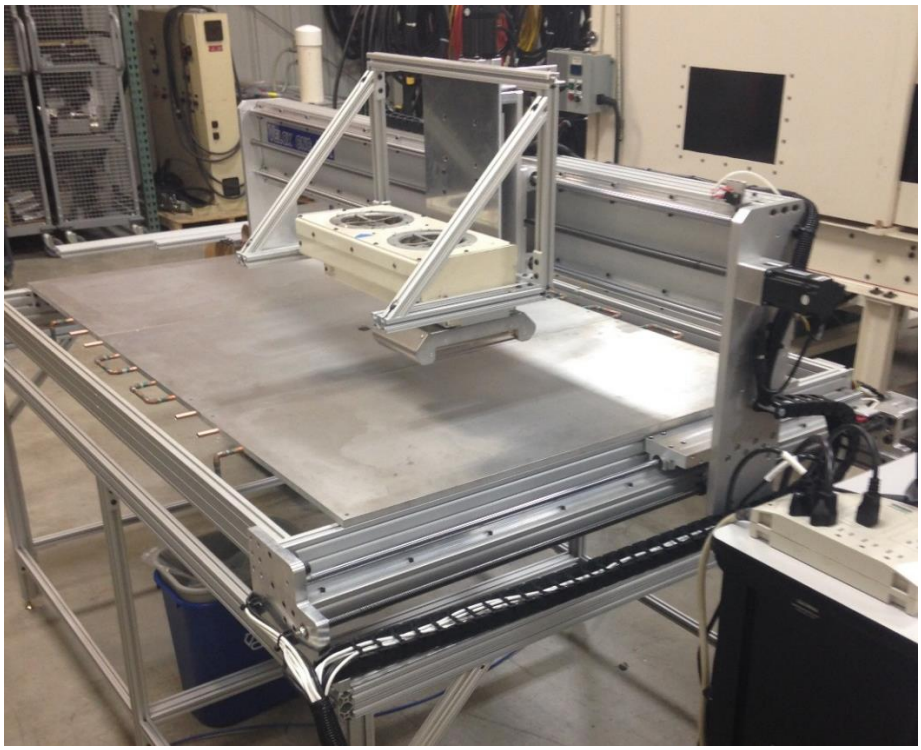

Figure 45: CNC table with chill surface mounted.

In addition to the equipment shown in Figure 43, the test apparatus had other auxiliary components, like the supply air fan and ductwork, the chiller for chilled water, the CNC software and controller, the data acquisition system (DAQ), and all measurement sensors. Other than the surface heat flux, the other important parameters to measure included surface temperature, supplied lamp power, reflector temperature, forced air temperature and flow rate, cooling water temperature and flow rate, and ambient conditions.

The experimental results were to be compared with the results from the model to validate or refute the model's accuracy. This was done by inputting the recorded surface temperatures (and other measurements like supplied power, reflector temperature, etc.) into the dryer radiation

model and running the model. By comparing the dryer radiation model's calculated results with the experimentally-measured heat flux, it was possible to gain confidence in some aspects of the model and correct it based on any discrepancies that were observed.

5.2 Experiment Equipment

The equipment required for the experiment is listed in Table 12.

Table 12: Equipment used in the experimental measurements.

Equipment	Vendor	Purpose
Support Table*	80/20	• Raise CNC equipment off floor • Provide mounting for other equipment
Triple Dryer Cassette*	XDS Holdings	• Provide radiative heat flux
Triple Dryer Duct*	XDS Holdings	• Provides housing for dryer's supply air fan and mounting for dryer cassettes
CNC Table and Motors*	Velox CNC	• 3-axis CNC table to move the dryers into the desired position
CNC Software	Mach3	• Allows G-code programs to control the CNC table head
Control Box	Velox CNC	• Interprets the Mach3 commands and controls the CNC table's motors accordingly
Duct Mount*	80/20	• Hardware to mount the duct to the CNC gantry
Supply Air Fan	N/A	• Supplies a constant stream of air to the duct, for the dryer fan to pull through the cassette
Supply Air Ductwork*	N/A	• Routes the air flow from the supply fan to the dryer cassette
MASS-tron II Air Flow Sensor	Air Monitor Corporation	• Measures the flow rate, pressure, and temperature of the supplied air
Heat Flux Sensor	Vatell	• TG1000-0 • Water-cooled thermo gage sensor made for high radiation environments • ± 3% uncertainty
Chill Surface*	N/A	• Provides mounting for heat flux sensor • Cooled using copper chill tubes

Chiller*	Sterlco	• Air-cooled water chiller to cool the water that flows through the chill surface
Chill Water Flow Meter	OMEGA	• FLR flow sensor • Measures the water flow rate fed in the chiller/chill surface loop
DAQ System*	Atlantic Integration	• Displays and records the sensor measurements
Electrical Power Cart	N/A	• Controls the amount of relative power delivered to the dryer cassettes through a digital potentiometer.
Electrical Power Meter	Dent	• Powerscout PS3037-E-D • Measures the total power supplied to the lamps of the three cassettes
Ambient Conditions Sensor	OMEGA	• BTHX iBTX series • Measures the ambient conditions—temperature, pressure, and relative humidity

Thermocouples	OMEGA	• All are Type K
		• Used in the following locations
		  ○ Three embedded in the chill surface
		  ○ Inlet and outlet of chill surface
		  ○ One at each end of the forced air jet holes
		  ○ One attached to the cassette reflector
		  ○ One in the supply air ductwork

*Photos depicting these pieces of equipment can be found in Appendix A:.

5.3 Chill Surface Design

The chill surface was a piece of equipment that needed to be designed correctly to ensure that the heat flux measurements from the test were representative of the drying process on the printing press. Specifically, the temperature of the aluminum surface needed to remain low enough that it did not affect the radiation exchange with the dryer. A 1-D finite-difference model was created in EES to estimate the temperature distribution in the aluminum surface with the chill tubes present. The model was based upon the situation shown in Figure 46.

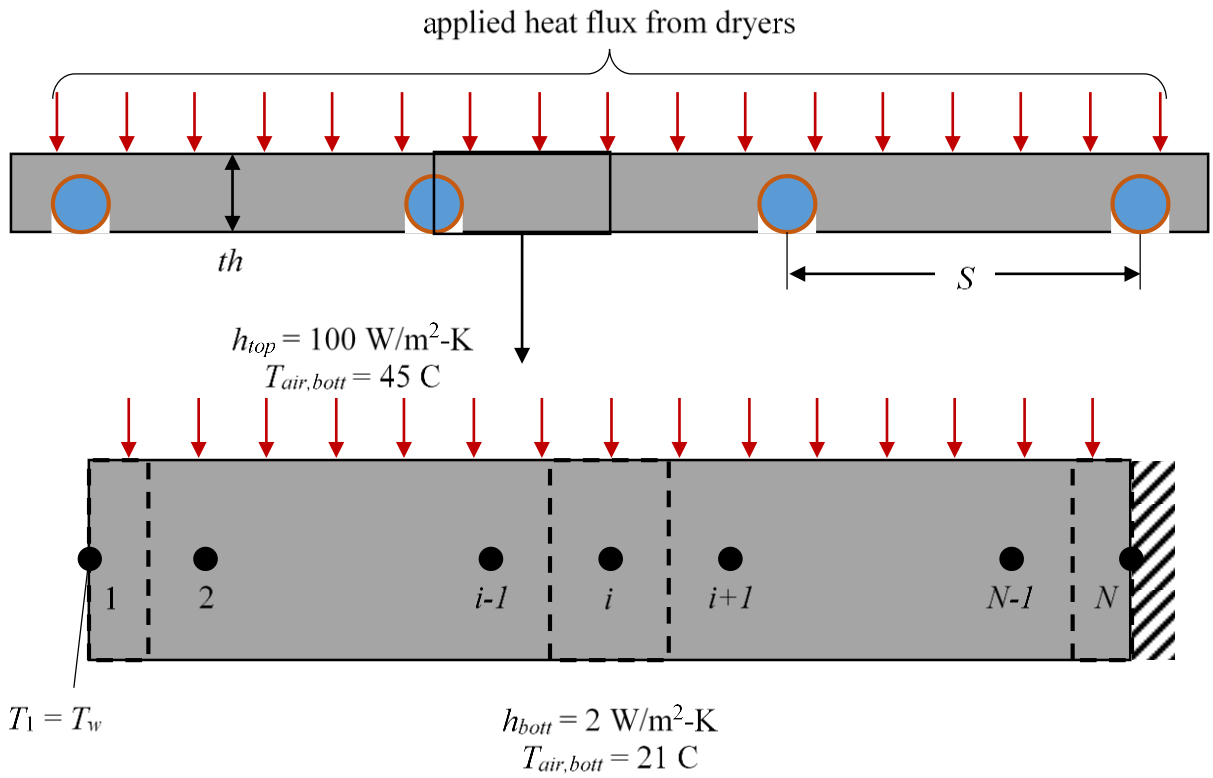

Figure 46: Section view of the chill surface illustration.

The aluminum surface had a constant thickness, *th*, and had the chill tubes embedded into the back of the surface with spacing, *S*. Aluminum has a very high conductivity (~230 W/m-K), so the surface's temperature gradients across the surface thickness were ignored. This assumption makes the analysis 1-D. The copper chill tubes have a high conductivity, and thus the temperature of the tube was assumed to be at the water temperature. The contact resistance between the copper tube and the chill surface was likely small enough that the temperature drop due to the contact resistance was small in comparison to the temperature drop along the chill surface, thus the contact resistance was assumed negligible. The repetition and symmetry of the tubes suggested that only half the spacing distance needed to be simulated. The finite difference analysis discretized the space into *N* nodes, with node 1 located at the center of the chill tube, and node *N* positioned *S*/2 away from node 1. The distribution of the nodes followed Eq. (115) and the spacing between the nodes was calculated according to Eq. (116):

$$x_i = \frac{S}{2}\left(\frac{i-1}{N-1}\right), \quad for\ i = 1..N \tag{115}$$

$$dx = \frac{\frac{S}{2}}{N-1} \tag{116}$$

Each internal node's control volume had an *x*-width of *dx*, a width into the page of *b* (*b* = 1 m since the analysis was 1-D), and a *y*-height of *th*. Each internal node experienced conduction on both sides, convection on the top and bottom, and the applied radiation at the surface top. The analysis was steady-state, so there was no energy storage in any of the control volumes. Assuming that convection and conduction were outgoing at each node, the energy balance for each internal node was given by Eq. (117):

$$\dot{q}_{rad,internal} = \dot{q}_{conv,top,i} + \dot{q}_{conv,bott,i} + \dot{q}_{cond,left,i} + \dot{q}_{cond,right,i}, \quad for\ i = 2..N-1 \tag{117}$$

where each of the terms in Eq. (117) was calculated according Eqs. (118) through (122).

$$\dot{q}_{rad,internal} = \dot{q}''_{surf}\, bdx \tag{118}$$

$$\dot{q}_{conv,top,i} = h_{top}\, bdx\left(T_i - T_{air,top}\right) \tag{119}$$

$$\dot{q}_{conv,bott,i} = h_{bott}\, bdx\left(T_i - T_{air,bott}\right) \tag{120}$$

$$\dot{q}_{cond,left,i} = \frac{kbth}{dx}\left(T_i - T_{i-1}\right) \tag{121}$$

$$\dot{q}_{cond,right,i} = \frac{kbth}{dx}\left(T_i - T_{i+1}\right) \tag{122}$$

$\dot{q}''_{surf}$ is the radiant heat flux from the dryers that was incident on the surface and *k* is the thermal conductivity of the aluminum surface. The *h* and T_{air} variables are the average convection coefficient and temperatures of the air, as indicated in Figure 46. T_i represents the temperature of the aluminum surface at each node.

The boundary condition at node 1 fixed its temperature to be equal to the cooling water temperature, T_w.

$$T_1 = T_w \tag{123}$$

Node *N* was located at a line of symmetry for the temperature distribution, thus its boundary condition was an adiabatic boundary. The energy balance for this boundary condition is shown in Eq. (124).

$$\dot{q}_{rad,end} = \dot{q}_{conv,top,N} + \dot{q}_{conv,bott,N} + \dot{q}_{cond,left,N} \tag{124}$$

where each of the terms was calculated according to Eqs. (125) through (128).

$$\dot{q}_{rad,end} = \dot{q}''_{surf}\, b\frac{dx}{2} \tag{125}$$

$$\dot{q}_{conv,top,N} = h_{top}\, b\frac{dx}{2}\left(T_N - T_{air,top}\right) \tag{126}$$

$$\dot{q}_{conv,bott,N} = h_{bott}\, b\frac{dx}{2}\left(T_N - T_{air,bott}\right) \tag{127}$$

$$\dot{q}_{cond,left,N} = \frac{kbth}{dx}\left(T_N - T_{N-1}\right) \tag{128}$$

Note that the only difference between the equations for node *N* and the internal nodes was the control volume thickness—the control volume of node *N* was half the width of the internal nodes' control volumes.

The hottest temperature in the temperature distribution was always at node N, thus the Eq. (129) held true.

$$T_{max} = T_N \tag{129}$$

The surface's applied radiation heat flux was not known, but an upper bound could be computed. The three lamps being investigated (SW, FRMW, MW) have rated powers of 1200 W, 950 W,

and 480 W, respectively. If the dryers had SW lamps installed, each lamp would dissipate at most 1200 W of power. Each cassette has the dimensions of L_{cass} = 7.44 in and W_{cass} = 5.94 in, and holds four lamps. If the lamps converted all 4800 W of electrical power into radiation incident on the surface, and that radiation was distributed equally over the entire cassette area ($A_{cass} = L_{cass}W_{cass}$), then the applied radiation heat flux would be ≈168 kW/m^2. This serves an upper bound estimate, as some of the radiation emitted from the filament would be absorbed in the lamp bulb and glass plate and some of the radiation would be lost to the surrounding environment. Furthermore, it would be unlikely that the lamps were operated at the maximum rated power level and convert all of that power to usable radiation. To account for this uncertainty, several different radiation heat fluxes (all at or below 168 kW/m^2) were simulated with the chill surface temperature distribution model. To start calculations, the bulbs were assumed to each emit 700 W of radiation, and 75% of the emitted radiation was absorbed in the chill surface. This assumption resulted in a surface radiation heat flux of 73.6 kW/m^2.

The two design parameters for the chill surface were the thickness of the surface and the spacing of the chill tubes. The surface thickness could range anywhere between 0.25 inches to 1 inch thick. A thick chill surface would have a smaller maximum temperature than a thin chill surface. Unfortunately, a thick chill surface would require a longer time to reach steady-state than a thin chill surface because of its larger thermal capacitance. The chill tube spacing could range between 2 inches and 8 inches. A small spacing value would produce a lower maximum temperature than a large spacing, but would also require more materials and cooling power. Using the suggested 73.65 kW/m^2 as the radiation heat flux, the temperature distribution model was run according the thickness and spacing ranges to produce the contour plot shown in Figure 47.

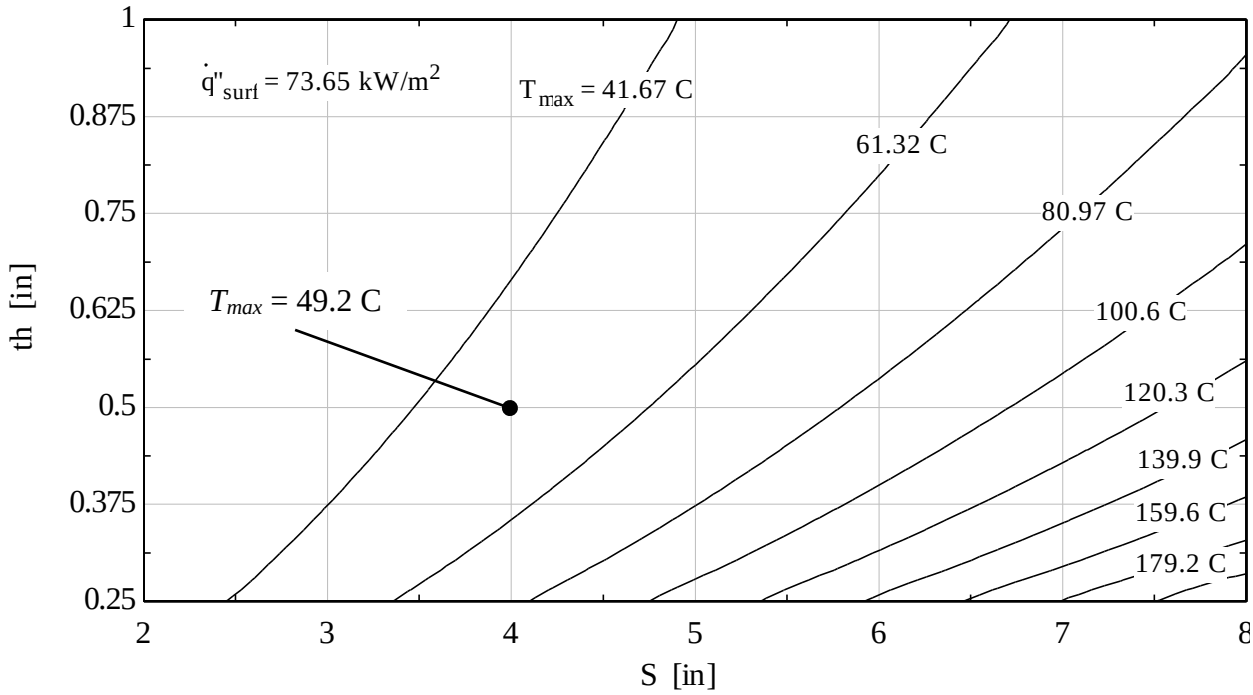

Figure 47: Contour plot of the chill surface's max temperature.

As expected, the maximum temperature increased with decreasing surface thickness and increasing chill tube spacing. The point at S = 4 in and th = 0.5 in corresponded to a maximum temperature of 49.2 °C, which was acceptable. A half inch thick aluminum surface was convenient for manufacturing and easy to handle, making it ideal for the surface. Additionally, it also provided reasonably fast response characteristics to shorten testing time. Four inches of space between chill tubes allowed ample room to fit the heat flux and temperature sensors in the surface and required few materials. Assuming th = 0.5 in and S = 4 in, multiple different radiation heat flux values were run in the program, and plotted in Figure 48.

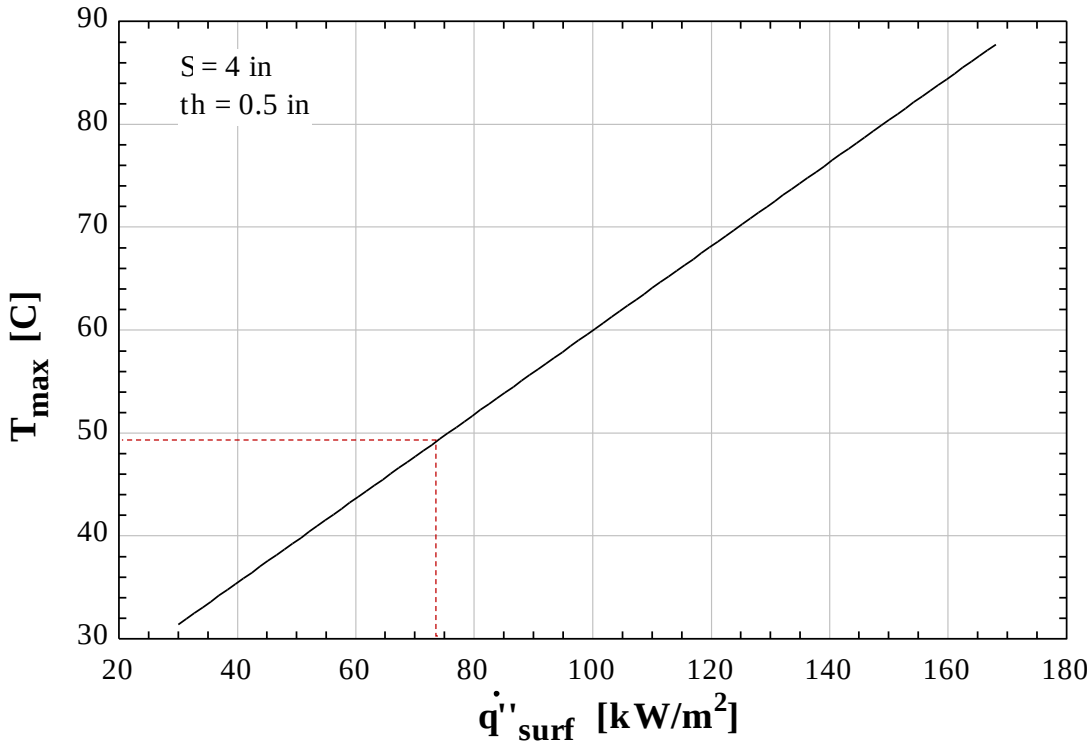

Figure 48: Max temperature vs. incident radiation—the red dashed lines indicate a heat flux of 73.65 kW/m^2.

Even if the applied heat flux extended up to 120 kW/m^2, the table's maximum temperature was expected to only reach 68 °C. In general, radiation heat flux is proportional to the difference of the surface temperatures to the 4th power:

$$\dot{q}_{rad} \propto \left(T_{hot}{}^4 - T_{cold}{}^4\right) \tag{130}$$

When the difference between T_{hot} and T_{cold} is very large, large fluctuations of T_{cold} hardly affect $\dot{q}_{rad}$ because $T_{hot}{}^4$ is always orders of magnitude greater than $T_{cold}{}^4$. The 19 °C change in maximum temperature from 49 °C to 68 °C is relatively small when considering that the filament is upwards of 1600 °C. The 19 °C change would significantly affect convection, but convection only slightly contributes to the heat transfer process (shown in section 2.4). The 19 °C change in the maximum surface temperature would not affect the heat flux recorded by the sensor. A chill surface with a thickness of 0.5 in and spacing of 4 in was chosen for the testing.

The heat flux sensor and three thermocouples were embedded into the center of the chill surface. The thermocouples were equally spaced around the outside of the heat flux sensor; the surface temperature was computed to be the average of the three measurements. Figure 49 provides a section view of the chill surface at the sensors' location.

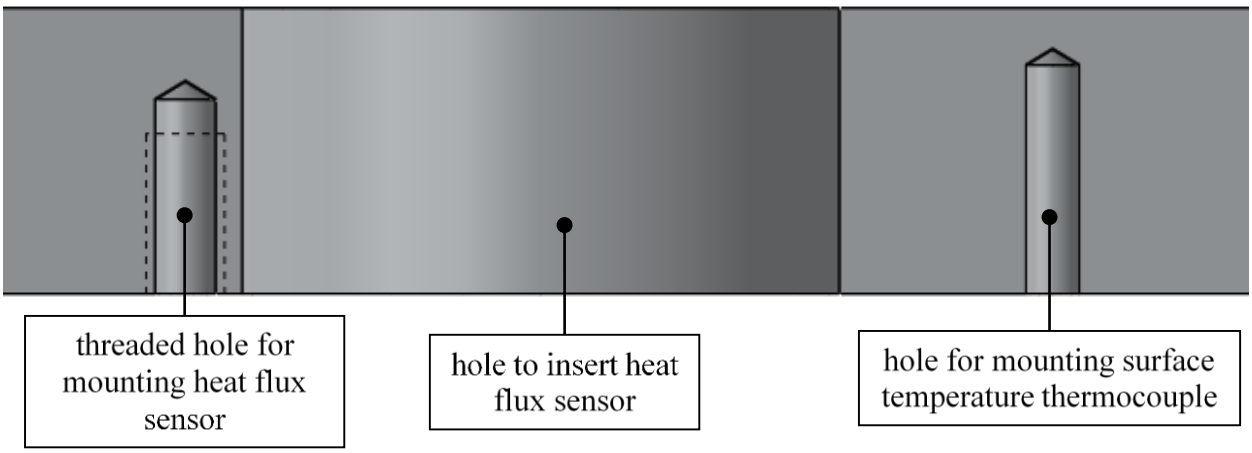

Figure 49: Section view of chill surface at the heat flux sensor and thermocouples.

The surface temperature thermocouples were cemented into the mounting holes in the aluminum surface. The heat flux sensor itself was actively water-cooled, and did not have a strong thermal connection with the chill surface. Thus, the surface temperature thermocouples did not provide an exact measurement of the heat flux sensor's surface temperature (where the heat flux was measured). The thermocouples could not be attached to the heat flux sensor due to the electrical interference in the sensors' signals. While this was not ideal, the surface thermocouples still provided a reasonable estimate of the surface temperature where the heat flux was measured. This estimate of surface temperature was sufficient when comparing the experimental results with the model results since the measured heat flux was predominantly radiation from the filament (which was at a temperature much higher than the sensor temperature). Because this temperature difference was so large, large uncertainties in the sensor temperature still resulted in small errors in the calculated heat flux.

5.4 Experimental Procedure

The experimental procedure for recording a 2-D map of heat flux measurements involved moving the dryers to specified positions and recording the heat flux and other readings. In addition to the sensors' measurements, the DAQ needed to keep track of the (x,y) coordinates of each measurement point. In data post processing, all the heat flux measurements that were taken at a given (x,y) location were averaged, such that there was one average heat flux value at each measurement point. The average heat flux readings were rearranged according to their (x,y) location to create a surface plot that served as a 2-D map, showing how the heat flux varied with respect to position under the dryers. Even though the heat flux was the measurement of most interest in the experiment, the mapping post process could be applied to any logged variable (surface temperature, supplied electrical power, air flow rate, etc.) to indicate how those variables changed at different positions.

The measurement points were laid out as a M x N rectangular grid (M rows and N columns) with the grid center being the location of the heat flux sensor. Figure 50 below illustrates the distribution of the points and defines the point coordinate system.

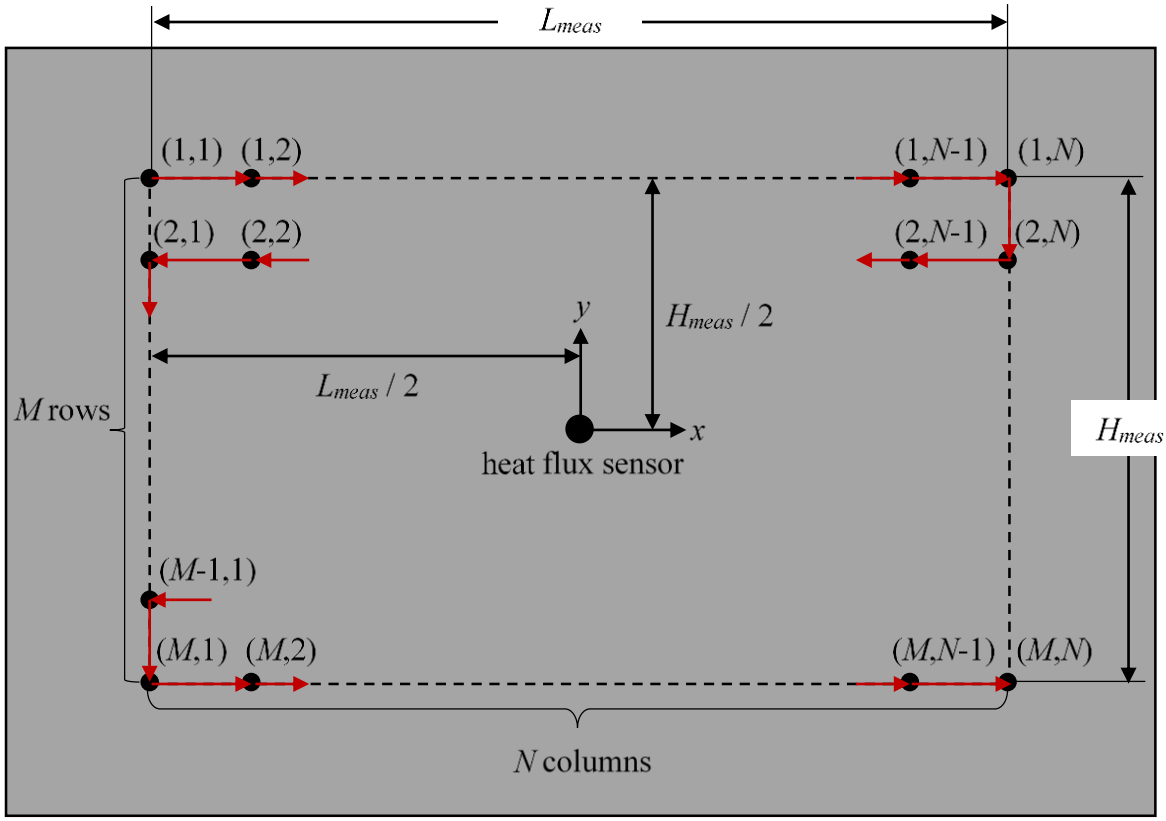

Figure 50: Top view of the measurement grid.

Table 13 explains the objects and variables shown in Figure 50.

Table 13: Measurement grid parameters.

Object	Representation
Large gray rectangle	• Portion of chill surface
Dashed rectangle	• Encompassing measurement area • Dimensions: L_{meas} x H_{meas} (both defined by user)
Center black dot	• Heat flux sensor • Origin of test coordinate system • Located at the center of the measurement area
Small black dots	• Positions where dryer cassettes will stop for the DAQ to log measurements • *M* rows, *N* columns (both defined by user) • *M* and *N* must be odd integers to ensure that a measurement point is aligned with the heat flux sensor
Ordered pairs	• Describe the index of the measurement point • (row #, column #)

Red arrows	• Indicate the serpentine path of the dryers from point-to-point

The coordinate system was situated so that the origin was directly aligned with the heat flux sensor. For example, the top-left point (1,1) was at an (*x*,*y*) location of $\left(-\frac{L_{meas}}{2},\frac{H_{meas}}{2}\right)$; likewise, the bottom-right point (*M*,*N*) was located at $\left(\frac{L_{meas}}{2},-\frac{H_{meas}}{2}\right)$. Because the dryers were the components moving to the different measurement point, each measurement position in Figure 50 indicates where the center of the dryer cassettes was located while the DAQ recorded measurements. Figure 51 illustrates the outline of the dryers at 5 different measurement positions—the dryer outline is not to scale.

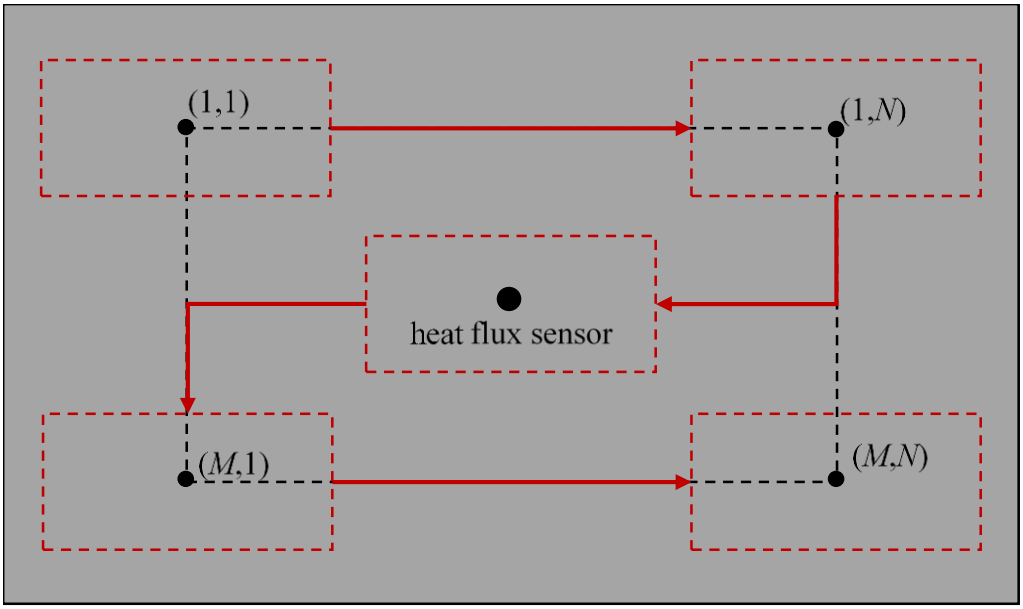

Figure 51: Dryer outline at various measurement positions.

In order for a measurement position to be located at the heat flux sensor, the number of rows and columns, (*M* and *N*, respectively) had to be odd integers. Furthermore, the test procedure followed the listed guidelines:

- The first measurement recorded was always at the top-left corner of the measurement area, point (1,1).
- After finishing logging data at (1,1), the dryers incremented their position one point to the right to (1,2). This pattern repeated for all points in the first row until point (1,*N*).
- When the dryers finished logging data at top-right point, (1,*N*), the dryers incremented rows, moving down to point (2,*N*).
- When in the second row, the dryers incremented positions to the left until the DAQ finished recording data at point (2,1).
- The above three steps were repeated for the remaining rows until the DAQ collected data associated with each measurement point.

Because there were always an odd number of rows in the measurement grid, the dryers always finished testing at the bottom-right measurement point, (*M*,*N*). The serpentine path was desired to reduce the dryer travel time and to reduce the time required for the heat flux sensor to reach a steady-state value.

The dryer path was implemented by the CNC machine through the use of a G-code program. G-code is a programming language implemented by manufacturing machinery to control positioning and movement of equipment. A G-code program consists of instructions that dictate the actions of the controlled equipment. A CNC software (the experiment uses Mach3) interprets and commands servomotors to perform the G-code actions one line at a time. Two simple commands include traverse and dwell. Traverse moves the controlled equipment to a specified point at a specified speed. Dwell holds the controlled equipment's current position for a specified period of time. Additionally, if a certain action is repeated many times throughout a

single program, G-code has a sub-program function that allows the code of the repeated action to be written once, and then called/looped by the main program.

G-code was perfect for the experiment, as the measurement points were programmed into the code according to their sequence in the experiment. Dwell times were input at each measurement point to allow the heat flux sensor to reach steady-state. While the DAQ could continuously log measurements, the created file would have been exceedingly large. To keep the file size reasonable, the DAQ needed to communicate with the G-code so that the DAQ could be told when to start and stop logging data at a measurement point. The experiment's CNC table was originally meant for a 3-axis CNC router, thus Mach3 had the ability to control both the (x,y,z) position as well as the router spindle power and speed. Since the experiment did not use a router with a spindle, the CNC spindle functions was utilized for communication with the DAQ. When the spindle was activated by the G-code, the control box output a 110VAC signal. Instead of using this signal to power the spindle, the experiment used the signal to drive a relay that connected to the DAQ. After some internal programming within the DAQ, the G-code's spindle ON/OFF command triggered the DAQ's measurement logging. The G-code for the experiment is attached in the electronic supplement, as outlined in Appendix C:.

As mentioned previously in this section, the (x,y) position of the dryers needed to be recorded at each measurement point in order to create a 2-D map of the heat flux. There were no external sensors that measure the dryer's absolute (x,y) position and it remains unknown if it is possible to send Mach3's displayed (x,y) position to the DAQ for it to store. The only option left was to determine the dryer position based upon the G-code. For a given set of M, N, L_{meas}, and H_{meas}, the (x,y) locations of the measurement points and their sequential order of logging could be determined. A program was created that listed the measurement points' (x,y) locations

in their chronological order in a spreadsheet file. The DAQ accessed this file to read the various measurement point locations and then associated any logged measurements with the respective (x,y) location. To correctly pair the (x,y) locations with the logged measurements, the DAQ used the falling edge of the spindle signal to know when to increment to the next (x,y) location. Every time the G-code signaled to the DAQ to stop logging measurements, the DAQ referenced the next listed (x,y) location so that when the DAQ started logging measurements again, it associated the readings with the correct measurement point.

5.5 Preliminary Experimental Results

Before finalizing the test parameters, a preliminary run of the experiment was performed to allow for any adjustments in the parameters. The preliminary test run used the parameters shown in Table 14.

Table 14: Preliminary testing parameters.

Parameter	Description	Numerical Value
M	Number of rows in measurement grid	11
N	Number of columns in measurement grid	11
L_{meas}	Length of measurement grid	18 in
H_{meas}	Height of measurement grid	12 in
H_{clear}	Clearance height between surface and cassettes	2 in
$\dot{m}_{air}$	Mass flow rate of supply air	250 scfm
T_w	Setpoint of the cooling water chiller	16 C
Lamp Type	Type of lamp	SW
Glass Type	Type of glass plate	Ceramic
$\dot{q}_{supply}$	Electrical power supplied to three cassettes	8800 W
t_{ss}	Time spent waiting at each point allowing the heat flux to reach steady-state value	10 sec
t_{meas}	Time required for the DAQ to log measurements	20 sec
SR	Sampling rate of the DAQ	20 S/sec

The measurement grid used provided a 1.8 in space between points in the *x*-direction, and a 1.2 in space between points in the *y*-direction. Additionally, considering travel time, waiting time, and logging time, the entire test needed 1 hour 18 minutes of time. A photo of the apparatus in operation is shown in Figure 52.

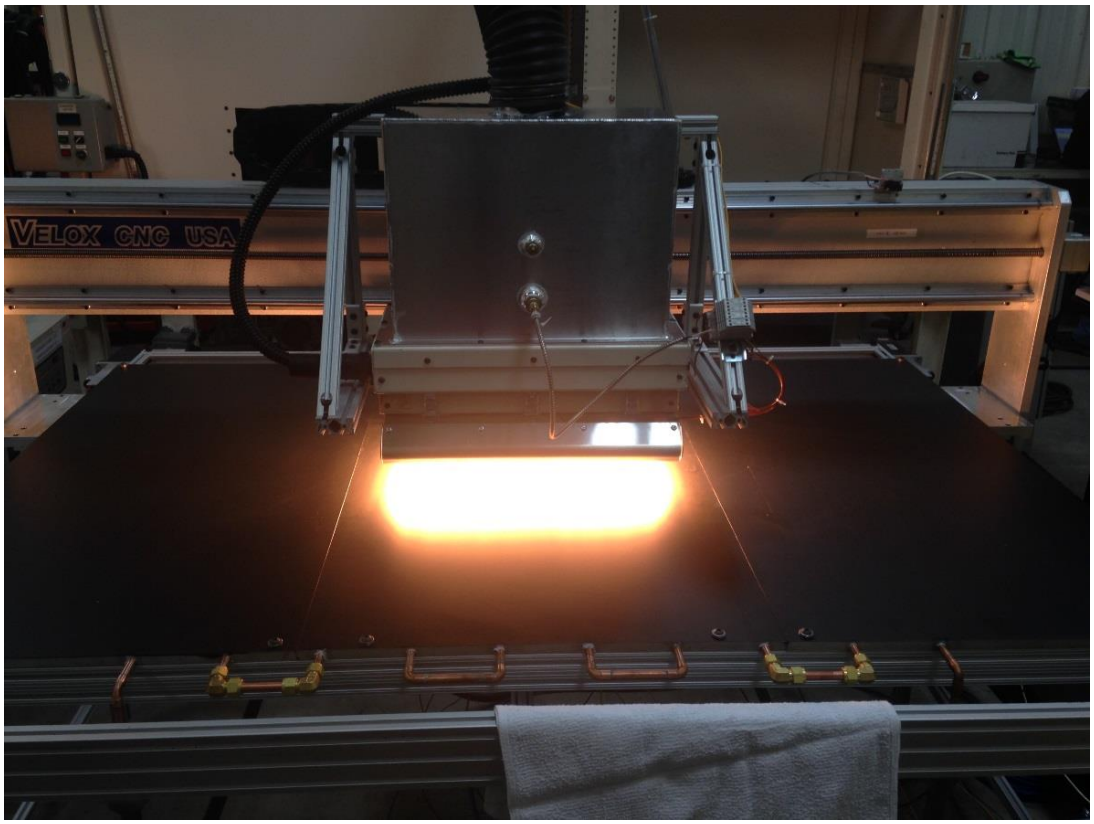

Figure 52: Dryers in operation during testing.

This initial test generated the heat flux and surface temperature map shown in Figure 53.

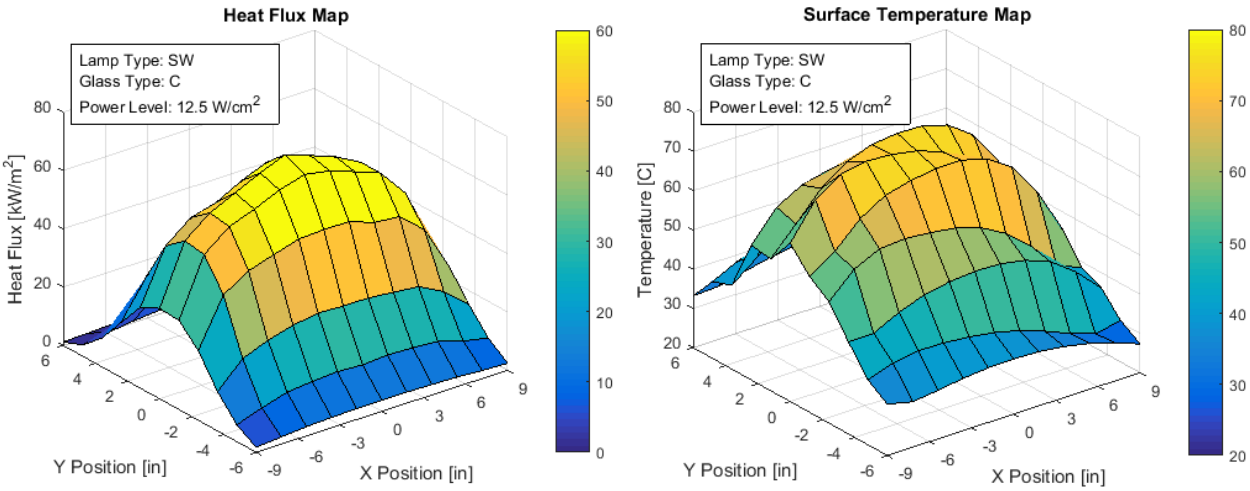

Figure 53: Heat flux and surface temperature maps from preliminary testing.

The shape of the heat flux map looks reasonable—the heat flux was a maximum (69.7 kW/m^2) near the center of the dryers and drastically dropped toward the edges of the map. The surface temperature map was not as symmetric as the heat flux map—the shape of surface temperature surface depended on the row of the measurement grid. The odd rows (where the dryers were moving left-to-right) had a temperature distribution that was hotter on the right side than the left. Likewise, the even rows (where the dryers were moving right-to-left) showed hotter temperatures on the left. This was because the surface temperature reading did not reach steady-state in the prescribed t_{ss} = 10 seconds that the dryers dwelled at a position before the DAQ began logging. The fact that the chill surface temperature did not reached steady-state does not greatly affect the validity of the experiment results because the heat flux at the surface was radiation dominated. Even a large difference in the steady-state surface temperature and the recorded surface temperature would still result in a negligible difference in the model's calculated board heat flux because the radiation was emitted from a significantly higher temperature than the surface temperature.

The goal of the experiment was to simulate the actual radiation exchange on a printing press that has approximately 18 cassettes mounted side-by-side. Thus, the heat flux

measurements under the two outside cassettes were disregarded since their values were not representative of the radiation exchange on a printing press; only the measurements aligned with the center cassette were useful. The linearly-interpolated heat flux map under the center cassette is shown in Figure 54.

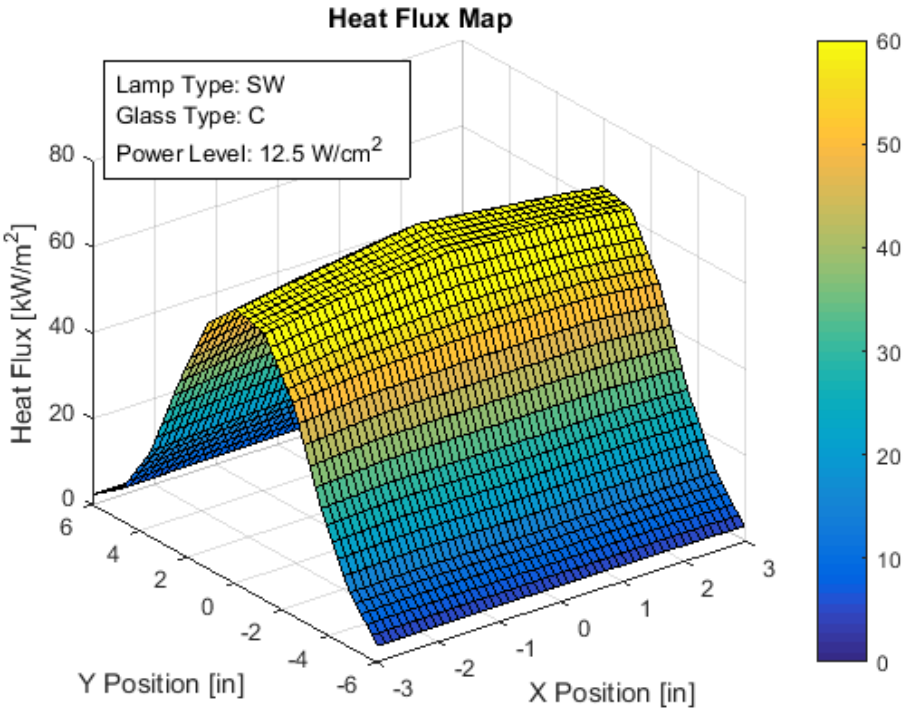

Figure 54: Heat flux map under the center cassette.

The heat flux map displayed in Figure 54 was considered approximately 1-D, since the heat flux hardly changed with respect to the *x*-direction. The heat fluxes were averaged across the *x*-direction to create a 1-D heat flux distribution, shown in Figure 55 with the error bars representing the heat flux sensor's ± 3% uncertainty error.

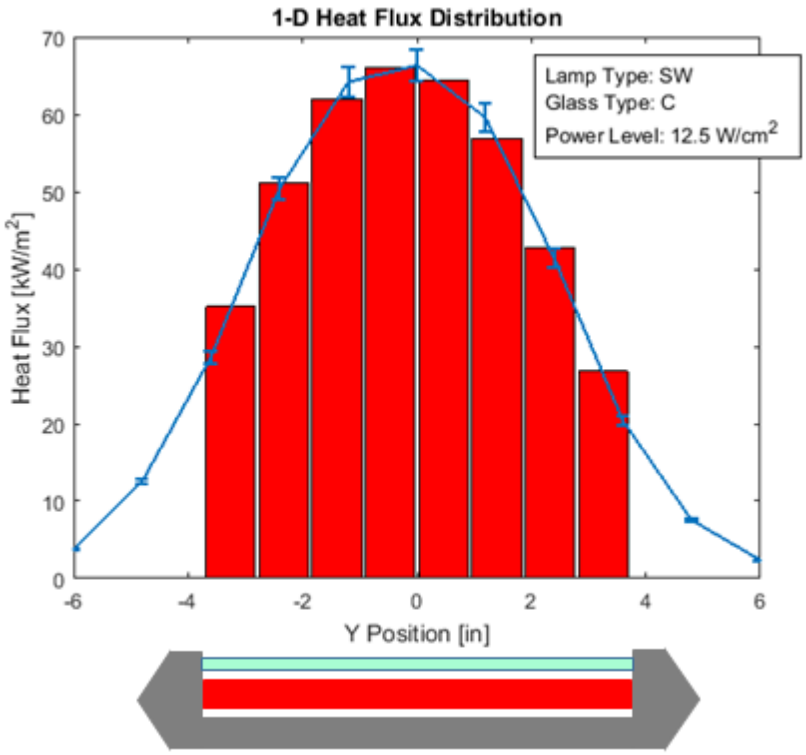

Figure 55: 1-D heat flux distribution under the dryer.

The area directly under the center cassette was broken into eight strips—the same process done for the dryer radiation model in Ch. 4). The red bars in Figure 55 demonstrate the average heat flux measured within these surfaces. The values of these red bars will serve as the comparison between the experimental and model heat flux values.

In Figure 55, the heat flux distribution (both the blue line and red bars) should have been symmetric about $y = 0$ in. The heat flux distribution was slightly shifted towards the negative y-values. This was due to improper CNC setup, and was corrected after the preliminary test run by offsetting the origin so that the center of the dryers aligned exactly over the heat flux sensor.

Because the measurements under the center cassette were the only important measurements, the final grid of points was aligned with the center cassette. The parameters for the final experimental procedure are laid out in Table 15.

Table 15: Final testing parameters.

Parameter	Description	Numerical Value
M	Number of rows in measurement grid	13
N	Number of columns in measurement grid	7
L_{meas}	Length of measurement grid	6 in
H_{meas}	Height of measurement grid	12 in
H_{clear}	Clearance height between surface and cassettes	1 in
$\dot{m}_{air}$	Mass flow rate of supply air	200 scfm
T_w	Setpoint of the cooling water chiller	16 C
Lamp Type	Type of lamp	Varied
Glass Type	Type of glass plate	Varied
$\dot{q}_{supply}$	Electrical power supplied to three cassettes	Varied
t_{ss}	Time spent waiting at each point allowing the heat flux to reach steady-state value	20 sec
t_{meas}	Time required for the DAQ to log measurements	5 sec
SR	Sampling rate of the DAQ	20 S/sec

The above parameters show that data was taken at 13 x 7 = 91 measurement points, with the *x*- and *y*-distance between points (*dx* and *dy*) both equal to 1 in. The above table also shows that the lamp type, glass type, and supply power were varied from run-to-run; these were the three factors considered in the experiment. While there were numerous other factors that could be tested in the experiment (such glass thickness, reflector type, supply air flow rate, clearance height, etc), time constraints on the experiment only allowed for the lamp type, glass type, and supplied power level to be investigated. Table 16 displays the different levels tested for each factor.

Table 16: Investigated factors and their respective levels.

Lamp Type	Glass Type	Power Level
Short Wave (SW)	Ceramic (C)	6.0 W/m^2
Fast-Response Medium Wave (FRMW)	Quartz (Q)	9.4 W/m^2

Medium Wave (MW)	

A run's power level corresponded to the supplied electrical power and lighted area of the three cassettes, as shown in Eq. (131).

$$power\ level = \frac{\dot{q}_{supply}}{L_{lit} W_{htr}} \tag{131}$$

Testing various lamp types at the same power level accounted for the fact that different lamps have different filament lengths, which can affect the dryer's heat flux distribution.

The final experimental procedure only recorded measurements under the center dryer cassette—it did not read measurements under the two outer dryer cassettes. However, the dryer radiation model from Ch. 4 did include these surfaces in the model. To compare the experimental and model results, some temperature value needed to be input into the model for the surfaces under the outside cassettes. Because the final procedure had no measurements associated with these surfaces, the following empirical correlation was applied to determine the approximate surface temperature to use:

$$T_{sides} = 0.73\left(T_{max} - T_{amb}\right) + T_{amb} \tag{132}$$

where T_{max} is the maximum temperature recorded, T_{amb} is the ambient temperature, and T_{sides} is the temperature to apply to the model surfaces that are under the side cassettes. The 0.73 [-] ratio was based upon the data from the preliminary test run discussed above. The surface temperature of the area directly under one of the side cassettes is plotted in Figure 56.

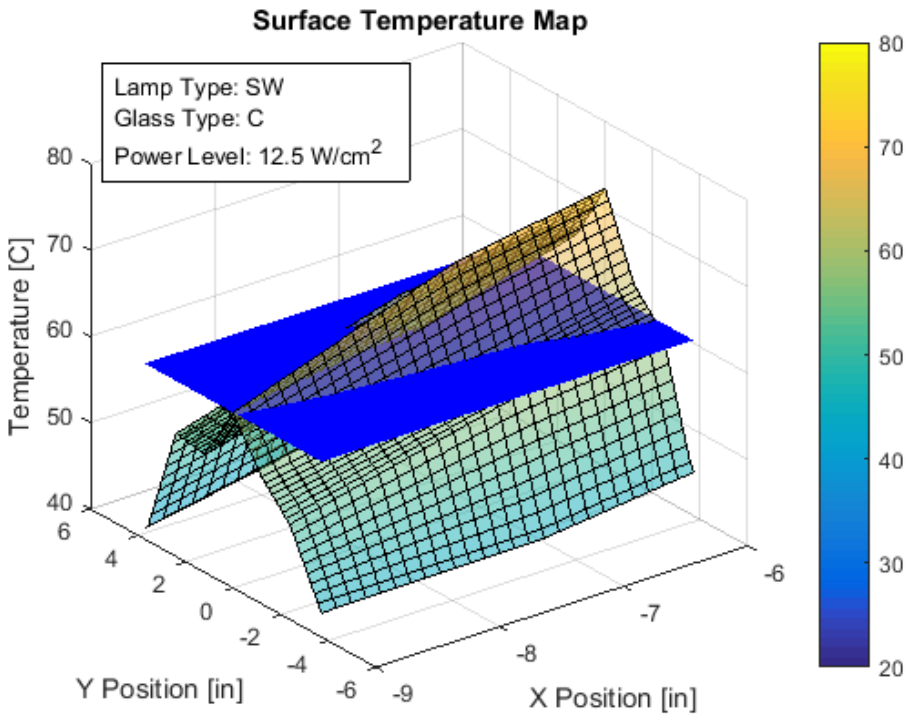

Figure 56: Surface temperature under the left side cassette.

The blue planar surface illustrates the average measured surface temperature across the entire side cassette area. This average surface temperature was 60.3 °C, the ambient temperature was 21 °C, and the max temperature of the entire run was 75 °C. These numbers produce a temperature ratio of 0.73 [-]. This ratio provided an algorithm to calculate the surface temperature under the side cassettes for future runs where measured data was not available. While it would be ideal to actually measure the surface temperature and heat flux under the side cassettes, it was an extra step that did not significantly affect the comparison between the experiment and the model.

5.6 Estimation of Reflector Convection Coefficient

Before beginning the experiment runs, a single-point experiment was performed to help estimate the convection coefficient that the reflector experiences. To estimate the convection coefficient, the dryers were positioned at a clearance height of 1 in, and the center of the

cassettes were located directly over the heat flux sensor and the three thermocouples. The lamps were supplied with power, and all the measured variables (heat flux, surface temperature, reflector temperature, etc.) were allowed to reach steady-state. The power supplied to the lamps was cut, such that their emitted radiation dropped drastically. With the lamps turned off, convection became the dominant mode of heat transfer, especially when the lamps' filaments cooled to near ambient temperature. Because convection was dominant, the reflector temperature followed a 1st-order system with time constant, τ. The time constant was determined from the experimental measurements and used to calculate the convection coefficient. The time history (both dimensional and non-dimensional) of the reflector temperature is shown below in Figure 57.

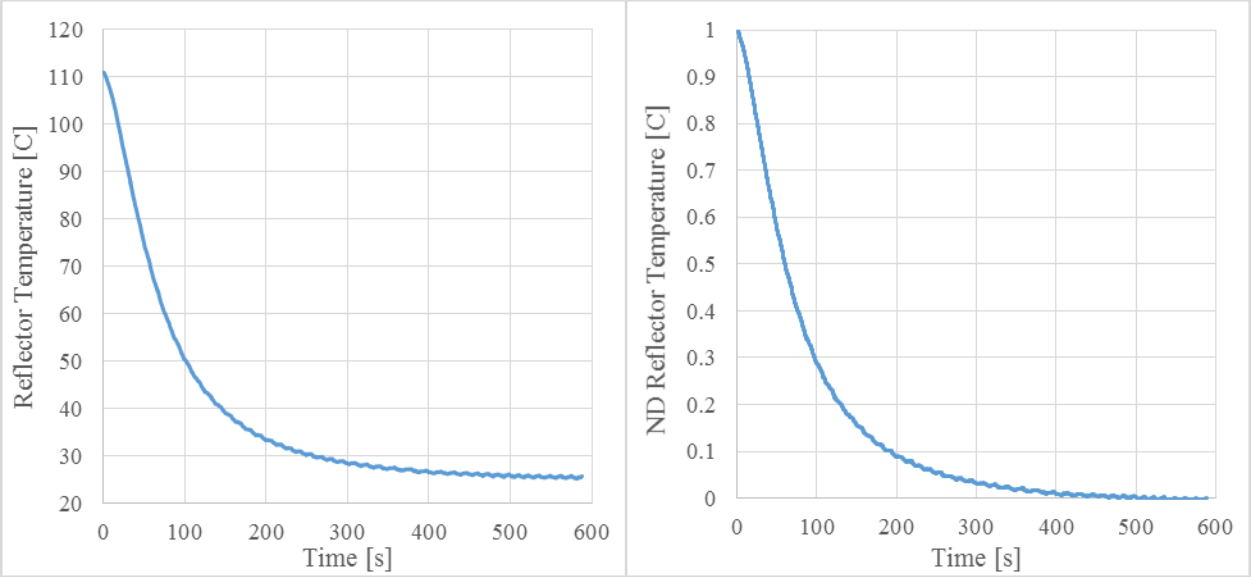

Figure 57: Time constant analysis to determine the convection coefficient at the reflector.

Since the reflector behaved as 1st-order system, the reflector temperature reached 63.2% of its change within one time constant. Furthermore, the temperature reached 95% of the change within three time constants. The non-dimensional reflector temperature shows where the temperature reached these changes, along with the elapsed time since the step change in the

supply power. When the temperature dropped by 63.2%, 82 seconds had elapsed; τ = 82 s. After 250 seconds, the temperature dropped 95%; 3τ = 250 s, or τ = 83 s.

The reflector's time constant is correlated to its convection coefficient by Eq. (133):

$$\tau = \frac{\rho V c}{\bar{h} A_s} \rightarrow \bar{h} = \frac{\tau A_s}{\rho V c} \tag{133}$$

where ρ, V, c, and A_s are the reflector's density, isothermal volume, specific heat, and surface area exposed to convection, respectively. The reflector is made of stainless steel, spans the entire cassette area, and is approximately 1 mm thick. Assuming the entire reflector was at the measured temperature, the convection coefficient associated with a time constant of 82 seconds was calculated to be $\bar{h}$ = 49 W/m^2-K.

The above time constant analysis assumed that the reflector was only exposed to convection from the forced air, and thus exactly obeys a 1st-order system. This was not the case; immediately after turning off the power, the reflector still received some radiation because the filaments (and glass bulbs and glass plate) were at such a high temperature that they were unable to instantaneously drop to the ambient temperature when the power was cut. For this reason, the reflector likely took longer to reach ambient than if the reflector was only experiencing convection. The reflector's actual convection coefficient was probably slightly higher than the calculated 49 W/m^2-K, so a value of 60 W/m^2-K was assumed for use in the dryer radiation model.

The time constant analysis could not have been applied to the recorded surface temperature to determine the surface's convection coefficient because the surface temperature did not behave like a 1st-order system. Unlike the reflector, when the lamp power was turned off, the chill surface was exposed to convection from the forced air and cooling from the water in the chill tubes. The time history of the chill surface temperature would have been representative of

both processes, and so the analysis would not be able to accurately determine the forced air convection coefficient alone. Furthermore, the chill surface did not experience a step change when the lamp power was turned off. The chill surface was exposed to the forced air after it exited the dryer cassettes; the forced air cooled cassette surfaces and thus it left the cassette at a higher temperature than when it entered. When the lamp power was shut down, the cassette surfaces began to cool and the temperature of the forced air leaving the cassettes also started to drop. The chill surface was no longer exposed to a step change in its thermal environment, thus the 63.2% and 95% rules would no longer apply to the situation. To demonstrate that the forced air outlet temperature change, its time history is shown below in Figure 58.

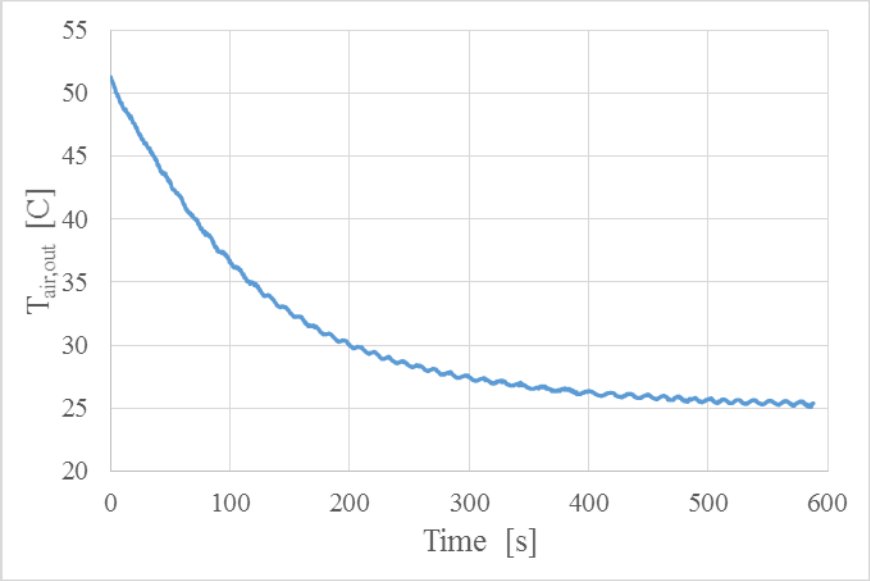

Figure 58: Forced air outlet temperature after lamp power step change.

Ch. 6 Experimental Results and Comparison with Dryer Radiation Model

The results of the experiment (outlined in Ch. 5) are presented, along with comparisons to the results from the dryer radiation model (described in Ch. 4). The experimental parameters that remained constant for all runs of the experiment were shown in Table 15, and the three factors investigated with their various levels were described in Table 16. To aid in comparing the different results, all heat flux distributions are presented with the same *x*- and *y*-axis scales.

6.1 Experimental Heat Flux Results

The experimentally measured and averaged 1-D heat flux distributions for all runs are shown in this section, with errors bars that represent the ± 3% sensor uncertainty at each location. See Appendix B: to see the individual heat flux maps for all 12 runs.

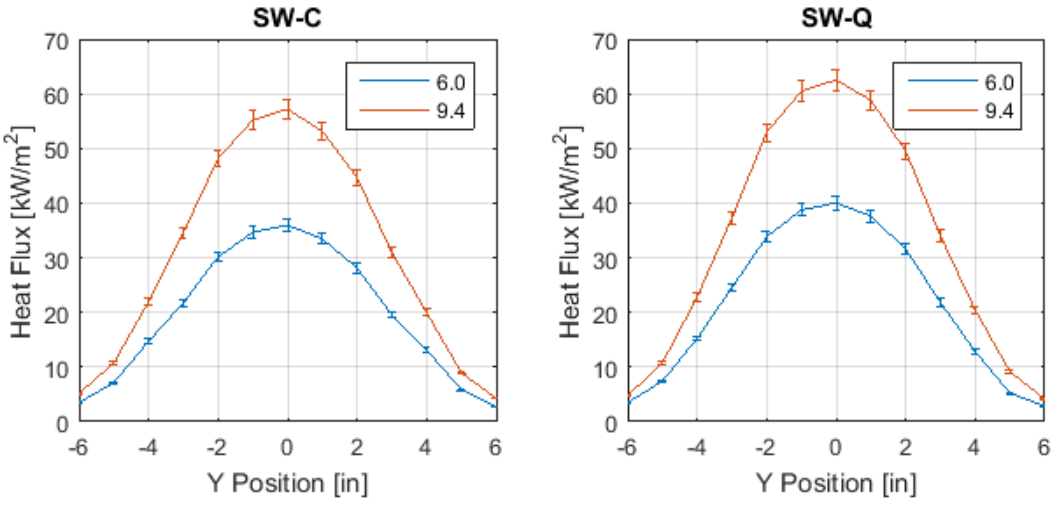

Figure 59: SW, experimental, 1-D heat flux distribution.

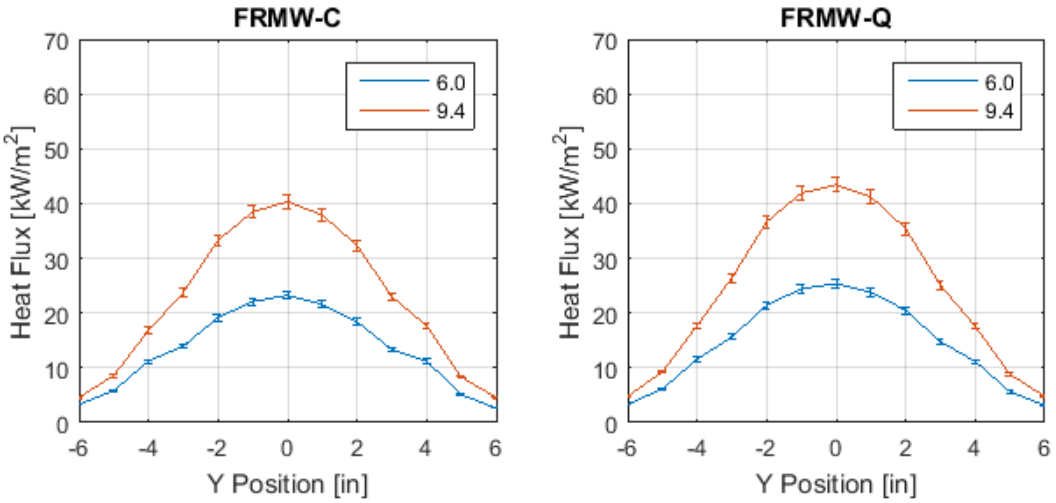

Figure 60: FRMW, experimental, 1-D heat flux distribution.

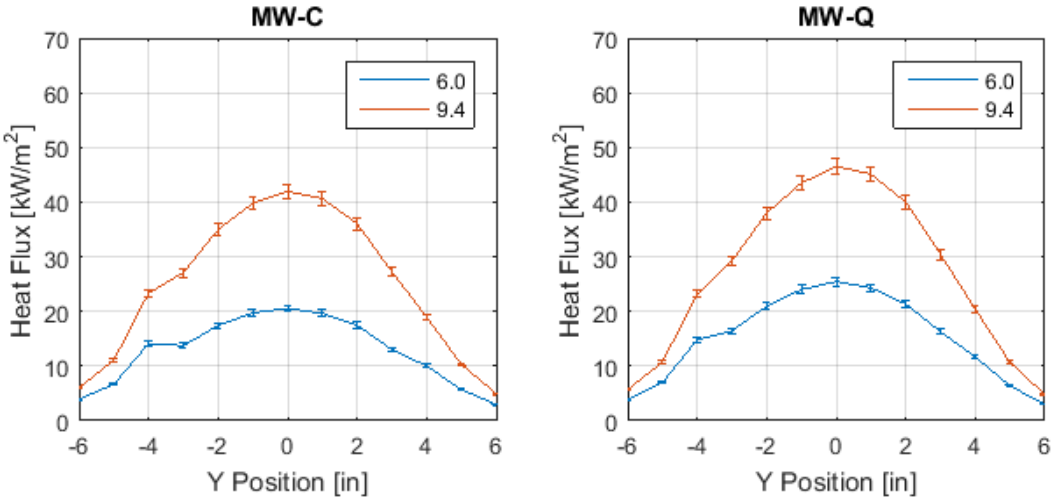

Figure 61: MW, experimental, 1-D heat flux distribution.

6.2 Comparison of Experimental and Model Heat Flux

The 1-D heat flux distributions from the experiment and the dryer radiation model are plotted in the figures below. All error bars represent the ± 3% sensor uncertainty.

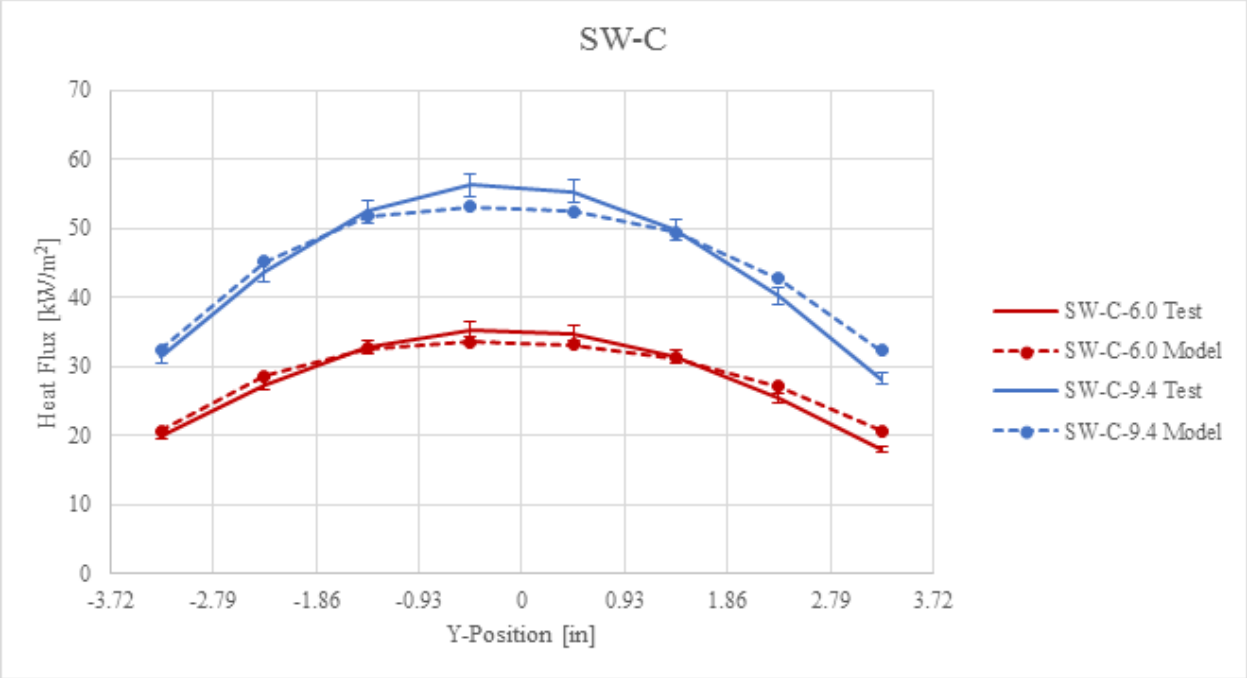

Figure 62: Comparison of SW-C experimental and model heat flux distributions.

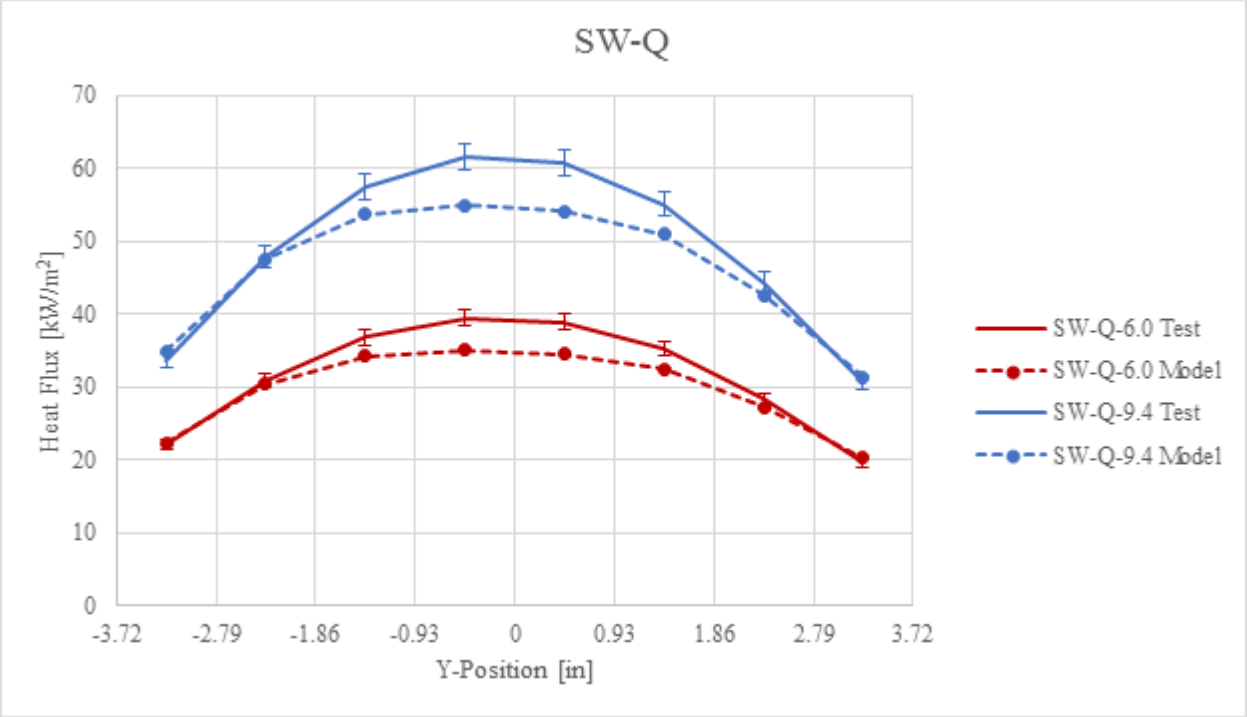

Figure 63: Comparison of SW-Q experimental and model heat flux distributions.

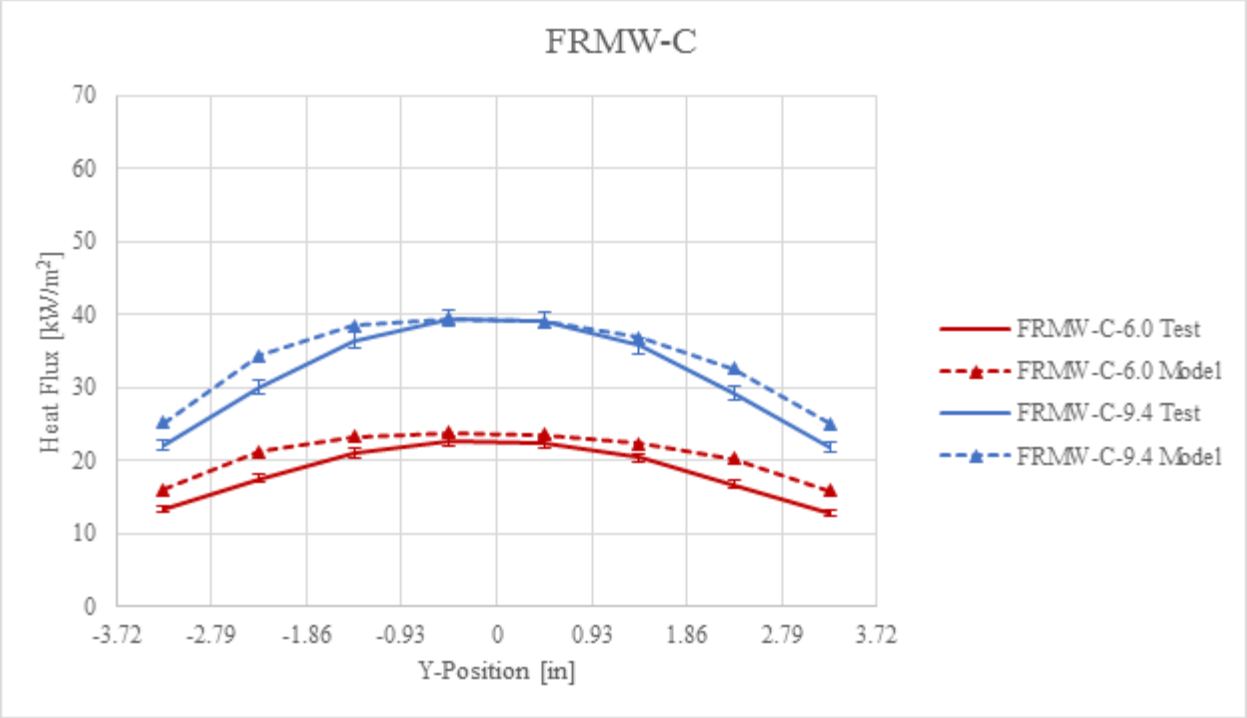

Figure 64: Comparison of FRMW-C experimental and model heat flux distributions.

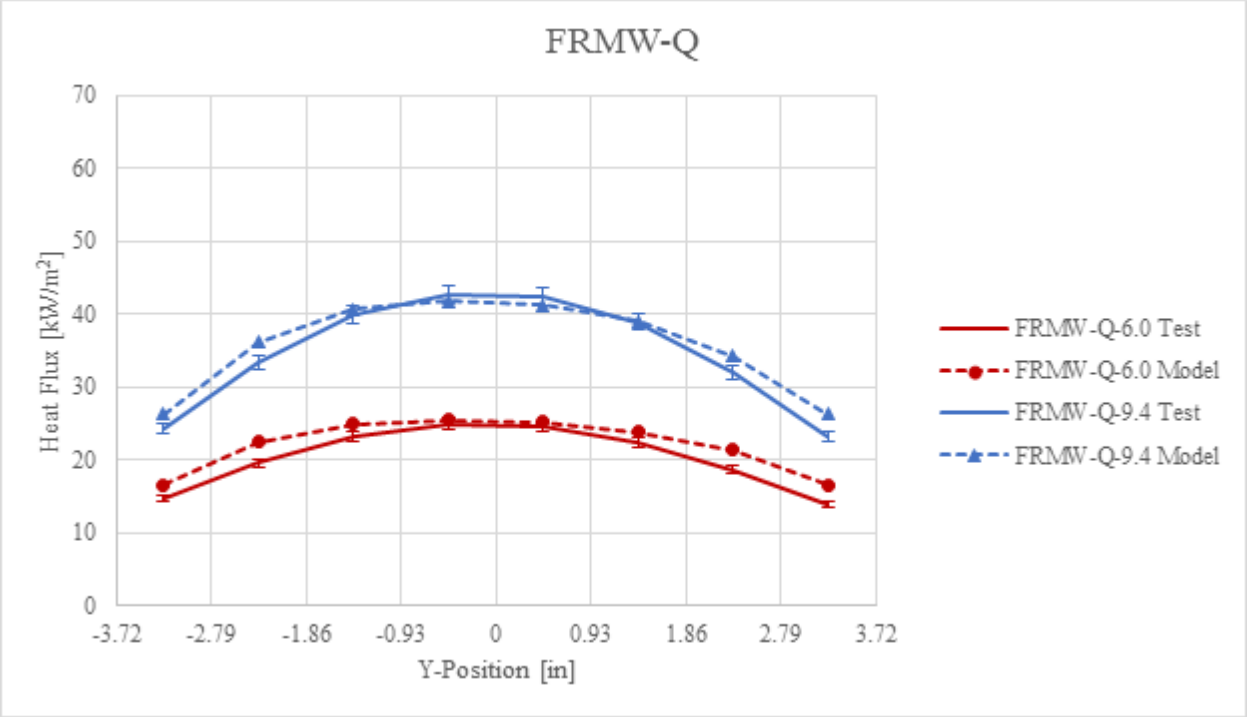

Figure 65: Comparison of FRMW-Q experimental and model heat flux distributions.

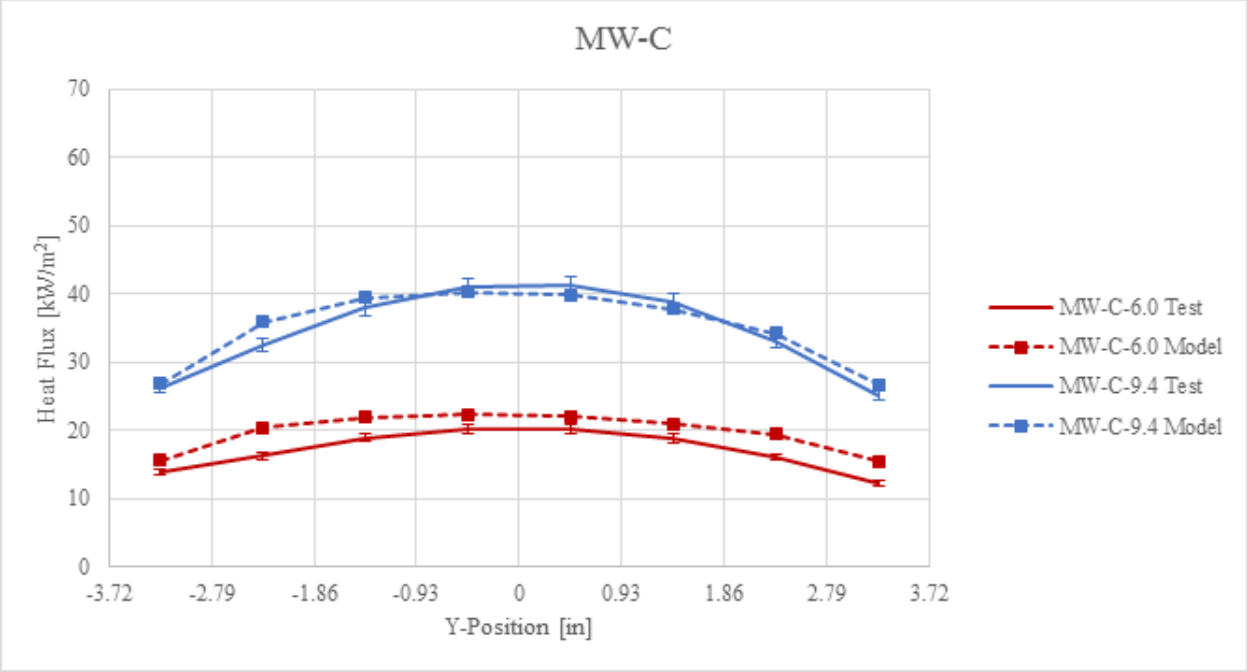

Figure 66: Comparison of MW-C experimental and model heat flux distributions.

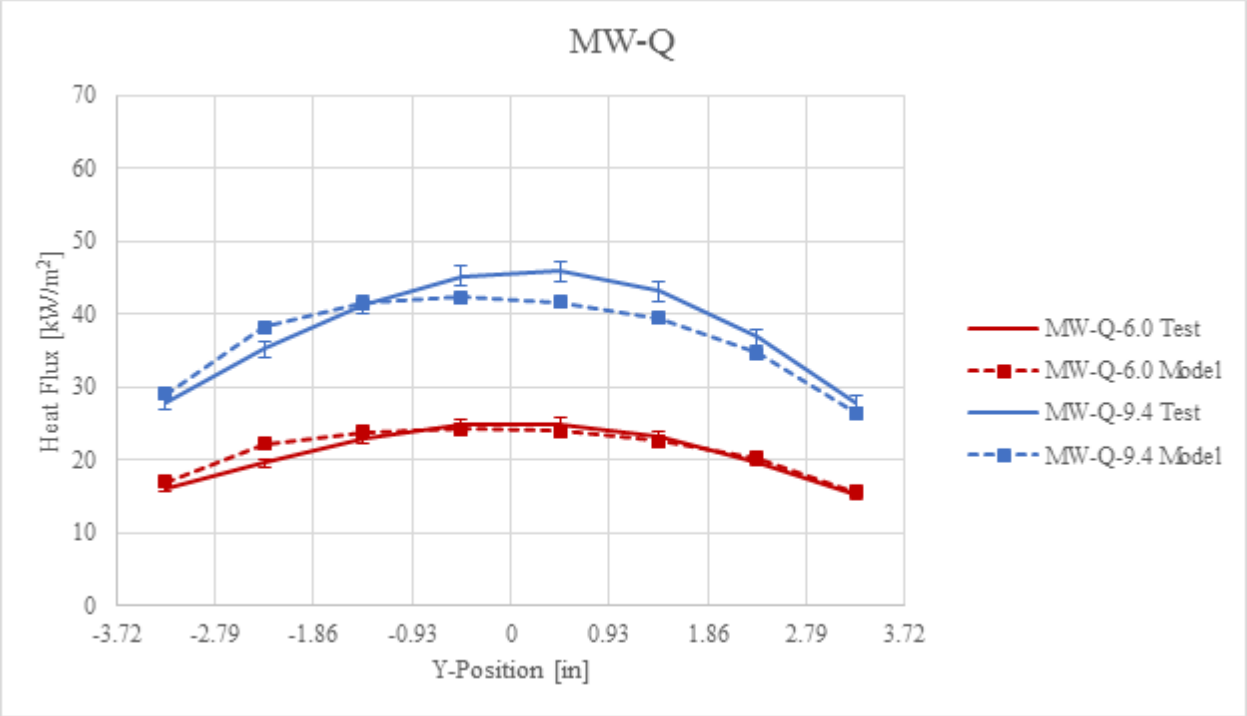

Figure 67: Comparison of MW-Q experimental and model heat flux distributions.

On average, the dryer radiation model heat flux values differed from the experimental heat flux values by only 7.6%, implying that the dryer radiation model closely simulates the

actual thermal radiation exchange. The above figures demonstrated a similar pattern: the model tended to over-predict the heat flux at the cassette edges and under-predicted the heat flux at the center of the cassette. This was probably because the model used the STRM, which assumed all the surfaces were diffuse-emitting and diffuse-reflecting. In reality, the dryer surfaces involved were likely specular for reflected radiation; this specular property may have reduced the amount of radiation seen by the edges of the board.

The above 1-D heat flux distributions were numerically integrated to determine the total heat transfer rate into the board surface.

Table 17: Experimental and model board total heat transfer rate.

Lamp	Glass	Power Level [kW/m^2]	Experimental Heat Transfer Rate [W]	Model Heat Transfer Rate [W]	Percent Difference [%]
SW	**C**	6.0	802	811	1.1
		9.4	1,273	1,280	0.6
	Q	6.0	895	842	6.0
		9.4	1,395	1,319	5.5
FRMW	**C**	6.0	523	592	13.2
		9.4	905	964	6.6
	Q	6.0	577	628	8.8
		9.4	985	1,017	3.2
MW	**C**	6.0	486	563	16.0
		9.4	984	1,001	1.8
	Q	6.0	592	604	2.1
		9.4	1,080	1,045	3.3
Average Percent Difference of Total Heat Transfer Rate:					**5.7%**

The board's total heat transfer rate was divided by the power supplied to the center cassette to determine the dryer's efficiency for turning electrical power into radiative heat transfer to the board surface, as shown in Eq. (134).

$$\eta_{elec\rightarrow rad} = \frac{\dot{q}_{board,tot}}{\dot{q}_{supply,cass}} \tag{134}$$

These efficiency values, based both upon the experimental and model calculations, are displayed in Table 18.

Table 18: Experimental and model efficiencies.

Lamp	Glass	Power Level [kW/m^2]	Experimental Efficiency [%]	Model Efficiency [%]	Difference in Efficiencies [%]
SW	**C**	6.0	49.1	49.6	0.5
		9.4	52.3	52.6	0.3
	Q	6.0	54.8	51.5	3.3
		9.4	57.3	54.2	3.1
FRMW	**C**	6.0	32.0	36.2	4.2
		9.4	41.1	43.8	2.7
	Q	6.0	38.5	41.8	3.3
		9.4	44.8	46.2	1.4
MW	**C**	6.0	28.0	32.5	4.5
		9.4	36.4	37.1	0.7
	Q	6.0	33.5	34.2	0.7
		9.4	40.0	38.7	1.3
Average Difference in Efficiency:					**2.2%**

The average percent difference in the board's total heat transfer (5.7%) and the average difference in the dryer's radiation efficiency (2.2%) were both small. This small error between the model and experimental data provides confidence that the model accurately simulated the dryer's radiation exchange for different lamp types, glass types, and supplied powers.

6.3 Discussion of Experimental and Model Results

The previous section showed the measured experimental results and the model's calculated results. A factorial effects analysis was performed on both the experimental and model results to determine the impact of each factor on the dryer efficiency. Consider Table 19, which presents several different average efficiencies.

Table 19: Experimental and model average efficiencies.

Factor	Averaged Factor Level*	Experimental Efficiency	Model Efficiency	Experimental Effect**	Model Effect**
Lamp Type	SW	53.4%	52.0%	+11.1%	+8.8%
	FRMW	39.1%	42.0%	-3.2%	-1.2%
	MW	34.5%	35.6%	-7.8%	-7.6%
Glass Type	C	39.8%	42.0%	-2.5%	-1.2%
	Q	44.8%	44.4%	+2.5%	+1.2%
Power Level	6.0	39.3%	41.0%	-3.0%	-2.2%
	9.4	45.3%	45.4%	+3.0%	+2.2%
Overall Efficiency:		42.3%	43.2%		

* The "Averaged Factor Level" indicates which runs were averaged—i.e. "C" means that the efficiencies of runs with ceramic glass were averaged.
** Effect describes how the efficiency for the averaged factor level compares to the overall average efficiency—i.e. the experimental SW lamp had an efficiency of 11.1% higher than the average experimental efficiency (53.4% - 42.3% = +11.1%).

Table 19 shows that the lamp type was the largest main effect on the dryer efficiency for both the experimental and model results. The SW lamps had the highest efficiency, followed by the FRMW and then MW lamps. The quartz glass outperformed the ceramic glass and the high power level (9.4 W/cm^2) had increased efficiency over the low power level (6.0 W/cm^2). All of these observations align with intuition. The higher color temperature lamps emitted more radiation at low wavelengths where the glasses were more transmissive, which leads to a better efficiency. The quartz glass's transmission curve was slightly more transparent than the ceramic glass's transmission spectrum, which increased the dryer's efficiency. The high power level

increased the color temperature of the lamps compared to the low power level, which allowed more radiation to be emitted at short wavelengths where the glasses were more transparent.

Section 6.2 proved the dryer radiation model closely simulated the experimental procedure. With the confidence that the model can accurately mimic the dryer's radiation exchange, the model's results can be analyzed further to deliver a more profound insight regarding the radiation exchange. Unlike the experiment, where only key measurements were recorded, the model tracks all aspects of the radiation exchange, including the spectral radiation, convection, and temperature of all the surfaces involved.

The spectral radiation of the board surface for the 12 combinations of lamp, glass, and power level are shown below, all with the same *x*- and *y*-scales to help compare the plots.

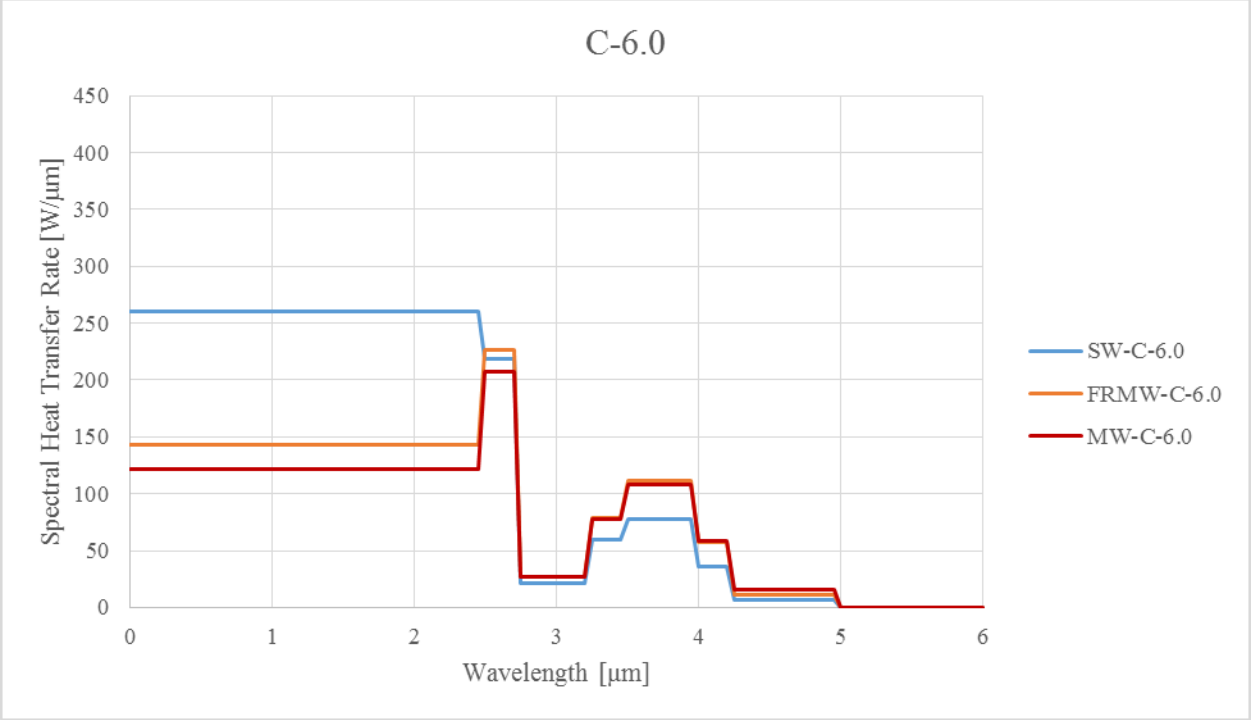

Figure 68: C-6.0 spectral distribution of absorbed radiation.

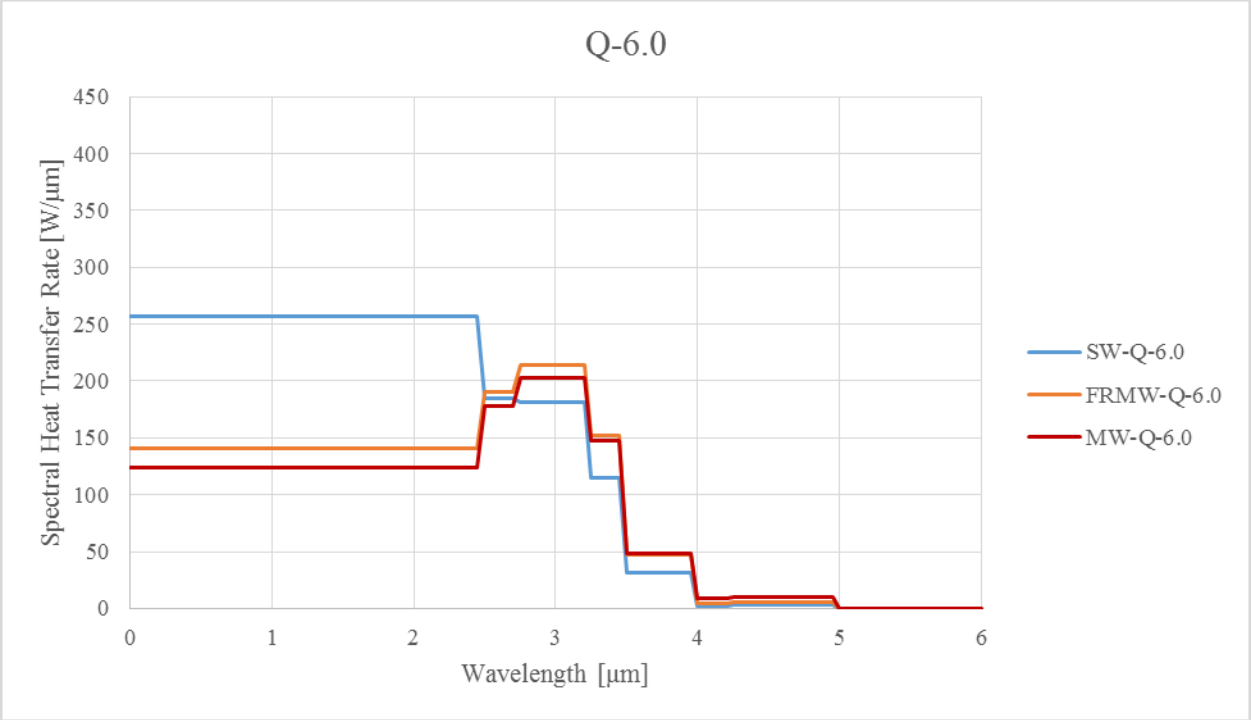

Figure 69: Q-6.0 spectral distribution of absorbed radiation.

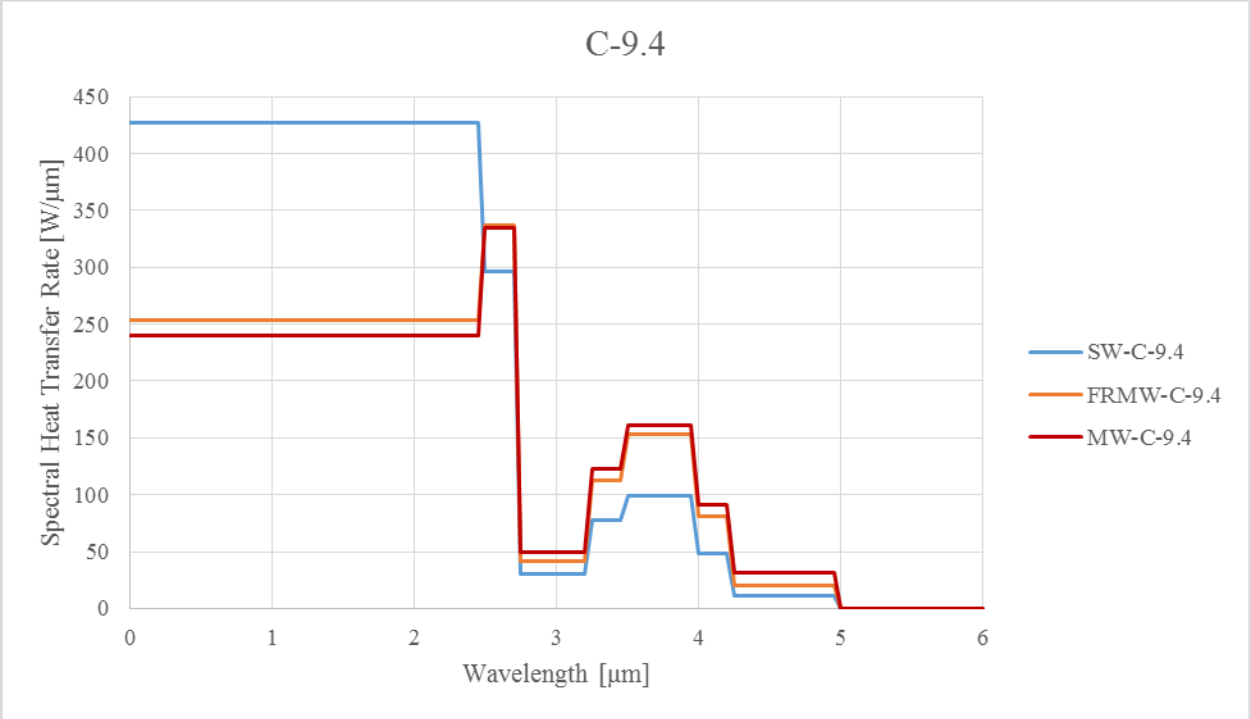

Figure 70: C-9.4 spectral distribution of absorbed radiation.

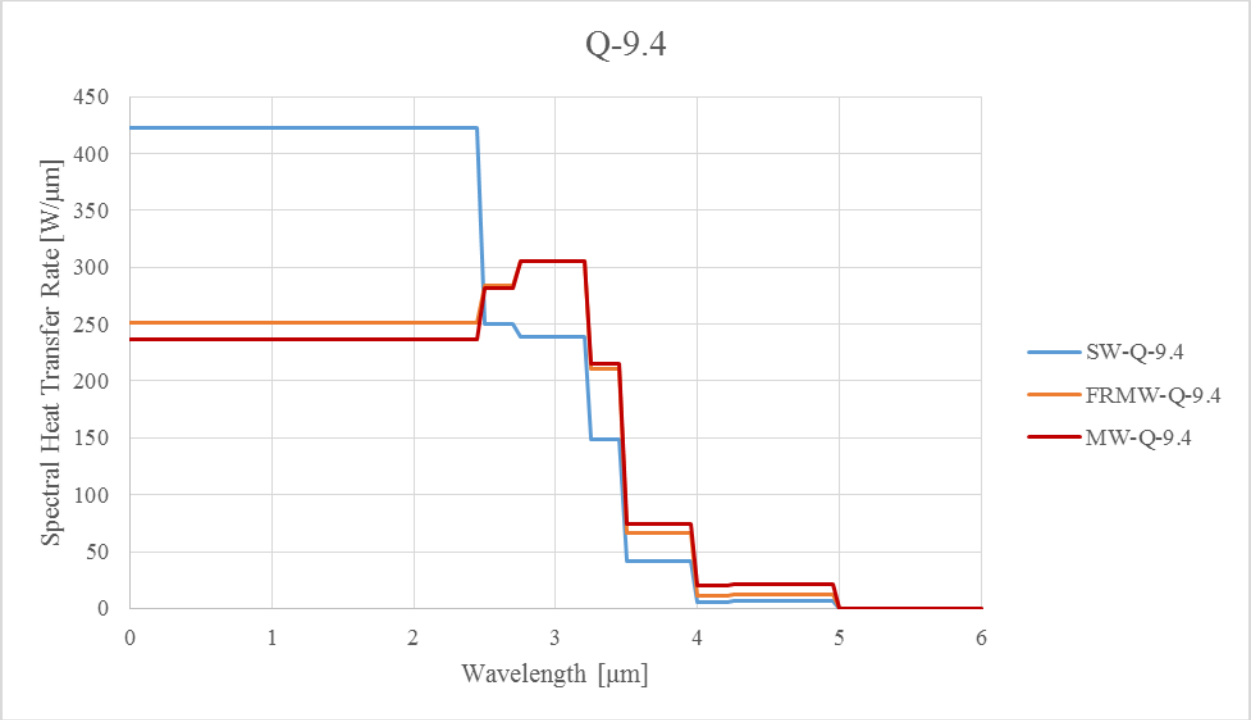

Figure 71: Q-9.4 spectral distribution of absorbed radiation.

When the dryers were equipped with the SW lamps, the board received the vast majority of its radiation in the lowest wavelength band ($\lambda < 2.5$ µm). This explains why the SW lamp's efficiencies in Table 18 were noticeably higher than the FRMW and MW efficiencies. The SW lamps emitted most of their radiation at low wavelengths where the glasses were the most transmissive, meaning more of the lamps emitted radiation was incident on the board. This also explains why the efficiency for a dryer with a given lamp-glass combination was higher for the larger power levels. With the lamp and glass components held constant, increasing the power level caused the filaments to reach a hotter temperature and emit more radiation at shorter wavelengths where the glass bulb and glass plate were the most transmissive. Increasing the power level increased the efficiency of the dryer because more radiation transmitted through the glass to the corrugated board.

The spectral plots demonstrate that the FRMW and MW lamps produced a similar board absorption spectrum, despite the fact that their rated color temperatures differed by 700 K. The

spectrums were similar because the lamps' filaments were actually at very similar temperatures. Table 20 shows what the model calculated for the filament temperatures of the different lamp, power level combinations. It is not surprising that the FRMW and MW were at similar temperatures because of their rated powers. When a lamp manufacturer specifies the color temperature of a lamp, they also specify the rated power the lamp should be operated at to obtain that color temperature. The FRMW lamp's rated power was 950 W, while the MW lamp's rated power was 480 W. In the 6.0 W/cm^2 runs, each FRMW lamp was powered with 375 W (significantly below its rated power), while each MW lamp was supplied with 433 W of power (almost at its rated power). For the 9.4 W/cm^2 runs, each FRMW lamp used 550 W of power and each MW lamp dissipated 675 W. The lamps acted as expected in relation to their rated powers.

Table 20: Model-calculated filament temperatures.

Filament Temperature		**Power Level**	
		6.0 [W/cm^2]	**9.4 [W/cm^2]**
Lamp	**SW**	1754 K	1931 K
	FRMW	1268 K	1393 K
	MW	1223 K	1364 K

The model also tracked the energy transfer due to convection at all surfaces. The magnitude of convection at the board surface ranged up to 26 W, which was very small compared to the model's total heat transfer rate of the board—across all factor combinations, the maximum percentage of the board's heat transfer rate that is due to convection was 4.1%. This reinforced the calculations done in Ch. 2 because the dryer radiation model determined that radiation was the dominant mode of heat transfer at the board surface, and convection was negligible.

Convection is still important to the radiation exchange in the dryer, as convection is the largest source of energy loss in the system. Energy that leaves a surface via convection was considered "energy loss" because that convection energy was not significantly adding to the heat transfer at the board surface. For instance, Table 21 displays the convection leaving each of the surfaces involved for the SW-C-9.4 factor combination. Surfaces 15, 16, and 30 were not included since they were pseudo-surfaces that modelled the surroundings.

Table 21: Convection leaving each surface for the SW-C-9.4 factor combination.

Surface #	Surface	Convection [W]
1-12	Bulbs	634.8
13-14	Reflector Sides	29.0
17	Reflector	518.3
18-19	Glass Plate	1,391.7
20-27	Board-Center	18.9
28-29	Board-Sides	41.0
	Sum:	**2,633.7**

The convection leaving the glass plate surfaces combined to be 53% of the total amount of energy lost to convection. This suggests that the dryer would realize large efficiency improvements if the glass plate were not present, because the lamps' radiation would not be absorbed and convected away by the glass plate. The data in Table 21 is only for the SW-C-9.4 combination; since the SW and 9.4 combination emits much of its radiation at short wavelengths, the negative impact of the glass plate should be more profound with other combinations that emit radiation at longer wavelengths where the glass was more absorptive. Table 22 presents the convected energy leaving the model surfaces for MW-C-6.0 factor combinations.

Table 22: Convection leaving each surface for the MW-C-6.0 factor combination.

Surface #	Surface	Convection [W]
1-12	Bulbs	889.6
13-14	Reflector Sides	21.8
17	Reflector	415.7
18-19	Glass Plate	1,587.3
20-27	Board-Center	-23.1
28-29	Board-Sides	-58.2
	Sum:	**2,833.1**

For the MW-C-6.0 factor combination, 56% of all the energy lost to convection was lost through the glass plate surfaces. Despite the fact that dryer was operated at less power, the MW-C-6.0 glass plate still convected away more energy than the glass plate in the SW-C-9.4 setup. This can be explained by their radiation spectrums. The MW-C-6.0 emits a larger percentage of its radiation at longer wavelengths than the SW-C-9.4. Because the glass is nearly opaque at long wavelengths, the presence of the glass plate has a greater impact on the efficiency of the MW-C-6.0 than the SW-C-9.4.

6.4 Results Comparison Overview

The dryer radiation model board heat flux distribution matched the experimentally measured heat flux distributions, which validated the accuracy of the dryer radiation model. Comparing the main effects of the factors showed that the lamp type had the largest impact on the dryer efficiency, but the other two factors still impacted the dryer performance. The presence of the glass plate negatively impacted the efficiency of the dryer, as it absorbed some of the lamps' radiation and convected the energy into the forced air. Convected energy was considered lost energy because convection contributed very little to the heat transfer process at the surface.

The above analysis assumed the board surface was opaque, and had an emissivity of 0.95, to match the heat flux sensor emissivity. In reality, the front liner surface likely has a lower emissivity, and may even transmit some of the incident radiation. It's even possible that the board could have spectral properties, where the board transmits radiation at certain wavelengths, but absorbs it at other wavelengths. These radiant properties would greatly affect the efficiency of the dryer in transferring heat to the board surface.

Ch. 7 Updated Drying Model

In Ch. 2, an initial drying model was created that analyzed the heat transfer process at the printed surface. The model included the effects of the radiant heat flux from the IR lamps, convection to the forced air, conduction within the printed surface, and mass transfer from the evaporating ink moisture. The results of the initial drying model showed that the radiation heat flux was the dominant mode of heat transfer and had the largest impact on the drying process. Section 2.4 also explained that the absorption distribution within the corrugated board could potentially significantly influence the drying process.

The initial model assumed that the radiant energy incident on the board was constant and equal to the blackbody emissive power defined by the lamps' color temperature. Because radiation was the dominant mode of heat transfer, the validity of this assumption greatly impacts the accuracy of the initial drying model. While this assumption was appropriate for the initial drying model, the dryer radiation model (explained in Ch. 4) was created to provide a better estimate of the radiant heat flux that the front liner receives as it passes over the dryer. The dryer radiation model was based upon actual drying parameters—lamp type, glass type, supplied power, clearance height, etc.—which allowed the model to calculate a realistic heat flux distribution. The dryer radiation model was validated by an experiment, described in Ch. 5. The corrugated board's radiation heat flux in the initial drying model can be improved upon by using the heat flux distribution produced by the dryer radiation model.

The initial model also assumed that the corrugated board's front liner only absorbed a small fraction of the incident radiation which allowed the assumption of an equally-distributed radiation distribution across the thickness of the front liner. This assumption is likely to have a substantial impact on the drying process, as noted in section 2.4. While no work was done to

determine how the radiation is actually absorbed in the front liner, several radiation absorption distributions have been considered to see the effect that this has on the drying process.

7.1 Drying Model with Varying Radiation Heat Flux

The 1-D radiant heat flux distribution calculated by the dryer radiation model was utilized to produce more accurate results from the initial drying model. After the dryer radiation model was run with the desired lamp type, glass type, and power level, the generated radiation-only heat flux distribution can be curve-fit. It is important that the curve is fit to the radiation-only heat flux distribution, and not the total heat flux (which includes radiation and convection). The drying model includes convection separately in the analysis. For example, Figure 72 shows the model's radiation heat flux distribution, and its 2nd-order polynomial fit for a dryer with short wave lamps (SW), ceramic glass plate (C), and supplied with a 9.4 W/cm^2 power level.

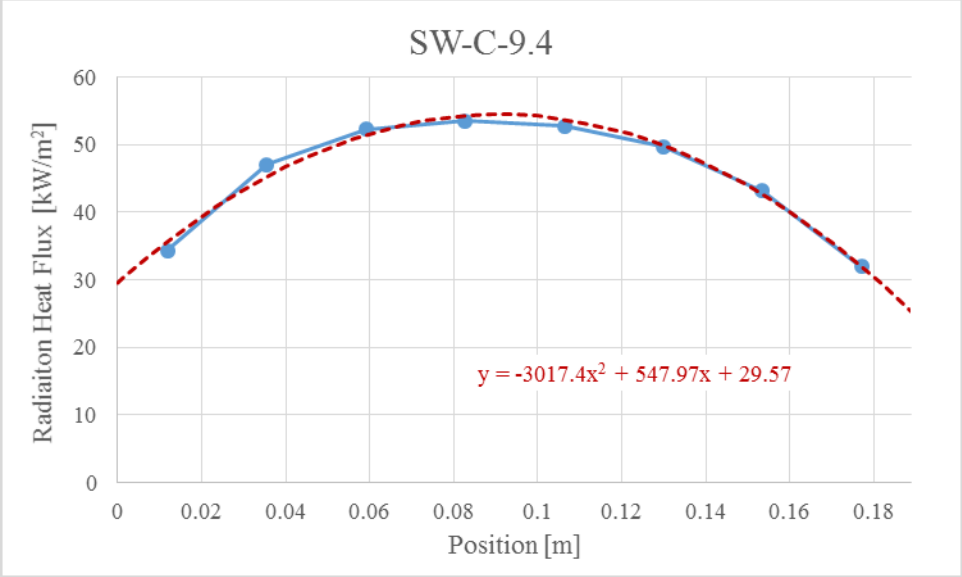

Figure 72: Model-determined heat flux distribution for SW-C-9.4.

Notice that the radiation distribution was positioned so that the left edge of the dryer was aligned at 0 m. This is different from the experimental measurements, but necessary to get the correct curve fit for implementation in the drying model. Because the radiation heat flux

distribution is determined from the dryer radiation model that already accounts for the board's emissivity, the heat flux distribution shown in Figure 72 represents the radiation heat flux that is absorbed by the board at various *x*-positions. To implement the radiation heat flux from Figure 72 in the drying model, Eq. (135) was input into the model:

$$\dot{q}''_{rad} = \begin{cases} -3{,}017.4\frac{kW}{m^4}x^2 + 547.97\frac{kW}{m^3}x + 29.57\frac{kW}{m^2}, & for\ 0 < x < L_{htr} \\ 0\frac{kW}{m^2}, & for\ x > L_{htr} \end{cases} \quad (135)$$

where $\dot{q}''_{rad}$ is the absorbed radiation heat flux and L_{htr} is the length of the dryer. Equation (135) shows that when the board is under the dryer, the radiation heat flux that the board absorbs is a function of its position, *x*, and when the board is not under the dryer, the board does not absorb any radiation heat flux.

The drying model's convection process was updated in a similar fashion. In the initial drying model, the convection coefficient was considered to be constant and equal to 100 W/m^2-K throughout the entire process, regardless of position. In reality, the jet holes at the ends of the dryers create a convection coefficient distribution dependent on the board's position relative to the dryer. A convection coefficient distribution was input into the model according to Eq. (136):

$$\bar{h} = \begin{cases} \bar{h}_\infty + \left(\bar{h}_{\max} - \bar{h}_\infty\right)e^{-\frac{x^2}{2\sigma^2}}, & for\ 0 < x < \frac{L_{htr}}{2} \\ \bar{h}_\infty + \left(\bar{h}_{\max} - \bar{h}_\infty\right)e^{-\frac{(x-L_{htr})^2}{2\sigma^2}}, & for\ x \geq \frac{L_{htr}}{2} \end{cases} \quad (136)$$

where $\bar{h}_\infty$ is the convection coefficient of the board when its far away from the jet holes, $\bar{h}_{max}$ is the maximum convection coefficient, and σ is the standard deviation of convection coefficient under each jet hole (a measure of the spread of convection coefficient distribution). Equation

(136) is an adaptation to the normal probability density function, such that when $x = 0$ or L_{htr} (where the jet holes are located), Eq. (136) simplifies to $\bar{h}_{max}$, as shown in Eq. (137):

$$\bar{h} = \bar{h}_{\infty} + \left(\bar{h}_{\max} - \bar{h}_{\infty}\right) \underbrace{e^{-\frac{0^2}{2\sigma^2}}}_{=1} = \bar{h}_{\infty} + \left(\bar{h}_{\max} - \bar{h}_{\infty}\right) = \bar{h}_{\max} \tag{137}$$

As x deviates from 0 or L_{htr} (the location of the jet holes), the convection coefficient drops according to $e^{-\frac{\delta^2}{2\sigma^2}}$, where δ is the distance from x to 0 or L_{htr}, respectively. As x moves far away from 0 or L_{htr}, the convection coefficient asymptotes at $\bar{h}_{\infty}$, as shown in Eq. (138).

$$\bar{h} = \bar{h}_{\infty} + \left(\bar{h}_{\max} - \bar{h}_{\infty}\right) \underbrace{e^{-\frac{\infty^2}{2\sigma^2}}}_{\approx 0} = \bar{h}_{\infty} \tag{138}$$

The numerical values for the parameters of the convection coefficient distribution are provided in Table 23. Figure 73 illustrates a plot of the radiation heat flux absorbed by the board and the convection coefficient as the board passes over the dryer.

Table 23: Convection coefficient distribution parameters.

Variable	Description	Nominal Value
$\bar{h}_{\infty}$	Convection coefficient far away from jet holes	15 W/m^2-K
$\bar{h}_{max}$	Conveciton coefficient directly aligned with the jet holes	110 W/m^2-K
σ	Standard deviation of the convection coefficient distribution—measure of the spread of the distribution	1 in

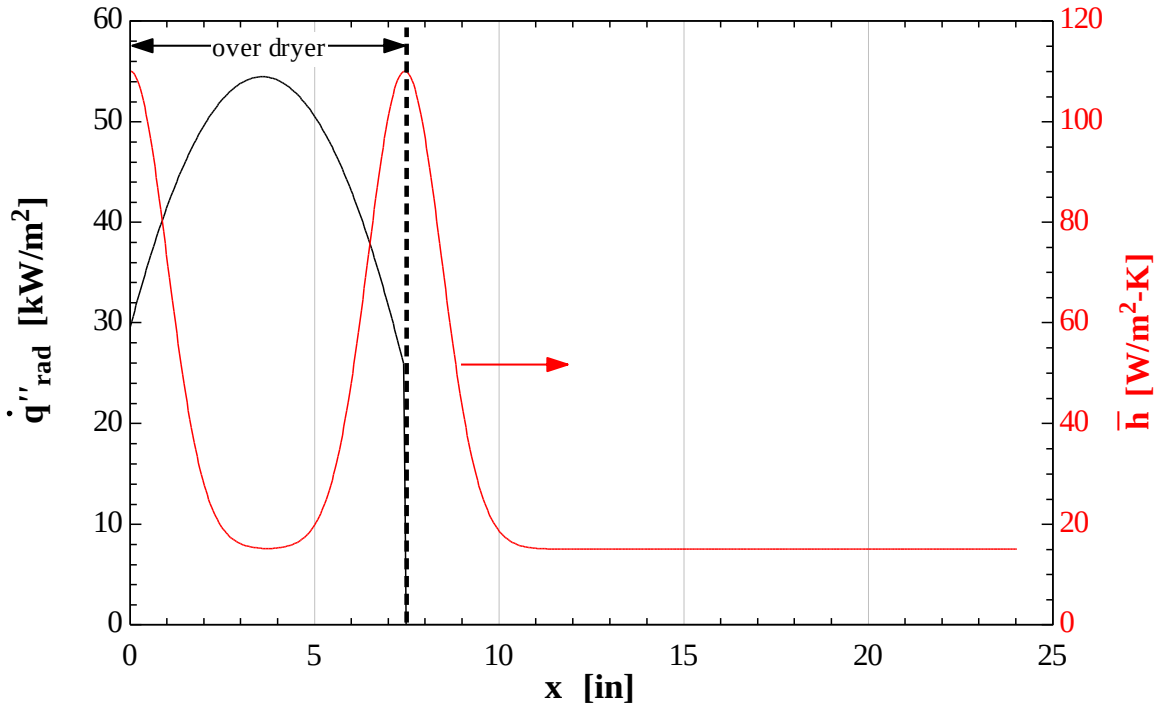

Figure 73: Absorbed radiation heat flux and convection coefficient distributions.

The rest of the drying model remained the same as was described in Ch. 2. The absorbed radiation was uniformly distributed throughout the thickness of the board's front liner. The mass transfer process was still modeled using the mass-heat transfer analogy. Almost all the parameters in Table 2 remained the same, except $E_{b,lamp}$, f_f, and $\bar{h}$ were unnecessary because the radiation and convection are implemented via Eqs. (135) and (136), and ΔT_{htr} was updated to 27 C to be consistent with the experimental results. The temperature and moisture distribution produced by the drying model with the varying heat flux and convection coefficient is shown in Figure 74.

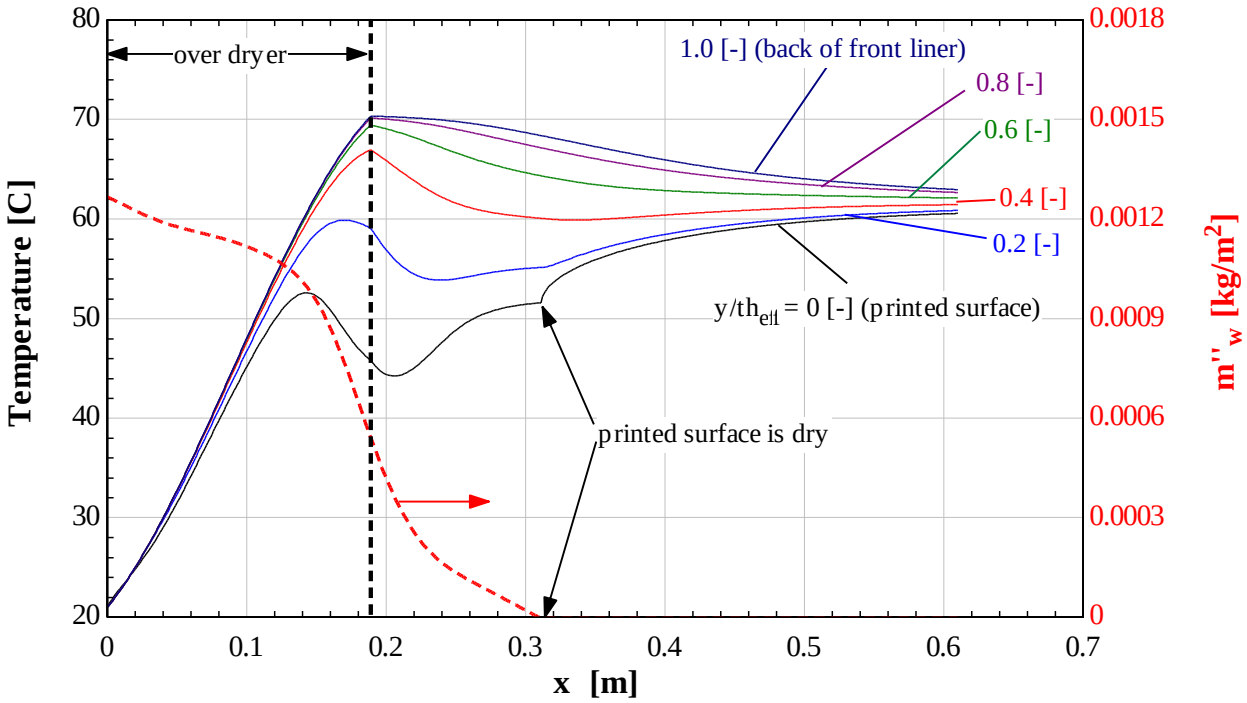

Figure 74: Temperature and moisture content of the corrugated board.

The temperature distribution of the board in Figure 74 makes sense. The equally-distributed radiation heat flux caused the entire board to rise in temperature together initially. The ink's moisture was only present at the printed surface, and so once the printed surface reached a temperature that was conducive to mass transfer (at about $x \approx 0.1$ m), the board's printed surface temperature started to lag the rest of the front liner's temperature because the mass transfer began to cool the surface. As the board approached the end of the dryer ($x \approx 0.15$ m), the hot board temperature and proximity to the dryer's second row of jet holes (which increased the mass transfer coefficient) caused the rate of mass transfer to increase, significantly cooling the board. As the board exited the heated length, the printed surface was not yet dry, but the internal parts of the front liner still provided heat transfer to the printed surface via conduction since the internal sections of the front liner were at a higher temperature than the surface. The printed surface still experienced a high mass transfer coefficient immediately after exiting the dryer, thus the mass transfer process still occurred until all the moisture was dried at x

≈ 0.31 m. When the printed surface became dry, the printed surface no longer experienced the cooling effect of mass transfer, and thus the surface experienced an instantaneous spike in the printed surface's temperature. Eventually all of the temperatures across the board equilibrate.

A comparison of the modes of heat transfer at the printed surface is shown in Figure 75.

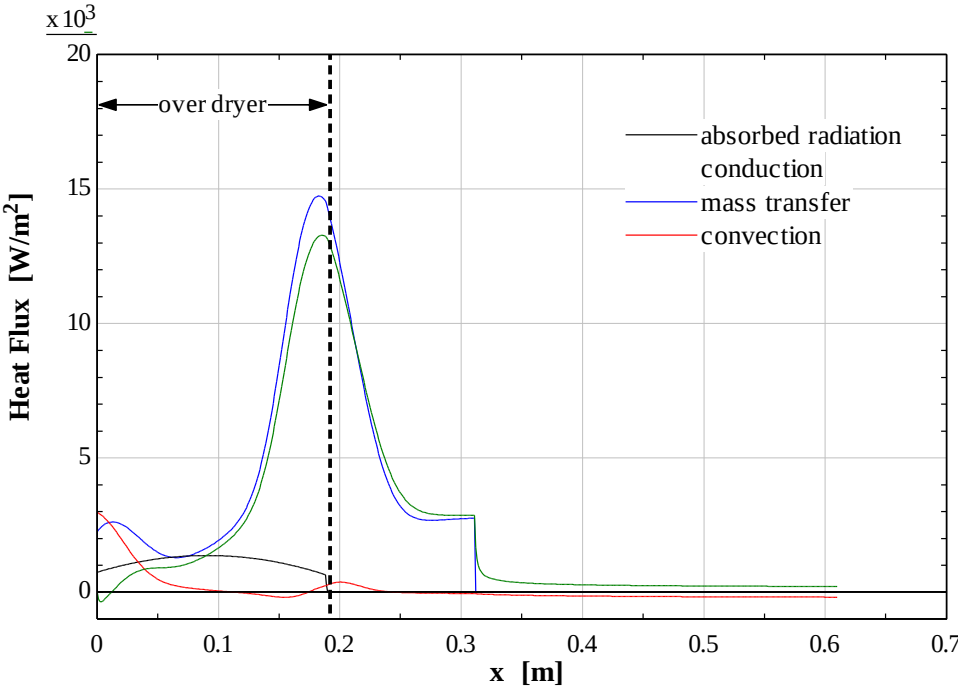

Figure 75: Comparison of heat transfer modes at the printed surface.

Similar to the results from initial drying model in Ch. 2, the mass transfer was mainly driven by radiant energy that was absorbed within the front liner and conducted towards the printed surface. Because this conducted energy originated as absorbed radiation, Figure 75 can be adjusted to show the "effective radiation", which is the sum of node 1's absorbed radiation and energy conducted from node 2 to node 1. The graphical comparison of the effective modes of heat transfer is shown in Figure 76.

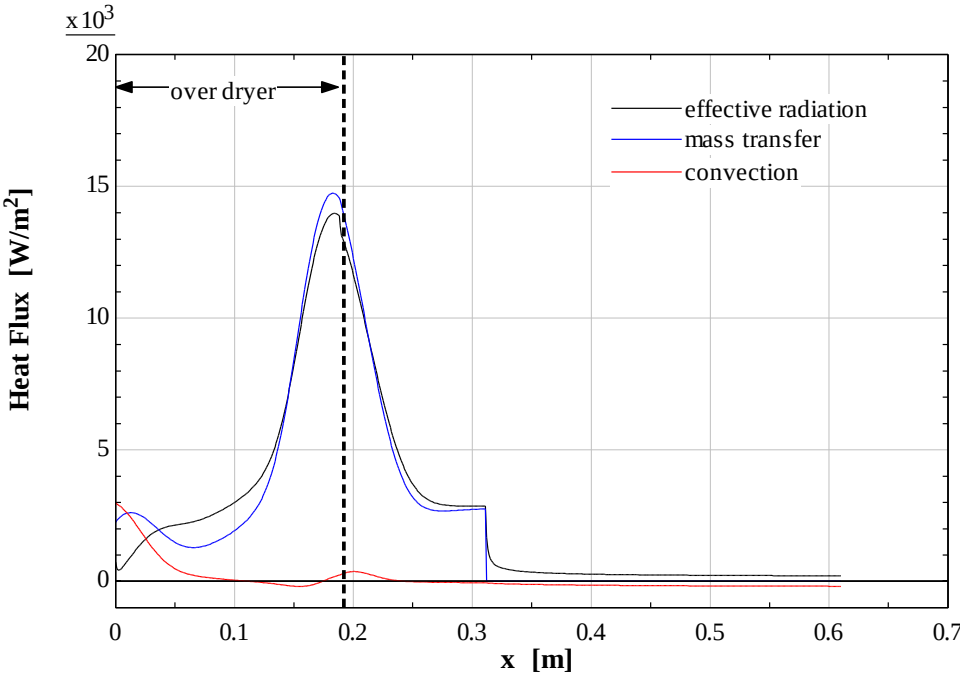

Figure 76: Comparison of effective heat transfer modes at the printed surface.

Finally, the overall modes of heat transfer of the drying process were compared by plotting the front liner's total absorbed radiation, the mass transfer, and the convection term. A comparison of the total heat transfer modes for the entire front liner is shown in Figure 77.

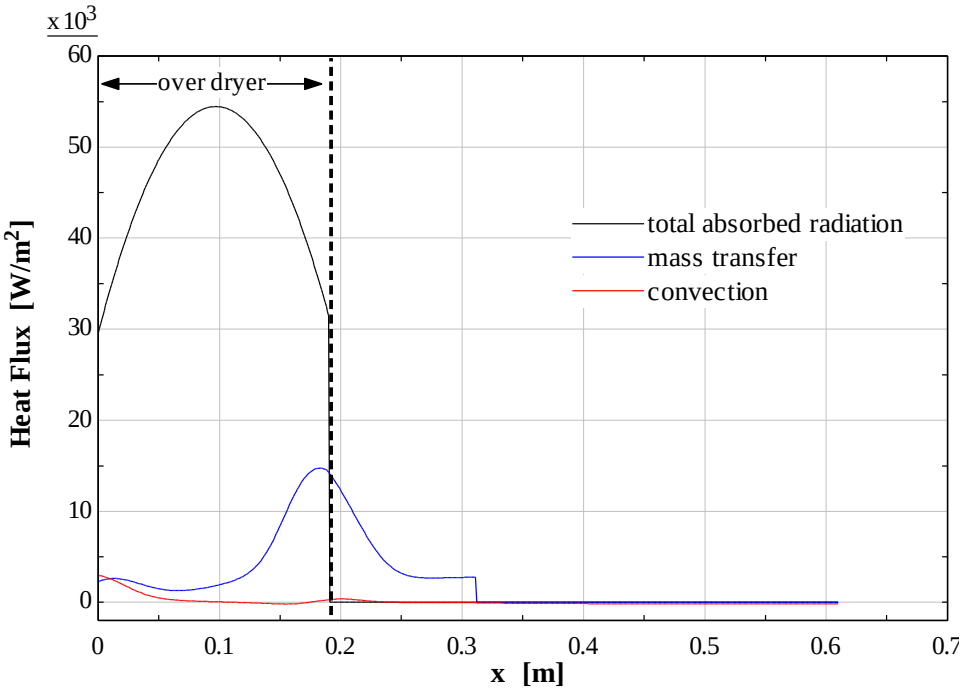

Figure 77: Comparison of total heat transfer modes.

The absorbed radiation was clearly the dominant force for the drying process. As was done in Eq. (27), a drying efficiency was determined by comparing the area under the mass transfer curve to the area under the absorbed radiation curve.

$$\eta_{rad\to evap} = \frac{energy\ required\ to\ evaporate\ moisture}{radiant\ energy\ absorbed\ in\ \ front\ liner} = \frac{3{,}033\ \frac{J}{m^2}}{16{,}892\ \frac{J}{m^2}} \approx 18.0\% \tag{139}$$

This efficiency describes how much of the front liner's absorbed radiation was utilized to evaporate the ink's moisture. This 18.0% is higher than the 11.5% calculated in Eq. (27), because the total radiation absorbed in the front liner decreased due to the improved analysis from the dryer radiation model.

The efficiency in Eq. (139) only accounted for the energy conversion from absorbed radiation within the front liner to moisture evaporation. The total energy efficiency also accounts for the energy conversion from supplied electrical energy to absorbed radiation. This electrical to radiation efficiency was determined via in the dryer radiation model according to Eq. (134), and shown explicitly for the SW-C-9.4 setup in Eq. (140).

$$\eta_{elec\to rad} = \frac{\dot{q}_{board,tot}}{\dot{q}_{supp,elec}} = 52.6\% \tag{140}$$

The total efficiency of the system was calculated by combining the efficiencies in Eqs. (139) and (140).

$$\eta_{tot} = \eta_{elec\to rad}\eta_{rad\to evap} = \left(0.526\right)\left(0.180\right) = 10.1\% \tag{141}$$

7.2 Exponential Radiation Absorption

In section 7.1 and Ch. 2, the radiation that was absorbed in the front liner was assumed to be equally-distributed throughout the thickness of the front liner, as shown in Eq. (142).

$$absorbed\ radiation_i = \begin{cases} \dot{q}''_{rad}\left(\dfrac{\Delta y}{th_{eff}}\right), & for\ 2 \le i \le N-1 \\ \dot{q}''_{rad}\left(\dfrac{\Delta y/2}{th_{eff}}\right), & for\ i = 1, N \end{cases} \quad (142)$$

where $absorbed\ radiation_i$ is the radiation heat flux that gets absorbed in node i, $\dot{q}''_{rad}$ is the total amount of radiation that is absorbed in the front liner, Δy is the distance between nodes, and th_{eff} is the effective thickness of the front liner. The reason nodes 1 and N absorbed less radiation is because their control volumes were half as tall as the internal control volumes. While this was an appropriate first assumption, the results of the initial model (discussed in section 2.4) showed that this equally-distributed assumption could majorly impact the model results since the majority of the energy used for evaporating the moisture came from radiant energy that was absorbed within the internal nodes of the front liner.

The front liner likely to absorbs the radiation according to an exponential distribution. Instead of all nodes receiving an equal amount of absorbed radiation, the node at the printed surface (node 1) absorbs more radiation than the node at the back of the front liner (node N). The distribution of absorbed radiation within the front liner is provided by Eq. (143).

$$\dot{q}''_{rad,abs} = \dot{q}''_{rad}\alpha e^{-\alpha y}, \quad for\ 0 \le y \le th_{eff} \quad (143)$$

where $\dot{q}''_{rad,abs}$ is the depth-specific heat flux within the front liner, and α is the absorption coefficient of the radiation heat flux. The absorption coefficient has units of 1/m, thus $\dot{q}''_{rad,abs}$ has units of kW/m^3. The absorption coefficient is a metric of how deep the radiation must penetrate into a surface before all the radiation is absorbed. Because the absorption coefficient models an exponentially decaying value, the reciprocal of an absorption coefficient is analogous to a time constant for a 1st-order system, τ (as discussed in section 5.6). Just as 3τ corresponded

to 95% of the overall change of a first-order system step response, a distance of $\frac{3}{\alpha}$ into the front liner corresponds to 95% of the radiation being absorbed. Thus, large absorption coefficients correspond to short the penetration depths. Figure 78 illustrates an example absorption distribution in relation to the physical thickness of the front liner.

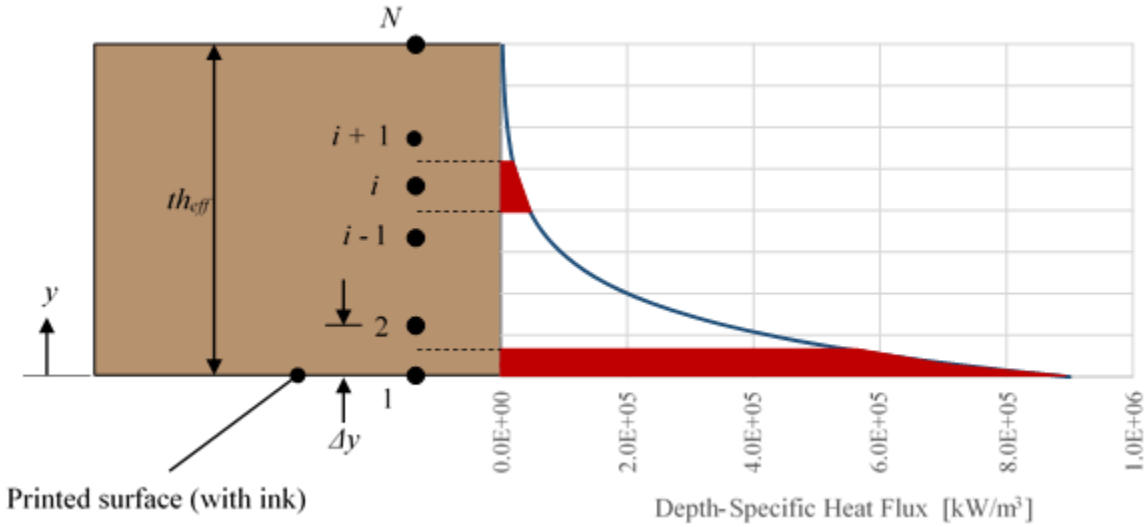

Figure 78: Exponentially-distributed radiation absorption within the front liner.

The long, narrow red box at the bottom of Figure 78 represents the amount of radiation that is absorbed in node 1. The small red box next to node *i* is the amount of radiation absorbed in node *i*. Note that node 1's red area is half the height of node *i*'s red area because node 1's CV is half as tall. The amount of radiation heat flux that is absorbed at each node can be determined by integrating the absorption distribution, as performed in Eq. (144).

$$\dot{q}''_{abs,i} = \int_{y_{bott,i}}^{y_{top,i}} \dot{q}''_{rad} \alpha e^{-\alpha y} dy = \dot{q}''_{rad} \left(e^{-\alpha y_{bott,i}} - e^{-\alpha y_{top,i}} \right), \quad for\ i = 1..N \tag{144}$$

where $y_{top,i}$ and $y_{bott,i}$ are the upper and lower boundaries of node *i*'s CV. Summing all of the nodes' absorbed heat fluxes should result in the board's total absorbed heat flux, $\dot{q}''_{rad}$.

Using an absorption coefficient to model the radiation absorption within the front liner was more realistic than assuming the equally-distributed model because as radiation penetrates into a surface and gets absorbed at a given *y*-depth, the following, deeper *y* locations are exposed to less radiation. Unfortunately the radiation absorption coefficient of corrugated board was not known, thus multiple absorption coefficients were used in the model to see how the absorption coefficient impacts the drying process. Care was taken when implementing the absorption distribution in the dryer model to ensure that the absorption coefficient was large enough that nearly all the radiation was absorbed within the front liner. For example, Figure 79 displays the absorption distribution for three different absorption coefficients.

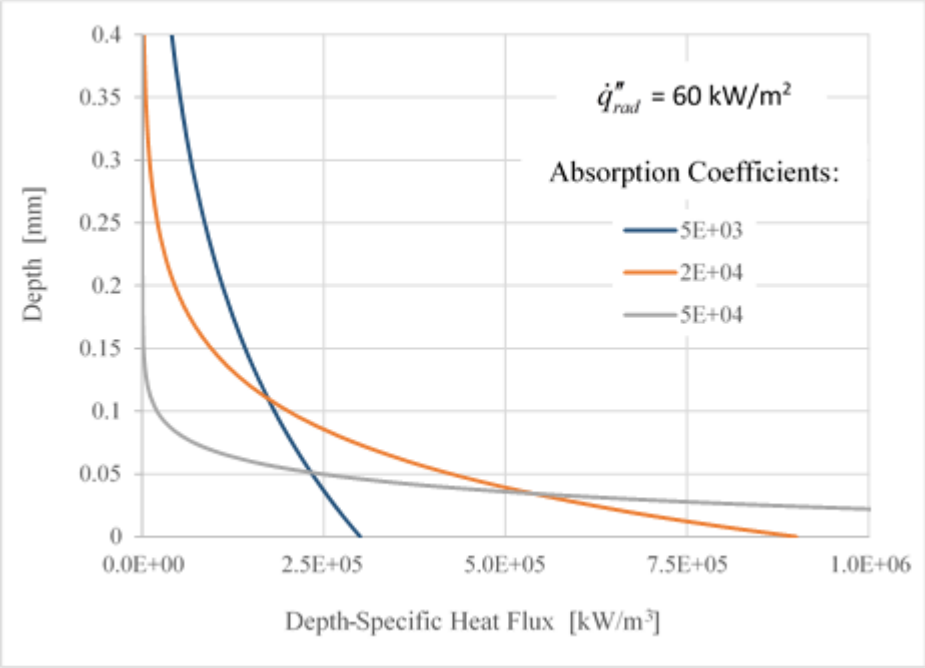

Figure 79: Comparison of three different absorption distributions.

Notice that the smallest absorption coefficient (α = 5e3 1/m) never reached a 0 depth-specific heat flux. This means that front liner was actually allowing some of the radiation energy to transmit through the front liner and not get absorbed. The drying model assumed that $\dot{q}''_{rad}$ was absorbed entirely in the front liner ($\dot{q}''_{rad}$ was determined by the dryer radiation model,

which assumed $\dot{q}''_{rad}$ was absorbed by the board surface). The other absorption coefficients from Figure 79 (α = 2e4 and 5e4 1/m) absorbed all the radiation, but had drastically different distributions. The α = 2e4 1/m distribution penetrated just deep enough to absorb all the radiation within the front liner, while the α = 5e4 1/m distribution absorbed all the radiation within nearly 0.1 mm of the printed surface. Figure 80 displays the percent of absorbed radiation as a function of the absorption coefficient. Notice that the curve eventually reached 100% for any absorption coefficient larger than approximately 1.6e4 1/m.

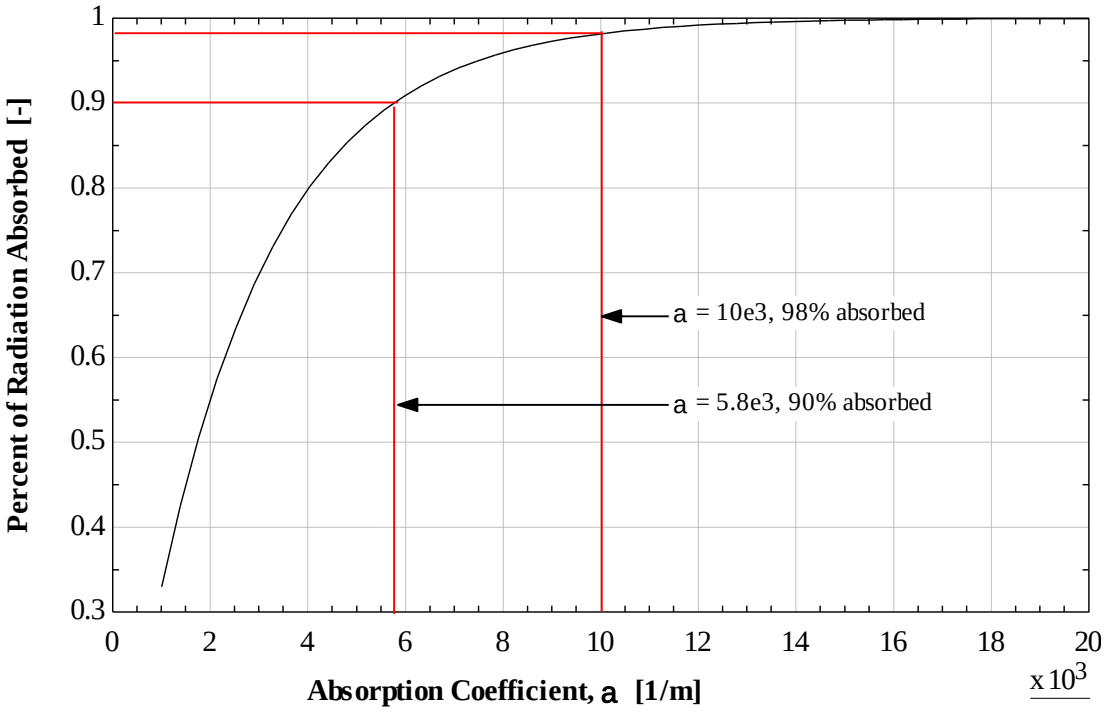

Figure 80: Percent of radiation absorbed vs. the absorption coefficient.

While all the radiation should be absorbed in the front liner, assigning too large an absorption coefficient causes all the radiation to be concentrated near the printed surface of the board. In the model, too much radiation absorbed near the surface caused the printed surface temperature to increase above the boiling point of water (this circumstance also depended on parameters such as board speed and power level). This would cause the moisture to boil instead of being driven off by mass transfer, which could not be tracked in the model. To keep the

surface temperature reaching its boiling temperature, the absorption coefficient was allowed a lower bound of 5.8e3 1/m, which corresponds to 90% radiation absorbed as shown in Figure 80. While this meant that the front liner did not absorb all the radiation it was assumed to, the model still provided realistic results.

7.3 Drying Model Results with Exponential Radiation Absorption

The exponential absorption distribution was implemented in the drying model (using the same parameters as described in section 7.1). The model's temperature and moisture distributions for an absorption coefficient of α = 5.8e3 1/m are shown in Figure 81.

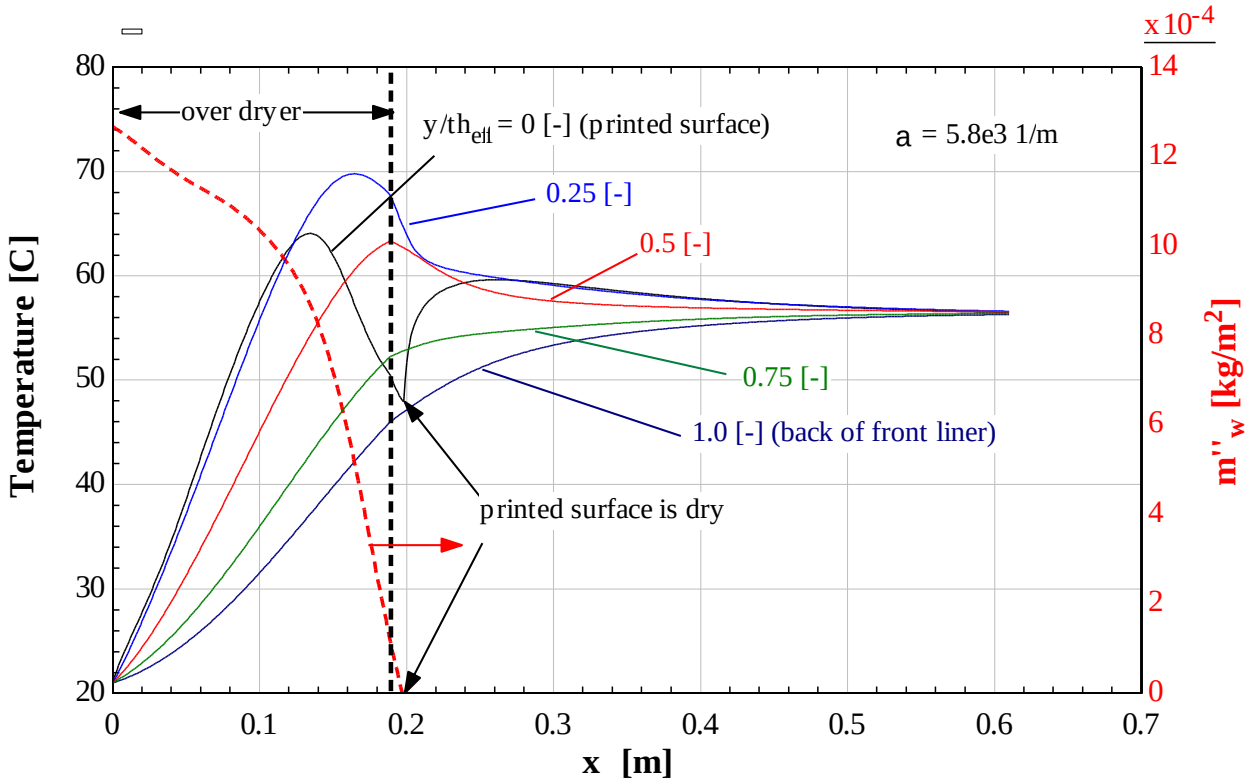

Figure 81: Temperature and moisture distribution with α = 5.8e3 1/m.

Notice that the board temperature near the printed surface was the hottest portion of the front liner, whereas previously, the back of the front liner was the hottest portion. This change was a result of the absorption distribution. When the radiation was equally-distributed, the back of the front liner was the hottest because it received the same amount of radiation as the printed

surface, but did not experience the cooling effect of convection or mass transfer. With the radiation exponentially-distributed, the absorbed radiation was more concentrated at the printed surface, and the back of the front liner experienced far less radiation than the printed surface.

As soon as the printed surface became dry ($x \approx 0.19$ m), the surface temperature instantaneously increased because of the loss of the mass transfer's cooling effect. This spike in temperature occurred after exiting the drying area, so the spike was not forced by radiation but rather by conduction from the nearby hot nodes of the front liner. The contribution of the modes of heat transfer at the printed surface is shown in Figure 82.

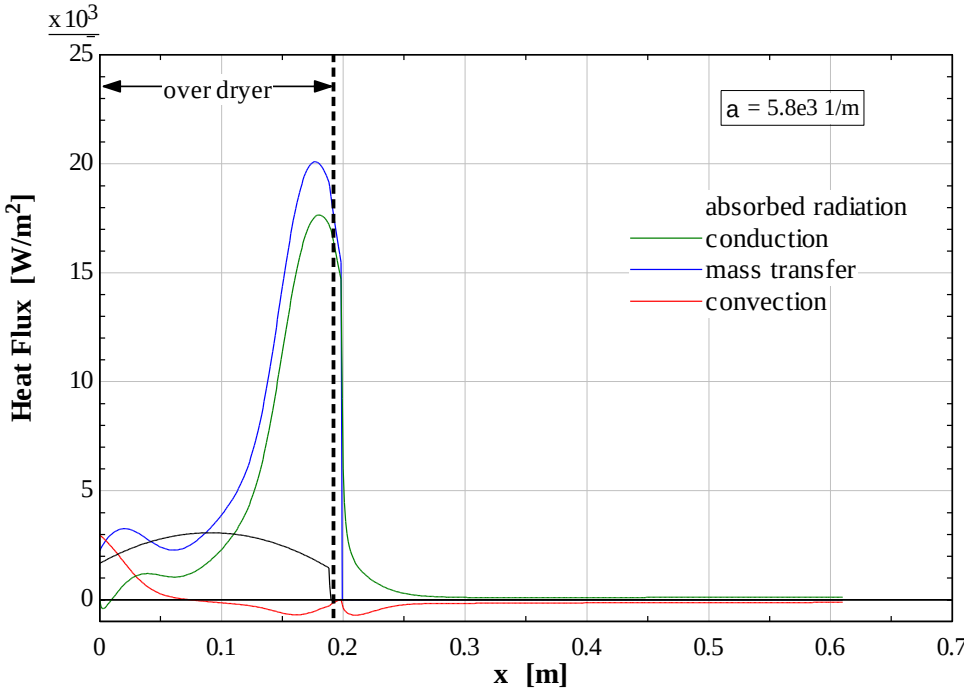

Figure 82: Comparison of heat transfer modes at the printed surface with α = 5.8e3 1/m.

The combination of absorbed radiation and conduction (which was energy that originated as radiation) dominated the mass transfer process. Compared to Figure 75, Figure 82 shows that much more radiation was absorbed at the printed surface node. The overall comparison of heat transfer modes is shown in Figure 83.

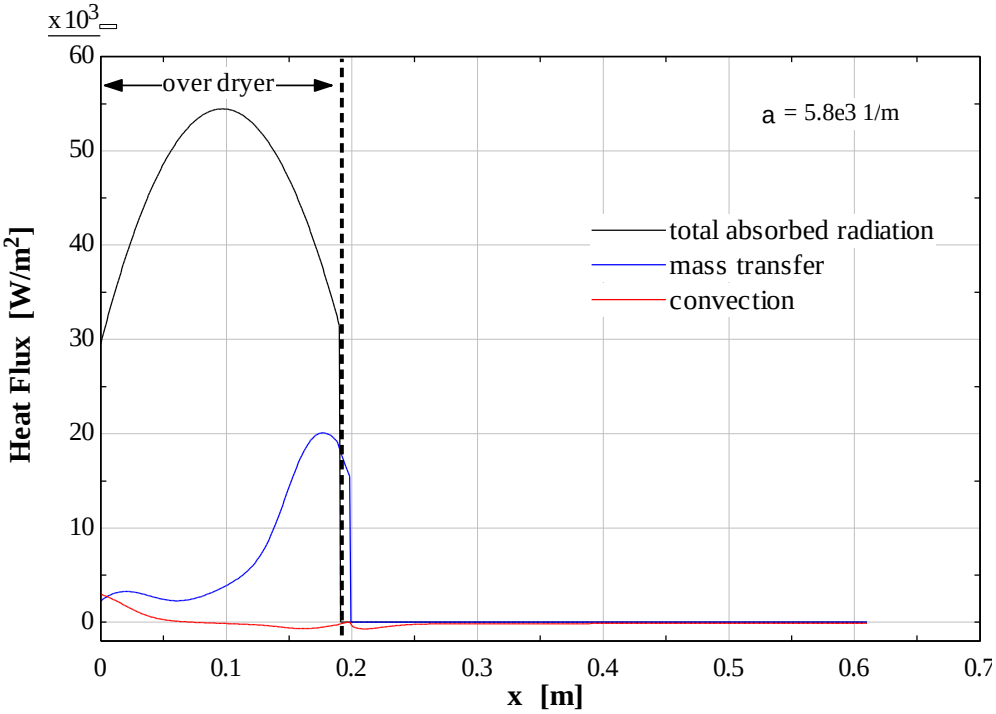

Figure 83: Comparison of total heat transfer modes with α = 5.8e3 1/m.

The radiation was overwhelmingly the largest forcing component of the process. The area under the blue curve illustrates the total amount of energy required to evaporate the ink's moisture, while the area under the black curve represents the total radiant energy absorbed by the front liner. The efficiency was determined by comparing their areas, as in Eq. (145).

$$\eta_{rad\to evap} = \frac{3{,}036\ \frac{J}{m^2}}{16{,}900\ \frac{J}{m^2}} \approx 18.0\% \tag{145}$$

The efficiency found in Eq. (145) was the same value as found in Eq. (139), where the front liner had an equal absorption distribution. This is not surprising because the same amount of radiant energy was absorbed in the front liner and the same amount of energy was required to evaporate moisture—the only parameter that differed between the two simulations was the distribution of how the radiation was absorbed within the front liner. Even though the absorption distribution did not affect efficiency, it still affected the performance of the dryer. The board

simulated with equally-distributed radiation absorption dried approximately at $x \approx 0.31$ m, whereas the board with the exponentially-distributed absorption distribution dried at $x \approx 0.19$ m. The exponentially-distributed absorption caused the printed surface to reach a higher temperature more quickly because it concentrated the radiation near the surface. The higher surface temperature created a more conducive environment for mass transfer, and thus the ink evaporated more quickly.

The other absorption coefficient simulated was α = 10e3 1/m, which was also shown in Figure 79. With α = 10e3 1/m, the front liner absorbed 98% of the radiation—close to the assumption that the front liner absorbed all the radiation determined by the dryer radiation model. The temperature and moisture distribution with α = 10e3 1/m is shown in Figure 84.

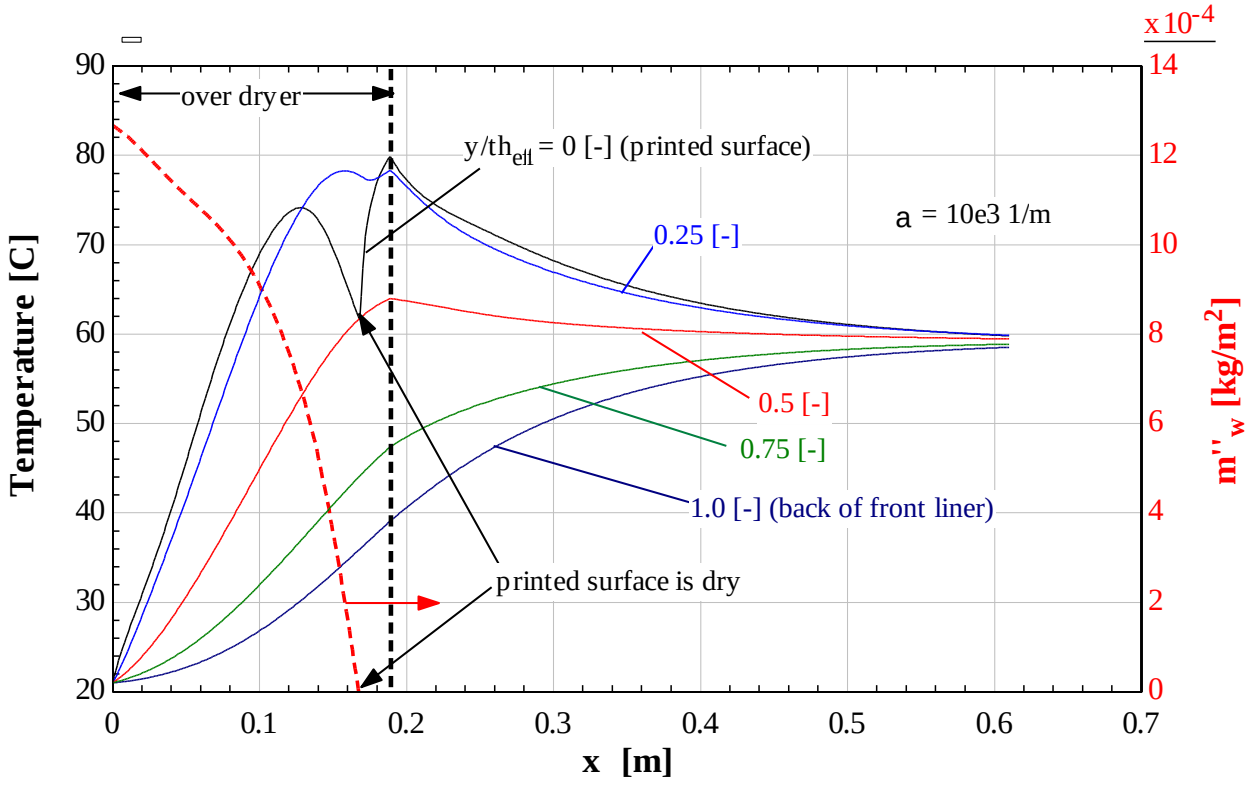

Figure 84: Temperature and moisture distribution with α = 10e3 1/m.

The front liner's overall temperature behavior was similar to that shown in Figure 81, but it reached a hotter temperature. This is due to the fact that the increased absorption coefficient

concentrated more of the absorbed radiation near the printed surface. Additionally, the printed surface did dry slightly sooner with the increased absorption coefficient ($x \approx 0.17$ m, compared to $x \approx 0.19$ m).

7.4 Updated Drying Model Overview

The initial drying model from Ch. 2 was improved by specifying the spatially-varying heat flux that the board received while over the dryer and a spatially-varying convection coefficient. The radiation heat fluxes calculated for the eight board surfaces in the dryer radiation model were fit to a 2nd-order polynomial, so that the heat flux absorbed by the board was determined by the board's location relative to the dryer. The 2nd-order polynomial curve was applied only to the x-locations directly over the dryer. Furthermore, the board's convection coefficient was updated to a spatially-varying distribution to reflect the board's high convection coefficients while directly over the forced air jet holes at the ends of the dryer cassettes, and low convection coefficients elsewhere. The changes to a spatially-varying radiation heat flux and convection coefficient provided a more realistic estimation of the actual drying process because the spatially-varying values were proven experimentally.

The initial drying model was updated further by applying an exponential radiation absorption distribution within the front liner. The results of the initial drying model (which assumed an equally-distributed radiation absorption) showed that radiation absorbed near the printed surface had a large impact on the drying process. A more realistic distribution for the radiation absorption was an exponentially-decaying distribution, where the majority of the absorbed radiation was concentrated near the printed surface. While the exponential absorption distribution was likely realistic of the actual process, there no experimental work was performed to determine empirically the front liner's absorption coefficient. Two approximate absorption

coefficients were implemented in the drying model to see the absorption coefficient's effect on the drying process—large absorption coefficients dried the printed surface quicker than small absorption coefficients. The EES file for the updated drying model can be found in the online supplement, as directed by Appendix C:.

Ch. 8 Conclusion and Future Work

The research presented above was conducted to gain a better understanding of the drying process utilized in industrial offset printing applications. The analysis began by splitting the drying process into its four different modes: radiation, convection, conduction, and mass transfer. With numerous assumptions, an initial drying model (discussed in Ch. 2) was created to simulate the drying process and understand the important parameters in the process. The initial model showed that radiation was the dominant force in the drying process.

Since radiation was the dominant force within the drying process, a radiation model was designed to analyze the effects of various parameters on the radiation heat flux incident on the printed substrate. Before constructing the radiation model, the semi-transparent radiosity method (STRM) was developed (derived in Ch. 3). The STRM is a technique for modeling radiation exchange within enclosures that have semi-transparent surfaces. The STRM is a system of equations that can track the emission, reflection, and absorption of thermal radiation between surfaces. The STRM improves upon the coupled sub-enclosure method (CSEM) because it uses effective view factors to maintain transmitted radiation's directionality through a semi-transparent surface. The STRM was compared to the Monte Carlo method (MCM), considered to be the gold standard for thermal radiation modeling. The MCM is a stochastic technique that randomly emits rays of radiation from the modeled surfaces and tracks each ray as it propagates through space and reflects off or transmits through surfaces, until the ray is absorbed by another surface. The STRM and MCM provided the same results when operating under the same assumptions. The STRM's advantage over the MCM was its computational efficiency; the STRM is a linear system of equations, whereas the MCM is a compiled, stochastic method which

requires a large number of rays to be simulated—which requires an exceedingly large number of calculations.

The dryer radiation model described in Ch. 4 used the STRM to track the radiation exchange of three dryer cassettes and a corrugated board surface, as well as the convection at each surface. The dryer radiation model determined the amount and spectrum of radiation that the corrugated board absorbed, along with a 1-D spatial distribution of the radiation. Changes in lamp type, power level, glass type, clearance height, etc. were all accounted for in the dryer radiation model.

To ensure that the dryer radiation model was accurate, an experiment was performed to measure the spatial distribution of the heat flux from the dryers. The experiment (explained in Ch. 5) utilized automated CNC and DAQ equipment to record process parameters at various locations relative to three dryer cassettes. After logging all the measurements, the values at each location were averaged to eventually produce a 1-D spatial distribution of the heat flux and surface temperature. The recorded surface temperatures and other process parameters (lamp type, glass type, power level, etc.) were then input into the dryer radiation model in Ch. 4. The 1-D heat flux distribution calculated by the radiation model was compared to the experimentally measured heat flux distribution to ensure the dryer radiation model was producing realistic results. The comparison of heat flux distributions showed that the model closely matched the experimental heat fluxes, as shown in Ch. 6.

The initial drying model was updated to include the spatially-varying radiation heat flux and convection coefficient distributions. The radiation heat flux implemented in the updated drying model was a 2^{nd}-order polynomial fit to the results of the dryer radiation model. The convection coefficient distribution was made to be a maximum at the ends of the dryer cassette

(where the forced air jet holes are located), and then decrease in value as the position deviates from the cassette ends, with a shape similar to a normal distribution. Additionally, the initial drying model was improved by adding an exponentially-decaying radiation absorption distribution in the front liner. The initial drying model assumed that the radiation was absorbed evenly throughout the thickness of the front liner. The exponential absorption distribution was more realistic because more radiation was absorbed near the surface. The change in absorption distribution did not affect the efficiency of the drying process, but it did cause the printed surface to be dried more quickly.

The focus of this research was to better understand and model the radiation exchange in the drying process, because radiation was the dominant force in the drying process. The other modes of heat transfer still affect the drying process and should be investigated in more detail. One possibility for further development is determining the radiant properties of the corrugated board. The work done in Ch. 6 and Ch. 7 assume that the corrugated board has the same emissivity as the heat flux sensor, thus the corrugated board and the heat flux sensor absorb the same amount of radiation. In reality, the corrugated board most likely has a smaller emissivity than the heat flux sensor, which will absorb less radiation. The front liner is the only thermally-important feature of the corrugated board, and the front liner is only 0.3 mm thick. With the front liner being so thin, it could be possible that the front liner is even transmissive to some wavelengths of radiation. With an accurate estimate of the corrugated board's radiant properties, the dryer radiation model can be utilized to its full advantage.

Similar to the board's radiant properties, the board's radiation absorption coefficient should be determined. Determining the absorption coefficient of the front liner will solidify how the absorbed radiation is distributed within the front liner. Ch. 7 showed that how the radiation

was distributed within the front liner significantly impacted the dryer's performance. Furthermore, experimental confirmation should be considered for determining the front liner's thermal conductivity, specific heat, and density. The majority of the energy that is used to evaporate the moisture is delivered to the surface via conduction through the front liner. The thermal conductivity, specific heat, and density of the front liner all affect the storage and conduction within front liner, thus they could impact the model's results.

Another possibility for future work includes a more in-depth analysis of the surface convection coefficient. Although convection was shown to not significantly affect the drying process, the convection coefficient still played a substantial role in the mass transfer portion of the drying process; under the heat-mass transfer analogy, the mass transfer coefficient was proportional to the convection coefficient. While the convection coefficient used in the radiation and drying model agreed with the experimental measurements, the convection coefficient should be investigated separately in deeper detail.

The final path for future work involves determining the moisture absorption properties of the corrugated board. The drying model assumed that all the moisture was present only at the printed surface. In reality, uncoated corrugated board is able to wick moisture away from the printed surface and into the interior of the board. Since the board may have an affinity to the moisture, the drying process could require more drying power, as the moisture needs to be forced through the substrate and then evaporate it off the surface. Fortunately, only the material near the printed surface needs to be dry enough for the ink to not smear. Even if moisture is present within the front liner but sufficiently below the printed surface, the inked image would be considered dry to the touch. The dynamics of the moisture concentration within the front liner could significantly effect on the model results.

References

[1] R. Siegel and J. Howell, Thermal Radiation Heat Transfer, 2nd ed., New York: Hemisphere Publishing Corporation, 1981.

[2] G. Nellis and S. Klein, Heat Transfer, New York: Cambridge University Press, 2009.

[3] R. Siegel, "Net Radiation Method for Enclosure Systems Involving Partially Transparent Walls," Cleveland, 1973.

[4] J. Duffie and W. Beckman, Solar Engineering of Thermal Processes, 4th ed., Hoboken: John Wiley & Sons, Inc, 2013.

[5] R. Gardon, "The Emissivity of Transparent Materials," *Journal of The American Ceramic Society*, vol. 39, no. 8, pp. 278-287, 1956.

[6] Momentive Performance Materials, Inc., "Optical Properties of Fused Quartz," [Online]. [Accessed 20 March 2016].

[7] SCHOTT Corp, "SCHOTT Product Downloads," [Online]. Available: http://www.us.schott.com. [Accessed 20 March 2016].

[8] F. Incropera and D. DeWitt, Fundamentals of Heat and Mass Transfer, 5th ed., Hoboken: Wiley, 2001.

Appendix A: Experimental Equipment Pictures

Figure 85: Sterlco water chiller.

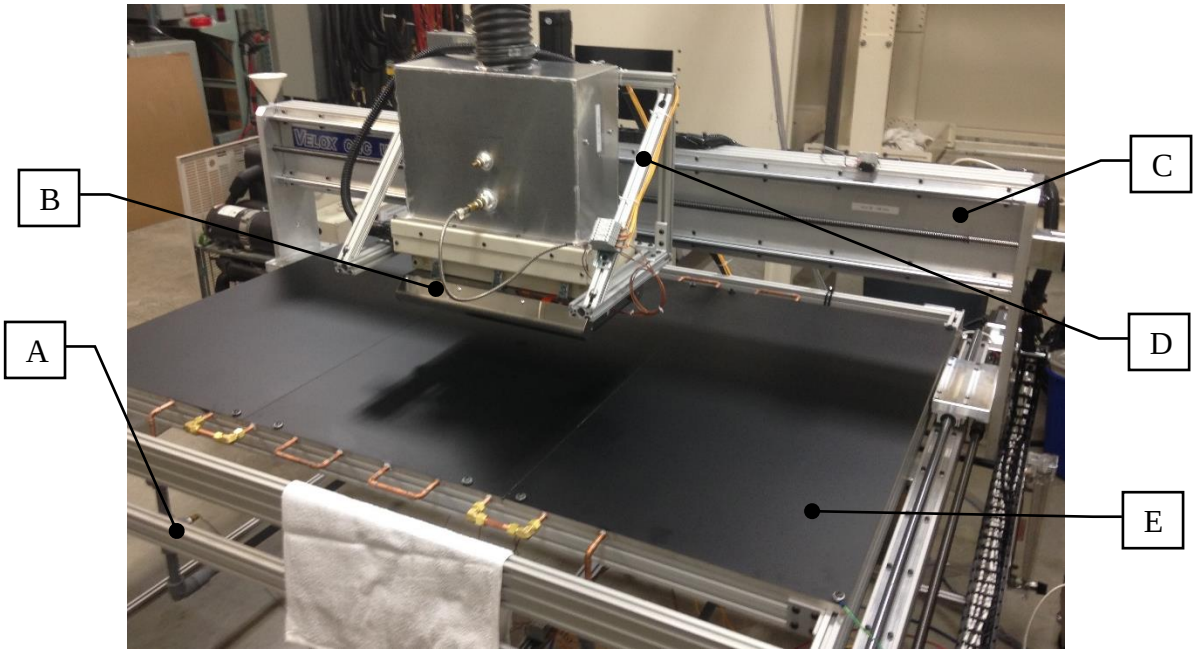

Figure 86: A: support table, B: triple dryer cassette, C: CNC table and motors, D: duct mount, E: chill surface.

Figure 87: Forced air ducting.

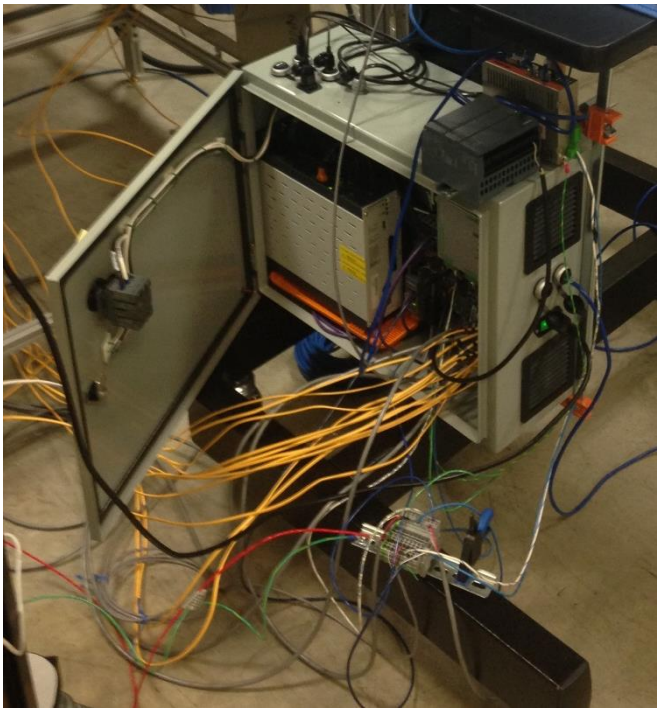

Figure 88: DAQ system.

Figure 89: CNC computer and control box with the Mach3 software.

Appendix B: Experimental Heat Flux Maps

1. SW-C-6.0

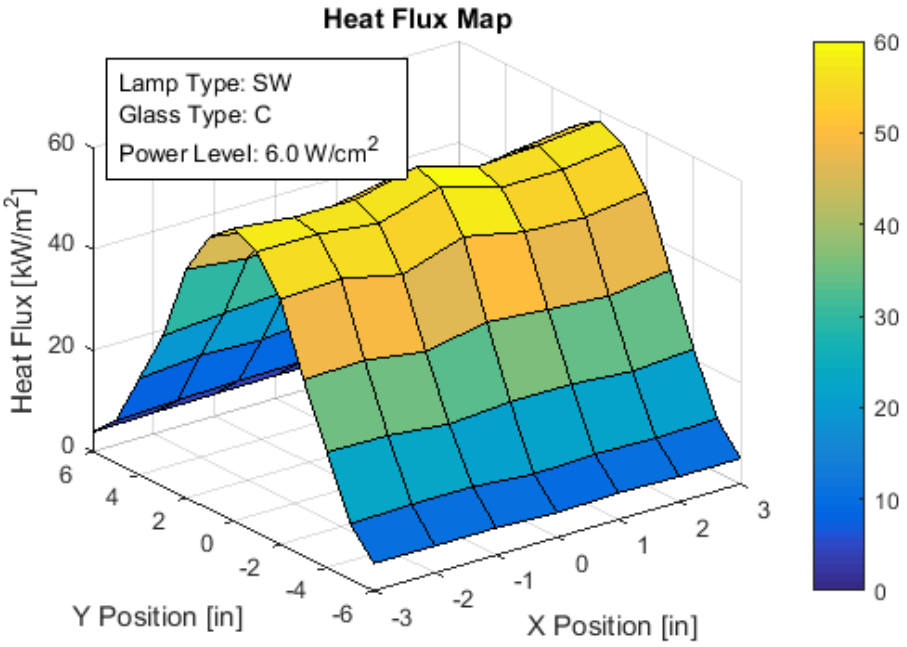

Figure 90: Experimentally measured heat flux map for SW-C-6.0 run.

2. SW-C-9.4

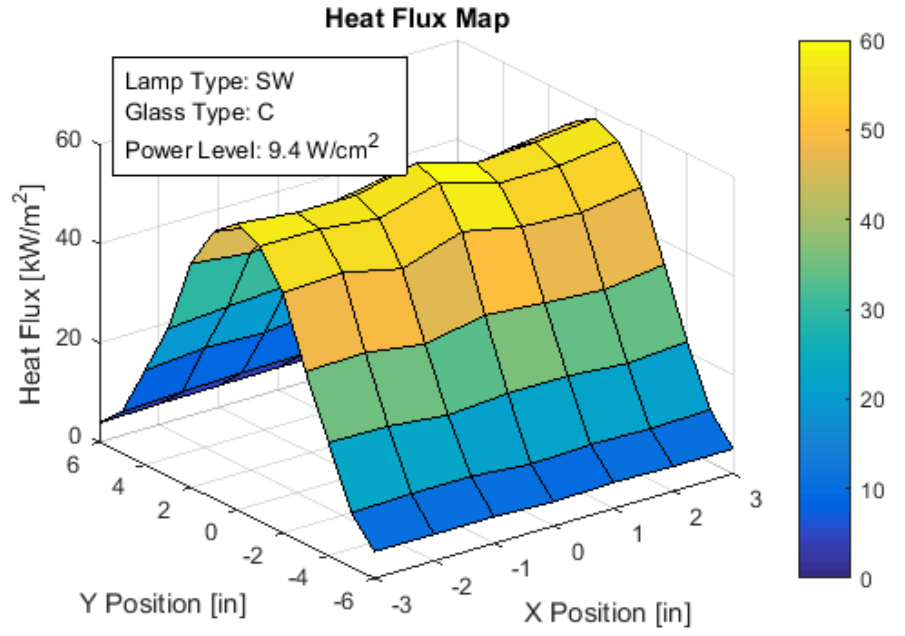

Figure 91: Experimentally measured heat flux map for SW-C-9.4 run.

3. FRMW-C-6.0

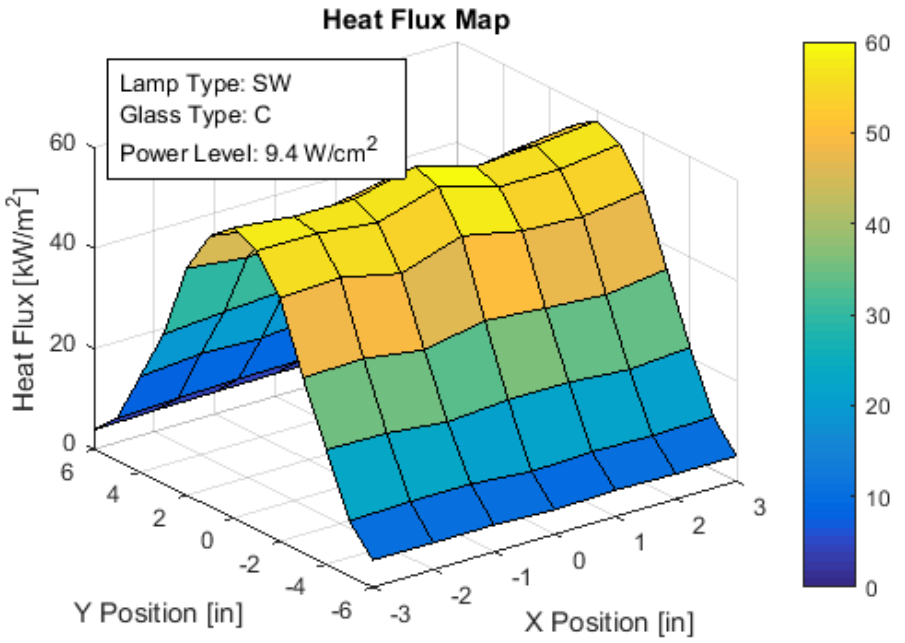

Figure 92: Experimentally measured heat flux map for FRMW-C-6.0 run.

4. FRMW-C-9.4

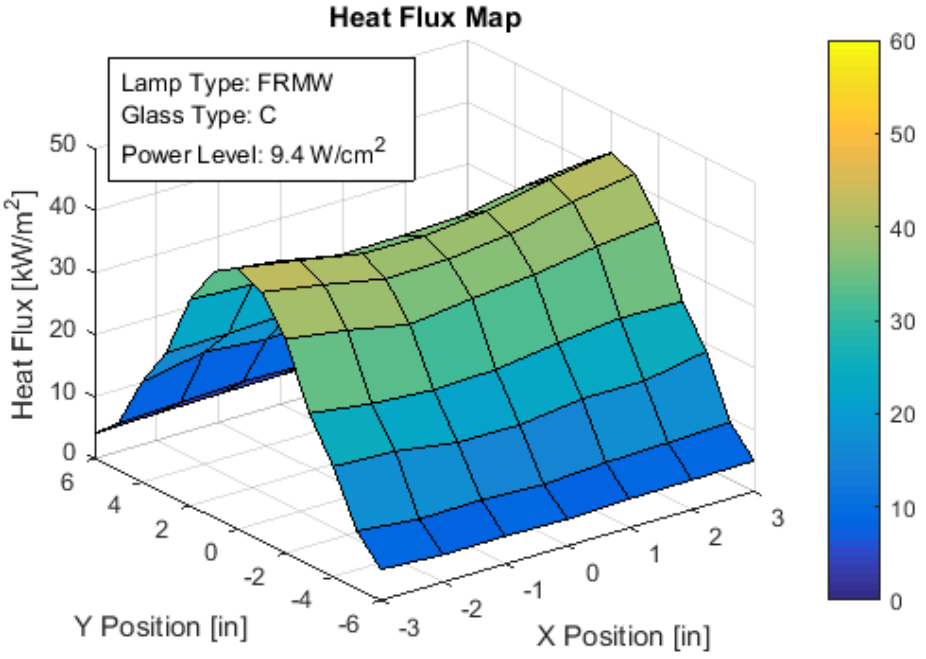

Figure 93: Experimentally measured heat flux map for FRMW-C-9.4 run.

5. MW-C-6.0

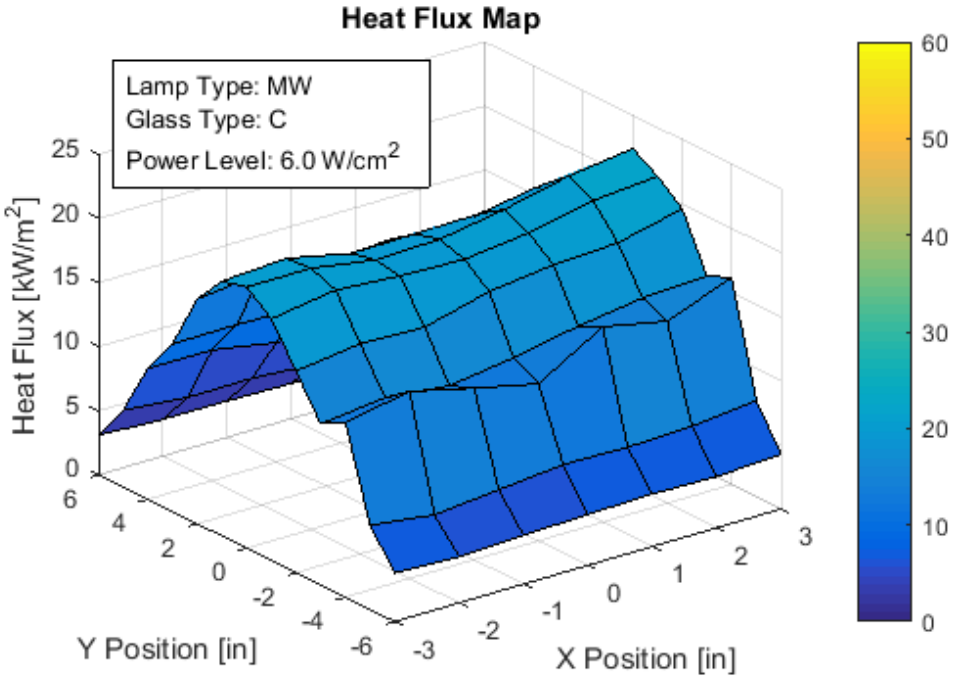

Figure 94: Experimentally measured heat flux map for MW-C-6.0 run.

6. MW-C-9.4

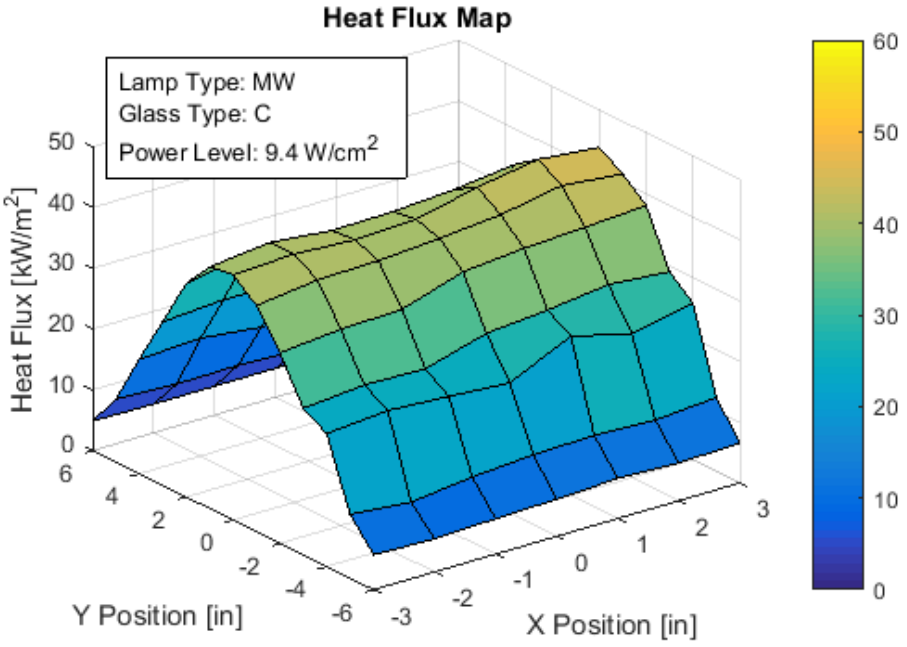

Figure 95: Experimentally measured heat flux map for MW-C-9.4 run.

7. SW-Q-6.0

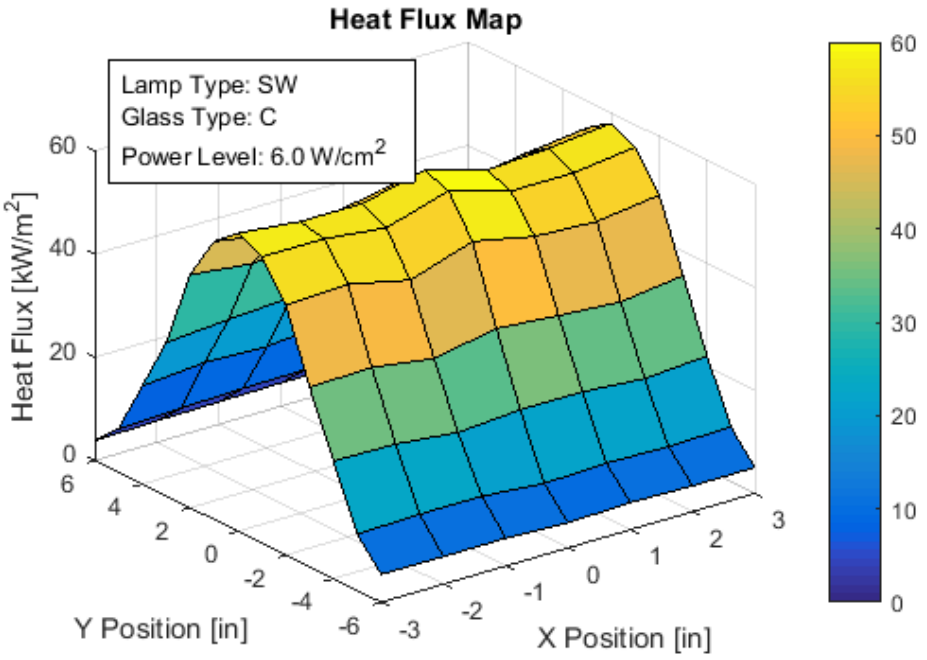

Figure 96: Experimentally measured heat flux map for SW-Q-6.0 run.

8. SW-Q-9.4

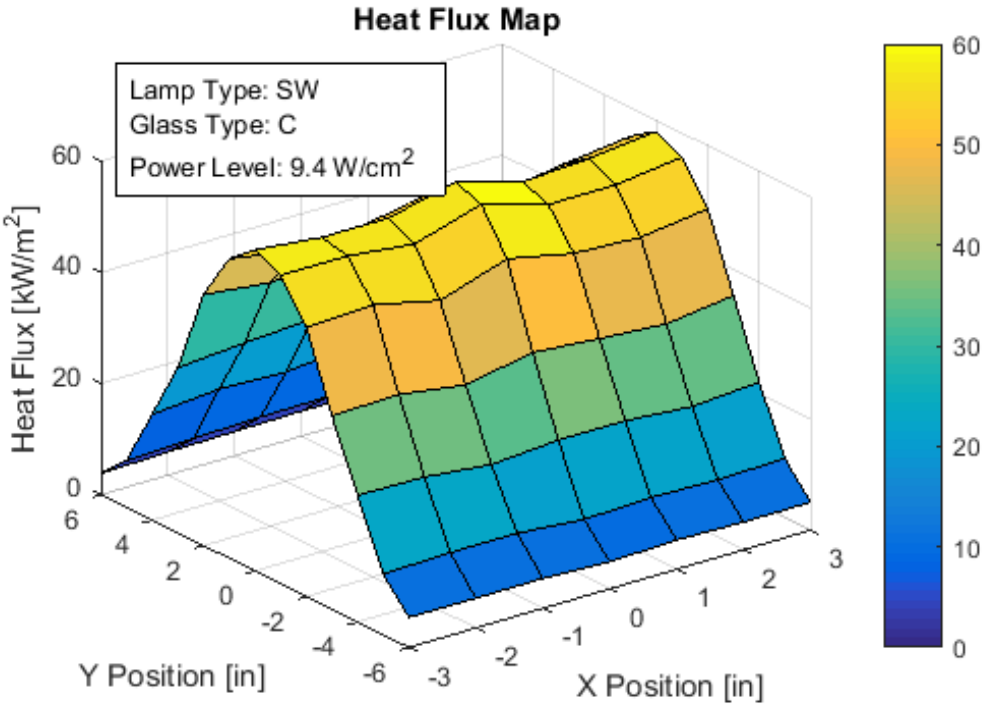

Figure 97: Experimentally measured heat flux map for SW-Q-9.4 run.

9. FRMW-Q-6.0

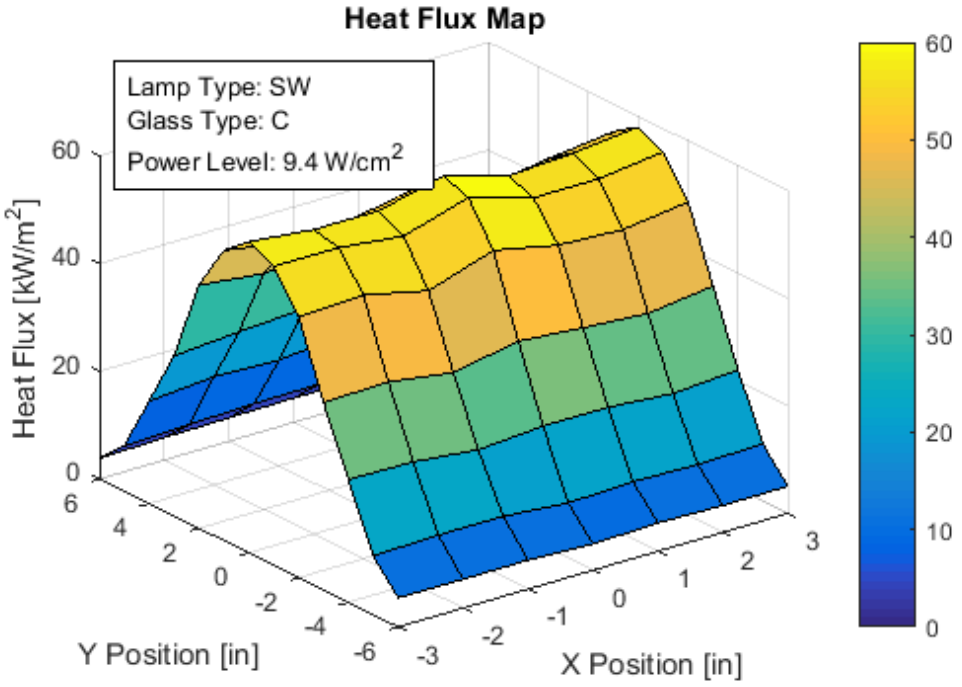

Figure 98: Experimentally measured heat flux map for FRMW-Q-6.0 run.

10. FRMW-Q-9.4

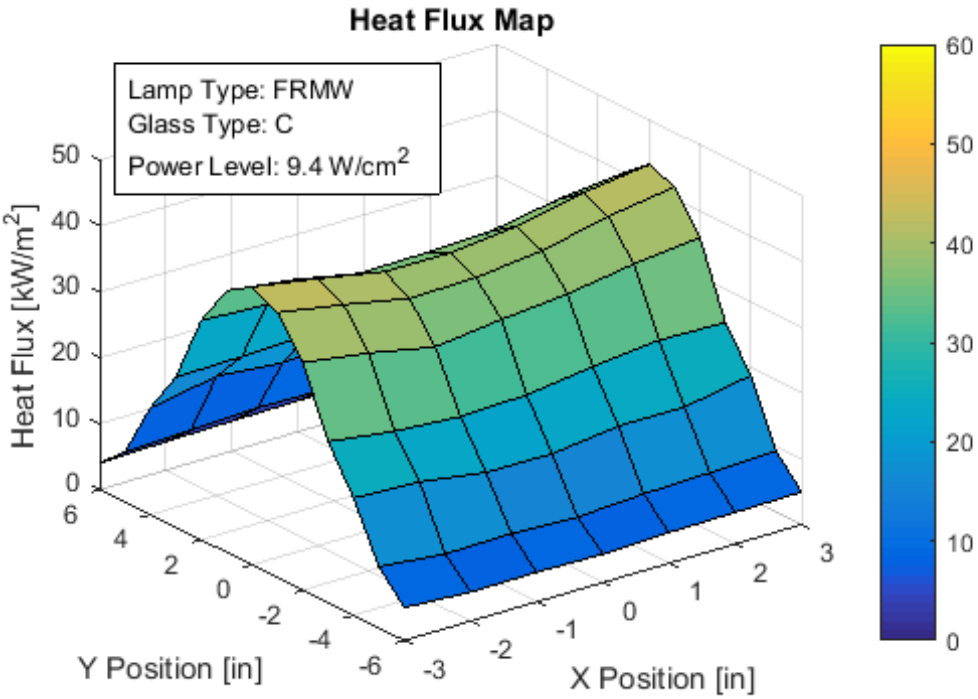

Figure 99: Experimentally measured heat flux map for FRMW-Q-9.4 run.

11. MW-Q-6.0

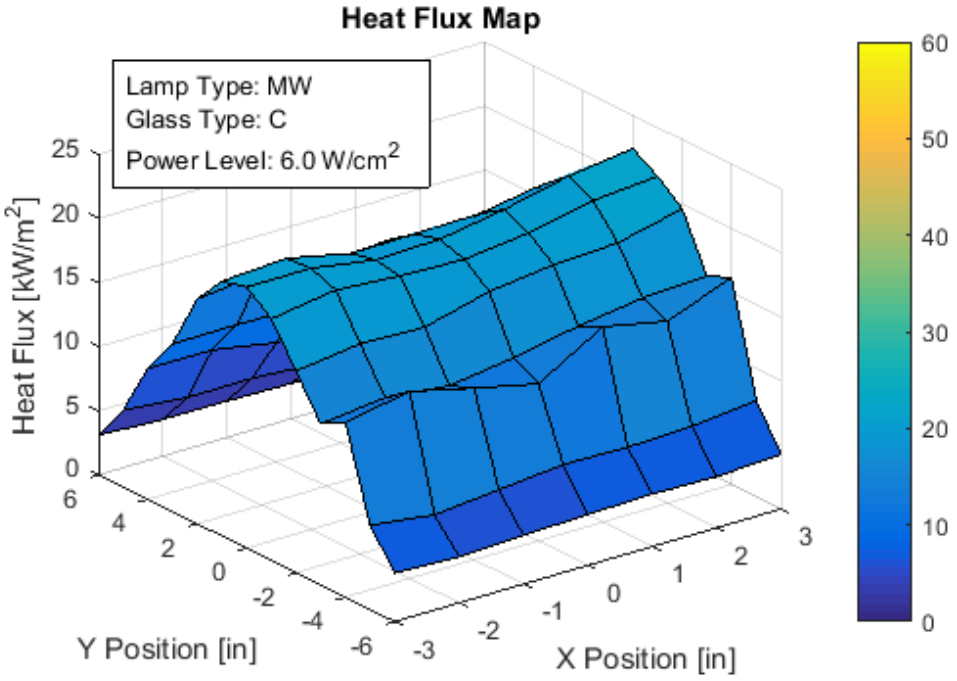

Figure 100: Experimentally measured heat flux map for MW-Q-6.0 run.

12. MW-Q-9.4

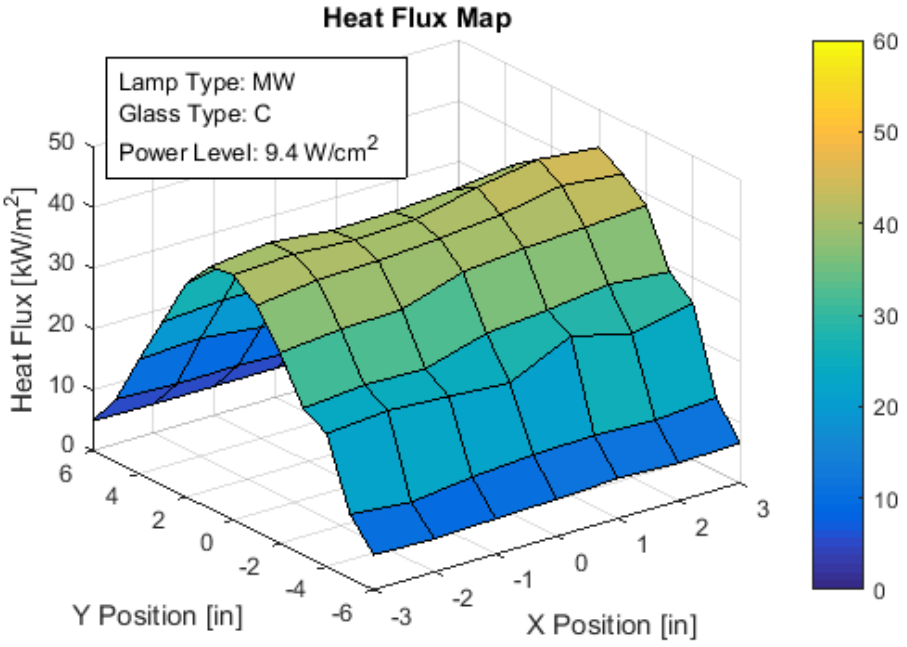

Figure 101: Experimentally measured heat flux map for MW-Q-9.4 run.

Appendix C: Supplemental Online Material

The following files can be found online at: http://sel.me.wisc.edu/publications-theses.shtml

1. Initial Drying Model
2. Monte Carlo Geometric View Factors
3. Lamp Radiation Model
4. Dryer Radiation Model
5. Experimental G-Code
6. Improved Drying Model